



University  
of Glasgow

Liu, Xuefeng (2002) *Quantum well intermixing in 1.55  $\mu\text{m}$  InGaAs/AlInGaAs and InGaAs/InGaAsP structures and applications.*

PhD thesis

<http://theses.gla.ac.uk/4332/>

Copyright and moral rights for this thesis are retained by the author

A copy can be downloaded for personal non-commercial research or study, without prior permission or charge

This thesis cannot be reproduced or quoted extensively from without first obtaining permission in writing from the Author

The content must not be changed in any way or sold commercially in any format or medium without the formal permission of the Author

When referring to this work, full bibliographic details including the author, title, awarding institution and date of the thesis must be given

**QUANTUM WELL INTERMIXING IN 1.55  $\mu\text{m}$   
InGaAs/AlInGaAs AND InGaAs/InGaAsP STRUCTURES  
AND APPLICATIONS**

by

Xuefeng Liu

A Research Carried out at the

Department of Electronics and Electrical Engineering,

University of Glasgow.

Submitted to the University of Glasgow for the Degree of Doctor of Philosophy

© Xuefeng Liu, June 2002

**To my parents**

## ABSTRACT

The work described in this thesis is aimed at the exploring the possibility of optically integrating multi-bandgap energy devices on appropriate semiconductor substrates, using the technology of quantum well intermixing.

A novel quantum well intermixing technique, based on sputtering process induced disordering (SID), has been developed for the first time, addressing multi-bandgap active device integration. Using this technique, blue shifts have been precisely tuned from 0 nm to over 160 nm for the InGaAs/AlInGaAs and from 0 nm to 100 nm for the InGaAs/InGaAsP MQW systems. Assessment of post-process material characteristics has shown that good electrical and optical qualities were maintained in the bandgap widened regions of both the InGaAs/AlInGaAs and InGaAs/InGaAsP material systems. This novel technique has been used to create multi-wavelength light sources that are of potential application in WDM systems and 2x2 crosspoint optical integrated switches. The expected performance has been achieved.

A reactive ion etching process, using  $\text{CH}_4/\text{H}_2$  etching gas, has been investigated, particularly for effective etching in the InGaAs/AlInGaAs MQW system. A 'standard' process for the InGaAs/AlInGaAs material system has been developed, based on experimental research.

A brief theoretical description of waveguides is presented. Three kinds of deep etched waveguides have been fabricated and characterised. It has been found the

surface roughness of narrow, deep etched waveguides has a strong influence on the propagation loss, as in such cases the surface energy scattering by waveguide side wall is significant.

Modelling and design of 3-dB MMI couplers have been carried out. An improved Ti/SiO<sub>2</sub> mask for reactive ion etching has been successfully employed to ensure the waveguide profiles of fabricated MMI couplers meet the design specification, especially regarding the lateral profiles of the MMI section. Characterisation has shown the waveguide profile is close to the design requirement (side wall angle is of  $81\pm 2^\circ$ ).

The principle operation of the so-called terahertz optical asymmetric demultiplexer has been qualitatively described and the design of a Mach-Zehnder interferometer (MZI) type demultiplexer has been carried out. Three kinds of MZI demultiplexers with different geometric structures have been fabricated using SID technique. Assessment of the devices has been carried out, including the operation of semiconductor amplifier, propagation loss of the device, etc.

## ACKNOWLEDGEMENT

During the three unforgettable years that should be a very special experience of my life, many people have contributed to the research leading to this Ph.D. thesis in various ways. I would like to express my most sincere gratitude to all those people, among whom the following are particularly important.

I owe my biggest thankfulness to my supervisor, professor J.H. Marsh. He has supervised my research with a great scholar's foresight, guidance, encouragement and support.

I would like to thank Dr. A.C. Bryce for her great help, encouragement and understanding. Her discussion has been proved so valuable in my research.

Very special gratitude must be given to Dr. Maolong Ke and Dr. Bocang Qiu for their devoting great amount of time and effort to passing on their rich experience, skill and insight in this topic. Without their countless and selfless discussion into smallest details, the research could have never gone so far.

I would like to thank Dr. O.P. Kowalski, Dr. S.D. McDougall, Dr. C.J. Hamilton and Dr. S Najda for their valuable discussion and encouragement.

Special thanks must go to the technical staff of the department, particularly the cleanroom staff, opto-lab staff and dry etching team for their superb technical support.

I must thank the Overseas Research Student (ORS) Awards Scheme and the Faculty of Engineering Scholarship of University of Glasgow for funding my study in Glasgow.

Finally, I owe my special thanks to my wife Min Pei and my son Weiran for their support, understanding, ...and love.

## PUBLICATIONS

1. X.F. Liu, B.C. Qiu, M.L. Ke, A.C. Bryce, J.H. Marsh, 'The Application of a Novel Intermixing Technique for Multi-Bandgap Integration of InGaAs/AlInGaAs', *13<sup>th</sup> IEEE Annual Lasers and Electro Optics Society (LEOS) Meeting Proceedings, THR4, 2000*
2. X.F. Liu, B.C. Qiu, M.L. Ke, A.C. Bryce, J.H. Marsh, 'Control of Multiple Bandgap Shifts in InGaAs/AlInGaAs Multiple Quantum Well Material Using Different Thickness of PECVD SiO<sub>2</sub> Protection Layers', *IEEE Photonics Technology Letters, Vol.12, No.9, pp.1141-1143, 2000*
3. M.L. Ke, B.D. Allan, X.F. Liu, A. Boyd, B.C. Qiu, Y.H. Qian, C.J. Hamilton, S.D. McDougall, O.P. Kowalski, A.C. Bryce, R.M. De La Rue, J.H. Marsh, 'Monolithically integrated distributed Bragg reflector lasers for 1.5  $\mu\text{m}$  operation with band gap shifted grating', *Optical Materials, Vol.14, pp.193-196, 2000*
4. X.F. Liu, M.L. Ke, B.C. Qiu, A.C. Bryce, J.H. Marsh, 'Fabrication of Monolithically Integrated Mach-Zehnder Asymmetric interferometer Switch', *12<sup>th</sup> IEEE International Conference on Indium Phosphide and Related Materials Proceedings, WP2.19, 2000*

5. B.C. Qiu, X.F. Liu, M.L. Ke, H.K. Lee, A.C. Bryce, J.S. Aitchson, and J.H. Marsh, 'Monolithic fabrication of 2x2 crosspoint switches in InGaAs/InAlGaAs Multiple Quantum Wells Using Quantum Well Intermixing', *IEEE Photonics Technology Letters*, to be published in the December 2000 issue
  
6. B.C. Qiu, X.F. Liu, M.L. Ke, H.K. Lee, A.C. Bryce, J.S. Aitchson, and J.H. Marsh, 'Monolithic fabrication of 2x2 crosspoint switches in InGaAs/InAlGaAs Multiple Quantum Wells Using Quantum Well Intermixing', *Conference on Lasers and Electro-Optics (CLEO) Proceedings, CMI4, 2001*
  
7. B.C. Qiu, X.F. Liu, O.P. Kowalski, A.C. Bryce, J.H. Marsh, 'Precise Control of the Blue-shift of the Wavelength in InGaAs-InGaAsP Multiple Quantum Wells Using a Sputtered SiO<sub>2</sub> Technique', *12<sup>th</sup> IEEE Annual Lasers and Electro Optics Society (LEOS) Meeting Proceedings, Vol.1, TuV3, pp.309-310, 1999*

## Table of Contents

<b>1</b>	<b>Introduction</b>	<b>1</b>
<b>2</b>	<b>Investigation of reactive ion etching processes for InGaAs/AlInGaAs MQW material</b>	<b>13</b>
2.1	Introduction	14
2.1.1	Wet etching and dry etching	14
2.1.2	Reactive ion etching	16
2.1.3	Damage generated during dry etching process	19
2.2	Experimental investigation of dry etching process on InGaAs/AlInGaAs material system	20
2.2.1	The ET340 RIE machine	20
2.2.2	Wafer structure of InGaAs/AlInGaAs MQW material	21
2.2.3	ET340 CH <sub>4</sub> /H <sub>2</sub> process	22
2.2.4	The pre-cleaning stage of InGaAs/AlInGaAs dry etching process	26
2.2.5	Dry etching damage and the recovery	27
2.3	Summary	28
<b>3</b>	<b>Optical waveguide: theory and experiments</b>	<b>31</b>
3.1	Characteristics of guided optical waves in planar waveguide	32
3.2	Characteristics of guided optical waves in rectangular waveguides	35
3.3	Propagation loss in optical waveguide	38
3.3.1	Scattering loss	38
3.3.2	Absorption loss	41
3.3.3	Radiation losses	45
3.4	Optical waveguide: design and characterisation	49
3.4.1	The material structure	49
3.4.2	The design of optical waveguides	51
3.4.3	Characterization of semiconductor optical waveguides	54
3.5	Summary	63

<b>4 Multimode interferometer (MMI) couplers: theory, design, fabrication and characterization</b>	<b>67</b>
4.1 Introduction	68
4.2 Basic theory of MMI couplers	70
4.3 Modeling and design of MMI couplers	73
4.4 Fabrication and characterization of MMI couplers	77
4.4.1 Fabrication	77
4.4.2 Characterization of MMI couplers	82
4.5 Summary	85
<b>5 Quantum well intermixing</b>	<b>88</b>
5.1 The development of quantum well intermixing	89
5.1.1 Impurity induced disordering (IID)	90
5.1.2 Impurity free vacancy disordering (IFVD)	92
5.1.3 Laser induced disordering (LID)	94
5.1.4 Photo-absorption induced disordering (PAID)	95
5.1.5 Pulsed photo-absorption induced disordering (P-PAID)	96
5.1.6 Ion implantation induced disordering	96
5.2 Sputtering process induced disordering (SID)	97
5.3 Experimental Investigation on sputtering process induced disordering	98
5.3.1 Experiment set-up	99
5.3.2 Protection material	101
5.3.3 Annealing temperature	102
5.3.4 Time of sputtering process	104
5.3.5 Measurement of spatial resolution	105
5.4 SIMS measurement	106
5.5 Summary	113

<b>6</b>	<b>Novel multi-bandgap quantum well intermixing technique on 1.55 <math>\mu\text{m}</math> InGaAs/AlInGaAs and InGaAs/InGaAsP MQW material</b>	<b>119</b>
6.1	Introduction	120
6.2	Multi-bandgap structure addressed using SID	123
6.3	Assessment of the post-process material characteristics	129
6.4	Applications of the novel multi-bandgap quantum well intermixing technique	135
6.4.1	Integrated bandgap-tuned InGaAs/AlInGaAs and InGaAs/InGaAsP oxide stripe lasers and ridge waveguide lasers	135
6.4.2	Integrated 2x2 crosspoint optical switch	141
6.5	Summary	145
<b>7</b>	<b>Monolithically integrated Mach-Zehnder asymmetric interferometer demultiplexer: introduction and theory</b>	<b>150</b>
7.1	Introduction	151
7.2	Non-linearity in Semiconductor Optical Amplifier (SOA)	154
7.2.1	Carrier density change induced non-linearity	154
7.2.2	Kerr Effect	156
7.3	Operation of TOAD	158
7.3.1	X-couplers	160
7.3.2	the performances of Mach-Zehnder interferometer (MZI) and Sagnac interferometer (SI)	162
7.3.3	Operation of TOAD	166
7.4	Design of MZI-DMUX	169
7.5	Summary	173
<b>8</b>	<b>Monolithically integrated Mach-Zehnder asymmetric interferometer demultiplexer: fabrication and assessment</b>	<b>177</b>
8.1	Quantum well intermixing using sputtering process induced disordering	178
8.2	Pattern Transfer Process on InGaAs/AlInGaAs Structure	179
8.2.1	The photoresists	180

8.2.2	Pattern transfer process with SiN <sub>x</sub> as mask material	181
8.2.3	Pattern transfer process with Ti/SiO <sub>2</sub> as mask material	183
8.3	Dry etching process	186
8.4	Metal contact layer deposition and device bonding	187
8.5	Assessment of integrated Mach-Zehnder asymmetric interferometer demultiplexer	190
8.5.1	Experimental set-up	190
8.5.2	Assessment of semiconductor optical amplifier	191
8.5.3	Assessment of integrated Mach-Zehnder asymmetric interferometer demultiplexer	194
8.6	Summary	197
<b>9</b>	<b>Conclusions and future work</b>	<b>199</b>
9.1	Conclusion	200
9.1.1	Reactive ion etching (RIE) process for InGaAs/AlInGaAs MQW system	200
9.1.2	Theory, design and characterisation of waveguides	202
9.1.3	Modelling, design and fabrication of MMI couplers	202
9.1.4	Novel multi-bandgap quantum well intermixing technique on 1.55 μm InGaAs/AlInGaAs and InGaAs/InGaAsP MQW material	202
9.1.5	Applications of the novel multi-bandgap quantum well intermixing technique	204
9.1.6	Investigation of monolithically integrated Mach-Zehnder asymmetric interferometer demultiplexer	205
9.2	Future work	205

# CHAPTER 1

## INTRODUCTION

The demand for optical fibre communication capacity has been growing explosively over the years. The search for higher data rates seems endless both in local-area network (LAN) and long-haul systems, although the use of optical fibre systems has enabled multi-gigabit data transmission on a single fibre. Single mode optical fibre can provide a bandwidth of the order of tens of THz. This bandwidth is far from being fully exploited. Major R&D efforts have been focused on both modulation bandwidth of semiconductor lasers and the speed of the electronic devices. Progress in hetero-junction bipolar transistor (HBT) technology has enabled the multiplexing of digital signals up to the rate of 40 of Gbit/s [1]. Although higher speed drivers, receivers and multiplexers have been demonstrated [2], such efforts will become more and more difficult because of both technical and economical considerations.

There are other ways to overcome the difficulties. Instead of constructing a data stream electronically, recent research has provided some optical schemes. These schemes can be separated into Wavelength Division Multiplexing (WDM) and Optical Time-Division Multiplexing (OTDM).

In WDM, light sources, with slightly different wavelengths for different signal channels, transmit along the same optical fibre. It is possible to transmit up to 160 channels in present-day silica-based optical fibre in the 1.55  $\mu\text{m}$  transmission window. One of the significant features of WDM is flexible access. In WDM, every signal channel is independent of the others. Therefore they could be of a very different nature and carrying very different data, such as computer data and video signals. In an OTDM system, a high bit-rate data stream is constructed by

optically interleaving several lower bit-rate optical data streams. Therefore a strict timing or phase relationship has to be maintained throughout the system. However, OTDM does not necessarily require more than one light source for different signal channels and it is possible to utilize soliton transmission technology to overcome the dispersion limitation, so greatly enhancing the transmission distance. On the other hand, OTDM requires short optical pulses of low duty cycle to be generated in order for more channels to be multiplexed together to form a higher bit-rate data flow. A low duty cycle is also a requirement for soliton transmission. In many ways, OTDM and WDM are complementary in the sense that each seems to have its own advantages, which overcome the other's disadvantages.

Along the requirement for extremely high data rate operation, there is an increasing need for the monolithic integration of light source, modulation and detection devices, operating at wavelengths around 1.55  $\mu\text{m}$ . Similarly, there is considerable interest in photonic switching circuits, and these remain requiring low-insertion-loss waveguides and power splitting devices. By eliminating the influence due to vibration and alignment associated with discrete component, integration offers significant improvements in mechanical stability and reliability. Integration also brings device miniaturization, which leads to potential fabrication economy and enhanced performance, such as higher speed operation than their discrete counterparts. With such significant advantages mentioned above, becomes more and more important for the long wavelength (1.3 and 1.55  $\mu\text{m}$ ) telecommunication such as WDM and OTDM systems.

The fundamental requirement of monolithic integration is to define local areas, each with a different bandgap energy structure. This requires selective spatial control over local optical and electrical properties across substrate. Many different approaches have been developed, such as selective regrowth, selective area epitaxy and quantum well intermixing.

**Selective regrowth [3]** involves the multiple growth of different semiconductor structures on the same substrate. Generally, a semiconductor structure with bandgap energy  $E_{g1}$  is grown over the whole substrate first. After the etching in selected areas, a subsequent regrowth of another semiconductor structure with bandgap energy  $E_{g2}$  is carried out. Although it allows independent design of the semiconductor structures for different devices, selective regrowth requires critical etching and regrowth to achieve effective optical coupling between different devices. Expensive facilities such as metal organic vapor phase epitaxy (MOVPE) are necessary throughout the whole production process, and as well as being slow, yields tend to be low.

**Selective area epitaxy [4]**, by using silica masks, enables regions with different band gaps to be realised across a wafer in a single growth step. In this approach, the substrate is coated with a dielectric mask in which slots are opened using photolithography and etching. No growth takes place on top of the mask, but surface migration of the growth species can take place for some distance across the mask to the nearest opening. The growth rate, and hence the QW width, in the opened areas therefore depends on the width of the opening and the patterning of the mask. This technique is quite limited with regards to the bandgap changes that

can be achieved, and it cannot be used to pattern the bandgap across a wafer in two dimensions.

**Vertical coupled twin-waveguide (TG) structures** [5] use two strongly coupled waveguide layers, one over the other and separated by a cladding layer, which are grown in a single epitaxial growth step. Their material compositions are different so they have different bandgap energy values. These waveguides are optically coupled to each other so that light can transfer from one waveguide to the other. The upper layer can be grown as the active device structure and the lower one be the low loss waveguide structure. During the fabrication, the upper layer is removed except where a light source or amplifier is located so that light propagates in the low loss waveguides elsewhere. With this way, active devices can be integrated with low loss interconnecting waveguides.

**Quantum well intermixing (QWI)** [6]. A quantum well (QW) is a very thin semiconductor layer, typically  $\leq 10$  nm, sandwiched between 'barriers' of larger bandgap energy (Figure 1.1.1). Because of the bandgap difference, electrons and holes are trapped in the QW. The small size of the well causes the electron and hole energy levels to become quantized, and so the bandgap energy of a QW is larger than that of an equivalent bulk layer. Although a QW confines carriers (electrons/holes) efficiently, it does not confine the light efficiently as it is too thin. QW waveguide devices are therefore grown with a separate optical waveguide guiding layer, which is much thicker than a QW, to offer efficient optical confinement. This type of structure is called a separate confinement heterostructure (SCH). Being a simple and flexible technique for the

implementation of monolithic integration, QWI is a disturbance to the lattice of the semiconductor crystal resulting from the diffusion of impurities, excess native elements and/or vacancies. This disturbance changes the quantum well profile by intermixing the previously well-defined interface between wells and barriers, which induces the change of effective bandgap [7] (See Figure 1.1.1). Due to the fact that the optical overlap between the waveguide mode and a QW is much smaller than that between the waveguide mode and the waveguide layer, this change can leave a passive waveguide layer with identical dimensions and virtually the same refractive index. And the scattering and reflection losses at the interfaces between active and passive sections are, in principle, extremely small [6]. The first report of QWI was in GaAlAs/GaAs by W.D. Laidig, et al [8].

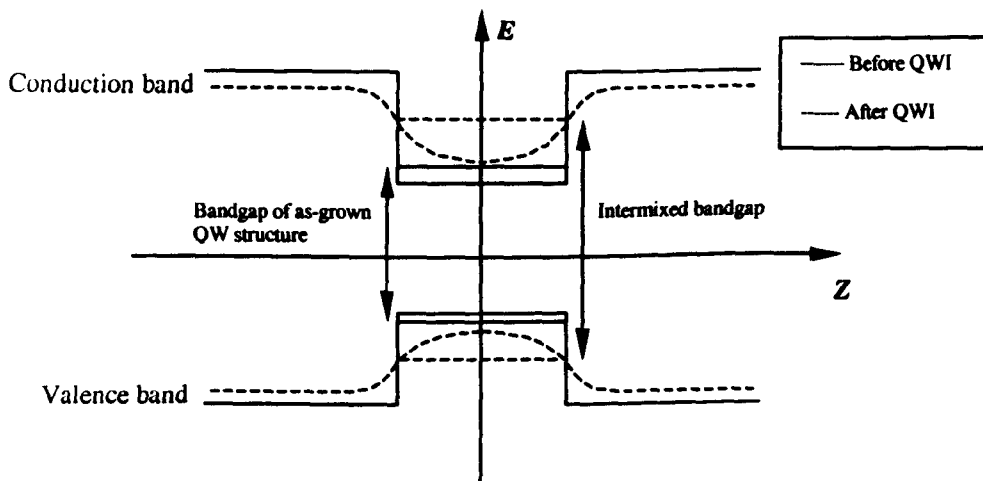


Figure 1.1.1 Diagram of quantum well bandgap structure and its change due to QWI

Since then, various methods have been developed. In the impurity induced disordering (IID) process [8], an impurity is introduced into an epitaxial wafer by using surface dopant diffusion or ion implantation. The presence of such an impurity enhances the atomic inter-diffusion during a subsequent anneal stage.

The introduction of impurities degrades the post-processed optical and electrical characteristics and makes IID unsuitable for forming active devices such as bandgap-tuned modulators and lasers.

Impurity free vacancy disordering (IFVD) [9] can yield large bandgap energy shifts without the disadvantages occurred in IID. Unfortunately, IFVD has poor reproducibility from run to run and poor discrimination between intermixed and unintermixed areas.

Some laser induced disordering (LID) techniques have been developed. In certain techniques, high power densities are used to melt the material and recrystallizing an alloy semiconductor [10]. Others utilise the transient melting of CW and pulse laser scanning to introduce encapsulant Si or other species into the epitaxial layers as a source for impurity-induced disordering [11-12]. Although LID processes are clearly effective, they can introduce the thermal shock damage when using high energy pulses mode and cause a potentially undesirable redistribution of dopants outside the active layers. Furthermore, melting the semiconductor and reforming result in complete intermixing and cannot be controlled to obtain partial bandgap shifts.

As an alternative to LID, photoabsorption induced disordering (PAID) [13] represents a promising QWI process, especially for the InGaAsP system, due to its poor thermal stability. This technique is layer-composition-selective and self-limiting. It is impurity free, uses low energy injection and does not involve a melt phase. Hence a material with high optical and electrical quality can be obtained.

However, due to its thermal nature, diffusion of heat leads to a poor spatial resolution of 100-200  $\mu\text{m}$ .

Pulsed photo-absorption induced disordering (P-PAID) [14] employs high-energy laser pulses from a Q-switched laser to irradiate the MQW material and produce transient heating in the crystal. Point defects, created by the thermal expansion, diffuse during a high temperature anneal and enhance the QWI rate. This technique offers a considerable improvement in spatial resolution, to better than 25  $\mu\text{m}$ . One of the potential problems of P-PAID is the possible formation of extend defects.

The use of ion implantation to generate point defects through high-energy impact with the crystal matrix elements has been used widely in many III-V material systems (AlGaAs, InP, etc.) [15]. Although it has been shown that InGaAsP/InP bandgap widened lasers can be successfully and reliably fabricated using this technique, the requirement for specialised facilities for implantation makes this technique relatively complicated and expensive.

Recently, a novel intermixing technique was developed in this department and in Intense Photonics Ltd., which has been used in a number of different material systems such as GaAs/AlGaAs, GaInP/AlGaInP, InGaAs/InGaAsP and InGaAs/InAlGaAs [16]. It is based on the introduction of an impurity during the deposition of sputtered SiO<sub>2</sub> and has so far proved highly successful for all of the above-mentioned material systems. By using PECVD SiO<sub>2</sub> with various thicknesses, effective control of the impurity introduction is possible and multiple

bandgap structures have been achieved. Assessment of the post-process material characteristics has shown that this process has considerable potential in multiple bandgap applications. In addition to its wide applicability, it is low cost and involves relatively simple processing stages.

The work described in this thesis is aimed at exploring the possibility of monolithic integration of multi-bandgap opto-electronic devices. These devices include multi-wavelength light sources and demultiplexers, in the InGaAs/AlInGaAs material system. Integration is carried out using the quantum well intermixing techniques effective control of the impurity introduction, especially the improved IID process.

In Chapter 2, the reactive ion etching process is discussed, especially related to the InGaAs/AlInGaAs system. In Chapter 3, based on a theoretical approach, the design of ridge waveguides is described. Assessment of three kinds of waveguide is also given in this chapter. Chapter 4 is concerned with the modelling, design, fabrication and assessment of 3-dB MMI couplers. In Chapter 5, several QWI techniques are discussed first. The recently developed intermixing technique, based on SID, is then addressed. Chapter 6 described the applications of this novel QWI technique. Multi-wavelength light sources are demonstrated, as well as a 2x2 crosspoint optical integrated switch. In Chapter 7, the principle of the terahertz optical asymmetric demultiplexer is investigated and the design of a MZI type demultiplexer is described. Chapter 8 documents the fabrication and assessment of MZI type demultiplexers. In Chapter 9, the conclusions of the work are discussed.

## Reference

- [1] J. Godin, P. Andre, J.L. Benchimol, P. Berdaguer, S. Blayac, J.R. Burie, P. Desrousseaux, and A.M. Duchenois, '40 Gbit/s optical communication: InP DHBT technology circuits and system experiments', *Proceeding of GaAs IC'99*, pp.185-188, 1999
- [2] H. Yoshimura, 'Future photonic networks and the role of InP-based devices', *12<sup>th</sup> IEEE International Conference on Indium Phosphide and Related Materials Proceedings*, PLEN 1, 2000
- [3] M. Aoki, M. Suzuki, H. Sano, T. Kawano, T. Ido, T. Taniwatari, K. Uomi and A. Takai, 'InGaAs/InGaAsP MQW electroabsorption modulator integrated with a DFB laser fabricated by band-gap energy control selective-area MOCVD', *IEEE J. Quantum Electronics*, Vol.29, pp.2088-2096, 1993
- [4] M. Gibbon, J.P. Stagg, C.G. Cureton, E.J. Thrush, C.J. Jones, R.E. Mallard, R.E. Pritchard, N. Collins, and A. Chew, 'Selective area low-pressure MOCVD of GaInAsP and related materials on planar InP substrates', *Semiconductor Science & Technology*, Vol.8, pp.998-1010, 1993
- [5] Y. Suematsu, M. Yamada, and K. Hayashi, 'A multi-hetero AlGaAs laser with integrated waveguide', *Proceeding of IEE (Lett)*, Vol.63, pp.208-209, 1975
- [6] J.H. Marsh, 'Quantum well intermixing', *Semiconductor Science & Technology*, Vol.8, pp.1136-1155, 1993
- [7] V.W.D. Laidig, N. Holonyak Jr., M.D. Camras, K. Hess, J.J. Coleman, P.D. Dapkus, and J. Bardeen, 'Disordering of an AlGaAs/GaAs super-lattice by impurity diffusion', *Applied Physics Letter*, Vol.38, pp.776-778, 1981

- [8] L.J. Guido, N. Holonyak Jr., K.C. Hsieh, R.W. Kaliski, W.E. Plano, R.D. Burnham, R.L. Thornton, J.E. Epler, and T.L. Paoli, 'Effect of dielectric encapsulation and As overpressure on Al-Ga interdiffusion in  $\text{Al}_x\text{Ga}_{1-x}\text{As}$  quantum well heterostructures', *J. of Applied Physics*, Vol.55, pp.540-542, 1989
- [9] J.D. Ralston, A.L. Moretti, R.K. Jain, and F.A. Chambers, 'Intermixing of  $\text{Al}_x\text{GaAs}/\text{GaAs}$  superlattices by pulsed laser irradiation', *Applied Physics Letter*, Vol.50, pp.1817-1819, 1987
- [10] J.E. Epler, F.A. Ponce, F.K.J. Endicott and T.L. Paoli,, 'Laser-induced disordering of  $\text{GaAs}/\text{AlGaAs}$  superlattice and incorporation of Si impurity', *Applied Physics Letter*, Vol.49, pp.1447-1449, 1986
- [11] A. Rys, Y. Shieh, A. Compaan, H. Yao, and A. Bhat, 'Pulsed laser annealing of GaAs implanted with Se and Si', *Optical Engineering*, Vol.29, pp.329-338, 1990
- [12] C.J. McLean, J.H. Marsh, R.M. De La Rue, A.C. Bryce, B. Garrett, and R.W. Glew, 'Layer selective disordering by photoabsorption-induced thermal-diffusion in  $\text{InGaAs}/\text{InP}$  based multiquantum well structures', *Electronics Letter*, Vol.28, pp.1117-1119, 1992
- [13] C.J. McLean, A. McKee, G. Lullo, A.C. Bryce, R.M. De La Rue, and J.H. Marsh, 'Quantum-well intermixing with high spatial selective using a pulsed-laser technique', *Electron. Letter*, Vol.31, pp.1285-1286, 1995
- [14] J.P. Noel, D. Melville, T. Jones, F.R. Shepherd, C.J. Miner, N. Puetz, K. Fox, P.J. Poole, Y. Feng, E.S. Koteles, S. Charbonneau, R.D. Goldberg, I.V. Mitchell, 'High-reliability blue-shifted  $\text{InGaAsP}/\text{InP}$  lasers', *Applied Physics Letter*, Vol.69, pp.3516-3518, 1996

[15] O.P. Kowalski, C.J. Hamilton, S.D. McDougall, J.H. Marsh, A.C. Bryce, R.M. De La Rue, B. Vögele, C.R. Stanley, C.C. Button, J.S. Roberts, 'A universal damage induced technique for quantum well intermixing', *Applied Physics Letter*, Vol.72, pp.581-584, 1998

## CHAPTER 2

### INVESTIGATION OF REACTIVE ION ETCHING PROCESSES FOR InGaAs/AlInGaAs MQW MATERIAL

In this chapter, a general description of the dry etching process is presented. A series of experiments is carried out to determine the relationship between etching results and etching conditions, especially for the InGaAs/AlInGaAs material system.

## 2.1 Introduction

### 2.1.1 Wet etching and dry etching

Etching is an integral part of device manufacture. In general, when removing semiconductor material to transfer desired patterns into solid substrates, there are two basic techniques: wet etching [1], involving chemicals in a liquid solution, and dry etching, involving reactive species generated in a plasma.

Wet etching can be highly selective and fast and involves immersing the substrates into the required chemical solutions to remove the material. Normally, wet etching is not directional, i.e., etching occurs in the lateral as well as the vertical direction, as shown in Figure 2.1.1(a). This leads to an undercutting of the mask, which is normally highly undesirable, especially when the mask is very narrow or the required sidewall is very sharp. Another characteristic of wet etching is the etching rate depends on the density of semiconductor atoms, i.e., the orientation of the material and also on the chemical nature of the surface. For all zincblende or diamond structures the wet etch rate of (100) is faster than that of other orientations, so wet etching is not suitable for transferring complicated patterns.

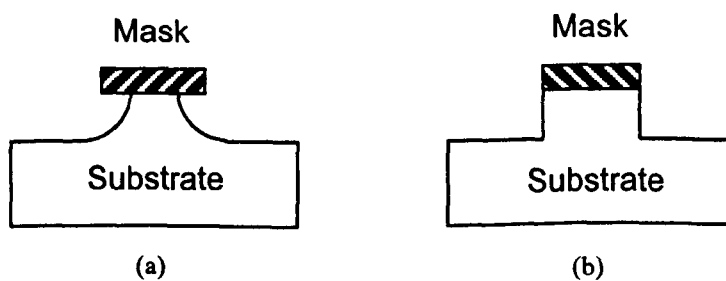


Figure 2.1.1 Typical profiles of (a) wet etching and (b) dry etching processes

Etching processes using corrosive or sputtering gases in the state of plasma come under the heading of dry etching [1]. The etching occurs predominantly in the direction of ion incidence, which means the dry etching process is anisotropic as shown in Figure 2.1.1(b). During the dry etching process, the sample is bombarded by a flux of ions that leads to physical sputtering or chemical reactions, or a mixture of both.

The physical action of the energetic ions on the substrate can be described as the removal of material purely through momentum transfer – the atoms are knocked out by the impact of the flux of ions. Purely physical etching is not widely used as the etching rate tends to be slow, and the profiles of an etched feature are not vertical.

In chemical reaction, the ion is selected so that it (or an associated radical) reacts chemically with the substrate material to create a chemical product that is volatile at the process pressure and temperature so that it can be extracted away.

Dry etching has several advantages:

- The degree of undercutting of the masks can be controlled effectively (particularly important for deep etching), which means it is possible to etch small features and to maintain accurate pattern transfer.
- The degree of selectivity between substrate materials can be varied with the process parameters.
- The etching of material by reaction with chemically active radicals in a glow discharge is dry and clean, which increases the reproducibility and

A typical RIE process offers process simplification and better dimensional control compared to the existing wet-etching processes.

- The etching process is not orientation-dependent, which means that many complicated desired profiles can only be obtained by dry etching.
- Reproducibility is increased due to better dimensional control compared to the existing wet etching process.

### 2.1.2 Reactive ion etching

Reactive-ion etching (RIE) [2] is a very popular dry etching process for transferring patterns onto III-V semiconductors. A simplified schematic diagram of a capacitively coupled RIE system is shown in Figure 2.1.2.

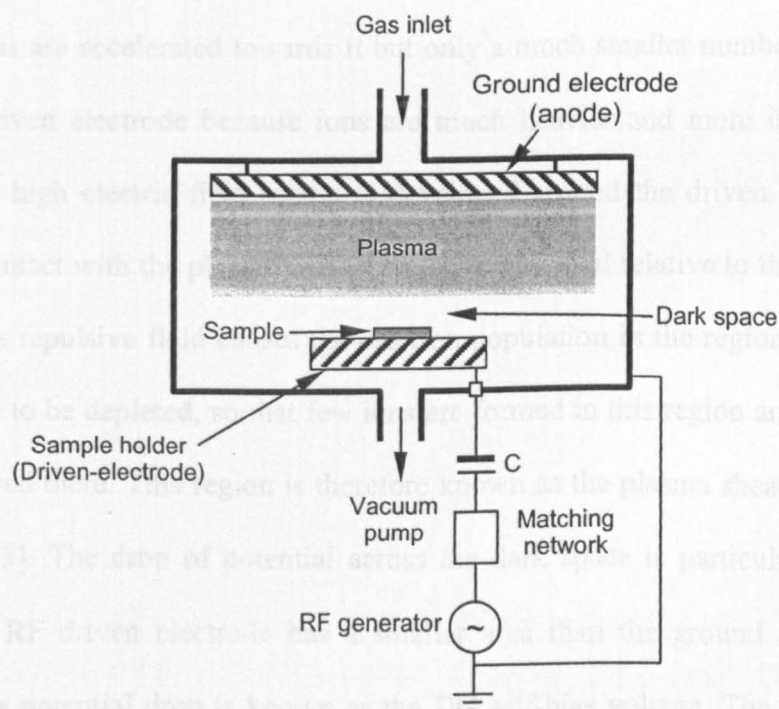


Figure 2.1.2 simplified schematic diagram of a RIE system

A typical reactive ion etch machine has a vacuum chamber which consists of two parallel electrodes. The top electrode (anode) is grounded while the bottom one (cathode) is driven by a radio frequency (RF) signal generator, connected through a capacitor and an impedance matching circuit. The etching gas is introduced into the chamber, which is maintained as a pumped vacuum environment. Free electrons in the chamber gain energy from the RF electron field. The energetic electrons collide with the gas molecules and so ions are formed. The combination of electrons and ions forming the etching gas is known as plasma. The response of the plasma is different in positive and negative cycles of RF driving. In the positive cycle, the driven electrode is positive and electrons are accelerated towards the driven electrode, which causes a significant accumulation of negative charge due to the high mobility of electrons. When the driven electrode is negative, ions are accelerated towards it but only a much smaller number of ions reach the driven electrode because ions are much heavier and more immobile. Therefore, a high electric field region is developed around the driven electrode surface in contact with the plasma, with a negative potential relative to the plasma volume. This repulsive field causes the electron population in the region close to the electrode to be depleted, so that few ions are formed in this region and a glow is not observed there. This region is therefore known as the plasma sheath, or the dark space [3]. The drop of potential across the dark space is particularly high because the RF driven electrode has a smaller area than the ground electrode (anode). This potential drop is known as the DC self-bias voltage. The DC self-bias is proportional to the amplitude of the RF signal and the ratio of the ground electrode surface area to the RF driven surface area. In most RIE apparatus, the

driven electrode is much smaller than the ground electrode in order to obtain a high self-bias.

The high drop of the negative potential causes a flow of positive ions from the plasma volume across the dark space to the driven electrode. The pressure used in the reactive ion etch machine is very low (5- 100 mTorr), therefore the mean free path of the ions is long, so they are not randomised in direction while traversing the plasma sheath. If the substrate is placed on the driven electrode, the ions will strike the substrate from a vertical direction. Etching will occur in this direction if the ions react chemically with the semiconductor to form volatile compounds which are then pumped away. Etching will also occur due to physical sputtering caused by energetic ion bombardment. Therefore RIE utilises both chemical and physical etching mechanisms.

We see that using electrodes of different area sizes, placing the sample on an electrode and using relatively low pressure all lead to an ion beam which is energetic and directed vertically at the sample. This combination leads towards achieving anisotropic etching in a RIE machine.

The basic processes involved in RIE are [4]:

1. The etching species (the reactant) is generated in the plasma.
2. The reactant is then transported by diffusion to the surface of substrate.
3. The reactant is adsorbed on the surface.
4. Chemical reaction takes place between the reactant and substrate material to form volatile compounds, along with physical effects such as ion bombardment.

5. These compounds are desorbed from the surface, and pumped out by the vacuum system.

### **2.1.3 Damage generated during dry etching process**

In reactive ion etch processes, the energetic ions bombard the material and can cause damage to the material being etched [5].

When ions strike a surface, the surface material is removed and damage is induced beneath the surface at the same time. The sidewalls, if vertical, are not at first sight bombarded by the incident ions. They will, however, be bombarded by ions re-emitted from or ricocheting from the etched surface and by ions attracted by the image charge they induce in the semiconductor.

As a result, the electrical and optical characteristics of the material degrade after dry etching [6-9]. The presence of damage manifests itself in many ways. Optically it results in reduced radiation recombination efficiency, leading to a decrease of the photoluminescence intensity of the material. Fatally, such damage leads to poor operation of semiconductor lasers. Electrically it results in reduced carrier mobility and carrier density in the material. This will decrease the material's conductivity, leading to lower transconductance, lower speed and increased noise figure in transistors.

*The energy and size of the impinging ion determine the impact it will bring to the lattice. When the incident ion strikes the material, the energy and momentum transfer from the ion to the material can make several things happen. The ions*

may either react chemically with the material, be reflected off the surface, or penetrate the material. If the ion enters the material, the structure of the crystalline lattice may be disturbed by the creation of vacancies, interstitials, or dislocations. Energy can also be released in the form of photons, phonons (heat), or electrons during the many collisions that occur in the material.

## **2.2 Experimental investigation of dry etching process on InGaAs/AlInGaAs material**

Currently, the reactive ion etching process based on a methane/hydrogen ( $\text{CH}_4/\text{H}_2$ ) mixture is the most widely used technique for dry etching of indium (In) containing semiconductor systems, as it offers better anisotropy [10-11] than RIE using chlorine (Cl) and bromine (Br) containing etching compounds [12]. Also,  $\text{InCl}_3$  and  $\text{InBr}_3$  are not very volatile (hence the need for 'hot'  $\text{SiCl}_4$ ). Although much work has been published on  $\text{CH}_4/\text{H}_2$  etching, there are many different RIE machines used in research establishments and the etching conditions such as gas flow rates, chamber pressure and DC bias, etc., are different from machine to machine. In this section, we will focus on the etching rates and surface morphology of the  $\text{CH}_4/\text{H}_2$  etching process on InGaAs/AlInGaAs material system.

### **2.2.1 The ET340 RIE machine**

The dry etching machine used in our research is an Electrotech SRS Plasmafab 340 RIE machine. The area ratio of the ground electrode to the RF driven

electrode is 3.3:1, and both are made of the aluminium (Al). The RF driven electrode, with a diameter of 17 cm, is coated with titanium oxide and the sample is placed on it. The temperature of the driven electrode is regulated at a constant 30°C during the process by a circulating cooling system. The ET340 permits control of the gas flow rate, gas ratio, RF power and chamber pressure.

## 2.2.2 Wafer structure of InGaAs/AlInGaAs MQW material

The wafer structure used in our research was InGaAs/AlInGaAs MQW, grown on a (100)-oriented n-type InP substrate either by molecular beam epitaxy (MBE) or by MOCVD. It contained six InGaAs quantum wells of 7 nm width with 8 nm wide InGaAs/AlInGaAs barriers. The structure is described in Table 2.2.1.

Table 2.2.1 Material structure used in the design of MMI couplers

Repeats	Thick. (nm)	Material	Dopant	Type	Conc(cm <sup>-3</sup> )
1	200	GaIn <sub>0.53</sub> As	Be*	p	5.0E+18
1	800	In <sub>0.52</sub> AlAs	Be*	p	5.0E+17
1	250	Al <sub>0.2</sub> In <sub>0.525</sub> GaAs		I	
1	7	In <sub>0.53</sub> GaAs QW		I	
5	8	Al <sub>0.2</sub> In <sub>0.525</sub> GaAs Barrier		I	
5	7	In <sub>0.53</sub> GaAs QW		I	
1	250	Al <sub>0.2</sub> In <sub>0.525</sub> GaAs		I	
1	5000	In <sub>0.52</sub> AlAs	Si	n	5.0E+17
1		InP	Si	n+	5.0E+18

\*The dopants in these two layers are Be for the wafers grown by MBE, and Zn for the wafers grown by MOCVD.

### 2.2.3 ET340 CH<sub>4</sub>/H<sub>2</sub> process

The CH<sub>4</sub>/H<sub>2</sub> etching process is generally thought to be the reverse of the MOCVD growth process. It has been shown that PH<sub>3</sub> is the primary phosphorus containing volatile product and it is postulated that In(CH<sub>3</sub>)<sub>3</sub> is the primary indium containing volatile product [11]. (2.2.1)-(2.2.3) show the possible dissociation processes of the etching gases and the reaction with InP.



From above equations, it appears CH<sub>4</sub> is responsible for reacting and removing the group III elements such as In, while H<sub>2</sub> is responsible for removing P and other group V elements. During the etching process, a layer of polymer can be formed on the mask material. It is believed to be an organic substance originating from the CH<sub>4</sub> because the thickness of the polymer is proportional to the CH<sub>4</sub> content.

Research has disclosed that, during the etching process, CH<sub>4</sub>/H<sub>2</sub> tends to give different etching rates for the InGaAs/InGaAsP and for the InP that normally forms the cladding layer. It was also found that, by mixing O<sub>2</sub> with the CH<sub>4</sub>/H<sub>2</sub> during the etching process, the smoothness and sharpness of the sidewall could be much improved. In addition, O<sub>2</sub> can remove the polymer created during the etching [13]. Table 2.2.2 gives a typical recipe for InGaAs/InGaAsP etching in this Department. An etching rate of around 59 nm/min. can be obtained using this recipe, with very good sidewall features.

Table 2.2.2 Typical CH<sub>4</sub>/H<sub>2</sub> process recipe for the InGaAs/InGaAsP system

Etching Gas	CH <sub>4</sub> / H <sub>2</sub> / O <sub>2</sub>
Flow Meter Reading (%)	72 / 100 / 8
Correct Flow (Sccm)	14.4 / 100 / 0.4
Etching Pressure (mTorr)	50
RF Forward Power (W)	55
RF Bias Voltage (-V)	500
Etching Rate (nm/Min.)	59 ± 2

Unfortunately, this recipe cannot be applied to the InGaAs/AlInGaAs material systems shown in Table 2.2.1 because the Al is very easily oxidised. The resulting Al<sub>2</sub>O<sub>3</sub> is very difficult to remove so further etching is prevented. No O<sub>2</sub> can be therefore used in the gas when etching InGaAs/AlInGaAs. The direct result of the absence of O<sub>2</sub> in the etch process is that the polymer deposited during the process may cause some problems.

First, the etching rate tends to decrease, as there is no O<sub>2</sub> to help remove the polymer deposited on the substrate surface. The creation rate of the polymer is proportional to the gas flow rate. If the gas flow rate is too large, the polymer deposited on the surface will not be sputtered away by ions and more and more polymers will deposit on the surface. Eventually, etching will stop. Considering that the dry etching damage is proportional to the intensity of ion bombardment

and ion energy, in turn determined by the RF power [14], a low RF power is preferred so that the substrate can maintain good optical and electronic characteristics. On the other hand, the etching will stop if the RF power is too low to offer a high enough sputtering rate for polymer removal, so a suitable RF power level is also important to the process.

One of the keys to successful etching is parameter selection and accurate process control. Here the gas flow rate and RF power were studied so that effective etching could be obtained, as well as low dry etching damage.

In the experiment, the RF power and the gas flow rate were varied. To verify the etching result, the etching rates were measured and the surface morphology of the post-process samples was observed. First, a layer of 200 nm PECVD (plasma enhanced chemical vapour deposition) SiO<sub>2</sub> was deposited on some InGaAs/AlInGaAs samples. The samples were patterned using photolithography and a CHF<sub>3</sub> dry etching process in the BP80 machine to form suitable masking patterns. The samples were then etched using CH<sub>4</sub>:H<sub>2</sub> under different conditions. After that, the mask of SiO<sub>2</sub> was removed and the profiles were measured using a Dektak<sup>3</sup>ST surface profiler from SLOAN TECHNOLOGY Ltd. to calculate the etching rate. The surface morphology was checked with a HITACHI S800 scanning electron microscope (SEM).

It was found that, as the RF power was increased, the surfaces became increasingly rough, while the sidewalls became sharper. When RF power was reduced to 20 W, the etching rate was quite low (20 nm/min.) and frequently

etching failed due to polymer deposition on the substrate surface. This was believed to be a result of the RF power being too low to remove the polymer generated on the substrate surface.

Table 2.2.3 The ET340 etching conditions and etching rates

	Test-1	Test-2	Test-3	Test-4	Test-5	Test-6	Test-7
Etching Gas	CH <sub>4</sub> /H <sub>2</sub>						
Flow Meter Reading (%)	36/100	36/100	36/100	36/100	36/100	36/100	30/50
Correct Flow (Scm)	7.2/100	7.2/100	7.2/100	7.2/100	7.2/100	7.2/100	6/50
Etching Pressure (mTorr)	50	50	50	50	50	40	30
RF Forward Power (W)	30	40	60	70	80	60	50
Etching Rate (nm/Min.)	20*	30	38	43	46	35	30

\* etching failed frequently

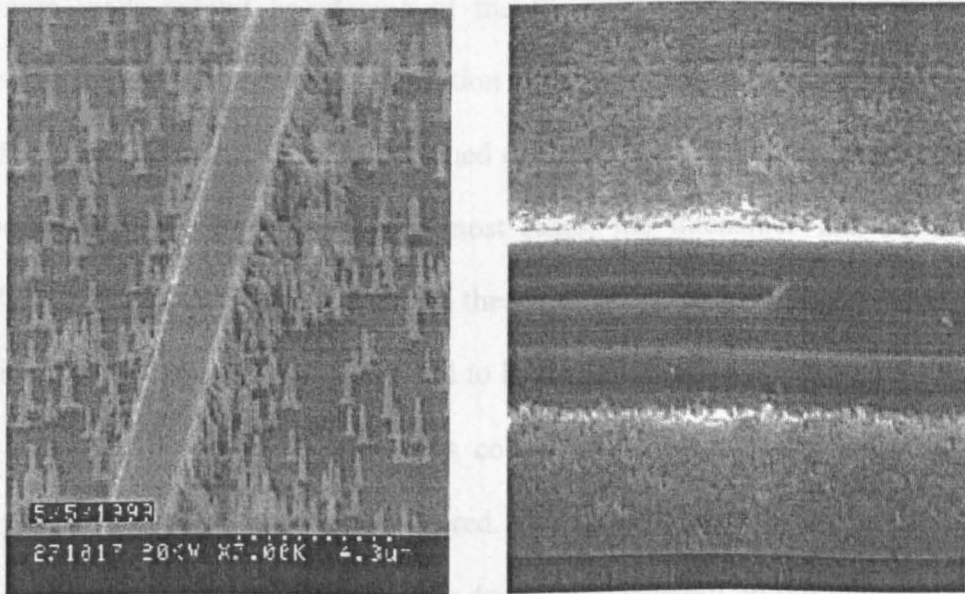
Table 2.2.4 'Standard' ET340 etching conditions and etching rates

Etching Gas	CH <sub>4</sub> /H <sub>2</sub>
Flow Meter Reading (%)	36 / 100
Correct Flow (Scm)	7.2 / 100
Etching Pressure (mTorr)	50
RF Forward Power (W)	60
Etching Rate (nm/Min.)	38

Considering the balance between the etching rate, sidewall sharpness and dry etching damage (proportional to the RF power), a group of process parameters was chosen as our 'standard' process for the InGaAs/AlInGaAs material system (Table 2.2.4).

#### 2.2.4 The pre-cleaning stage of InGaAs/AlInGaAs dry etching process

During the experiments, it was found that, occasionally, the dry etching stopped in some areas, as shown in Fig.2.2.1 (a). This was believed to be mainly due to small amount of  $O_2$  present in the etching chamber reacting with Al to form  $Al_2O_3$  on some areas during the process. This led to the prevention of further etching in such areas, as  $Al_2O_3$  is quite hard to etch. Sometimes this happened to the whole etching surface, as shown in Fig.5.2.1 (b).



(a)

(b)

Fig.2.2.1. Effect of  $O_2$  contamination in AlInGaAs dry etch

This really has become the major reason of fabrication failure. It was found that the  $O_2$  came from the cleaning stage prior to the etching process, in which  $O_2$  was used to clean the chamber. It was also found that, if the pumping stage before etching was not long enough, the residual  $O_2$  could cause the fatal result. After some experiments, an improved pre-cleaning stage was developed with significant success. First, the chamber was cleaned with  $O_2$  for 10 minutes, followed by  $H_2$  cleaning for 20 minutes. Then the chamber was pumped to the desired vacuum level and  $CH_4/H_2$  etching gas was introduced into the chamber. After 1 minute, the RF source was switched on and etching started.

### **2.2.5 Dry etching damage and the recovery**

In his work [15], Qiu investigated the damage generated during the ET340 RIE dry etching process, using the photo photoluminescence (PL) method combined with the multiple quantum well probe technique. It has been found that damaged quantum wells exhibit broadening of the PL peaks, as well as a significant decrease of PL intensities. The degradation of the quantum wells is proportional to the RF power. Experiment has confirmed that a post-dry-etching annealing stage is very useful for PL recovery. In most cases, the intensities and PL width (FWHM) can be restored to those of the as-grown values. This effect may be ascribed to the removal of damage and to hydrogen passivation. However, it was also found that very high RF powers could induce permanent damage to the quantum wells that could not be recovered. This strongly indicates that a relatively low RF power is preferred to eliminate dry etching damage, in our situation, less than 60 W.

In this work, no similar study was carried out. However some experiments were carried out to confirm the necessity of the post-dry-etching annealing stage for the InGaAs/AlInGaAs system. In the experiment, ridge waveguide lasers were made on three InGaAs/AlInGaAs samples from the same wafer. The width of ridge was 5  $\mu\text{m}$  and the etching depth was 1  $\mu\text{m}$ . Lasers on Sample A were made using wet etching, while lasers on Sample B and C used the same dry etching process except that a post-dry-etching annealing stage of 500°C/60s was applied to Sample C. It was found that lasers of 400  $\mu\text{m}$  cavity length from Sample A gave the best performance. Those from sample C exhibited about an 11% increase in threshold current. However, no device from Sample B worked. This did prove that the post-dry-etching annealing stage is vital for active device fabrication on InGaAs/AlInGaAs material.

### **2.3 Summary**

In this chapter, a general description of the RIE dry etching process has been presented. The damage generated during the process has been discussed. A series of experiments, carried out on a ET340 RIE machine, was used to determine the optimal etching conditions, especially for the InGaAs/AlInGaAs material system. The operation of ridge waveguide lasers fabricated with different processes has shown that a proper post-dry-etching annealing stage is compulsory for InGaAs/AlInGaAs active device fabrication when using dry etching.

## Reference

- [1] S.M. Sze, 'Semiconductor Devices Physics and Technology', John Wiley & Sons, pp.457, 1985
- [2] D. Bollinger, S. Iida, O. Mastsumoto, 'Reactive ion-etching: its basic and future', *Solid State Technology*, May, pp.111, 1984
- [3]. B. N. Chapman, "Glow Discharge Processes" John Wiley & Sons, pp.97, 1980
- [4] S. M. Sze, 'VLSI Technology overview and Trends', *Japanese J. of Physics*, Vol.22, pp.3, 1983
- [5]. S. K. Murad, M. Rahman, N. Johnson, S. Thomas, S. P. Beaumont, and C. D. W. Wilkinson, "Dry etching damage in III-V semiconductors," *J. of Vacuum Science & Technology*, Vol.B14, pp.3658-3662, 1996
- [6] S.J. Pearton, W.S. Hobson, U.K. Chakrabarti, G.E. Derkits, and A.P. Kinsella, 'Use of hydrogenated chlorofluorocarbon mixtures for reactive ion etching of In-based III-V semiconductors', *J. of Vacuum Science & Technology*, Vol.B8, pp.1274-1284, 1990
- [7] T.R. Hayes, W.C. Dautremont-Smith, H.S. Luftman, and J.W. Lee, 'Passivation of acceptors in InP resulting from  $\text{CH}_4/\text{H}_2$  reactive ion etching', *Applied Physics Letters*, Vol.55, pp56-58, 1989
- [8] M. Moehrle, 'Hydrogen passivation of Zn acceptors in InGaAs during reactive ion etching', *Applied Physics Letter*, Vol.56, pp.542-544, 1990
- [9] D.G. Yu, B.P. Keller, A.L. Holmes, Jr., and E.L. Hu, 'Analysis of InP etched surface using metal-organic chemical vapor deposition regrown quantum well structures', *J. of Vacuum Science & Technology*, Vol.B13, pp.2381-2385, 1995

- [10] E. Andideh, I. Adesida, T. Brock, C. Caneau, and V. Kermidas, 'Short-period grating for long-wavelength optical devices', *J. of Vacuum Science & Technology*, Vol.**B7**, pp.1841-1845, 1989
- [11] T.R. Hayes, M. A. Dreisbach, P.M. Thomas, W.C. Dautremont-Smith, and L.A. Heimbrook, 'Reactive ion etching of InP using CH<sub>4</sub>/H<sub>2</sub> mixtures – mechanism of etching and anisotropy', *J. of Vacuum Science & Technology*, Vol.**B7**, pp.1130-1140, 1989
- [12] K. Takimoto, K. Ohnaka, and J. Shibata, 'Reactive ion etching of InP with Br<sub>2</sub> containing gases to produce smooth, vertical walls – fabrication of etched-facet lasers', *Applied Physics Letters*, Vol.**54**, pp.1947-1949, 1989
- [13] S.E. Hicks, C.D.W. Wilkinson, G.F. Doughty, A.L. Burness, I. Henning, M. Asghari, and I. White, 'Reactive ion etching of low-loss mirrors in InP/InGaAsP/InP heterostructures using CH<sub>4</sub>/H<sub>2</sub>/O<sub>2</sub> chemistry', *Proceeding of European Conference on Integrated Optics*, pp.2-36, 1993
- [14] B.C. Qiu, B.S. Ooi, A.C. Bryce, S.E. Hicks, C.D.W. Wilkinson, R.M. De La Rue, and J.H. Marsh, 'Reduced damage reactive ion etching process for fabrication of InGaAs/InGaAsP multiple quantum well ridge waveguide lasers', *J. of Vacuum Science & Technology*, Vol.**B16**, pp.1818-1822, 1998
- [15] B. Qiu, 'Photonic integration in InGaAs/InGaAsP multiple-quantum well laser structure using quantum well intermixing', *thesis of University of Glasgow*, pp.110-116, 1998

## CHAPTER 3

### OPTICAL WAVEGUIDE: THEORY AND EXPERIMENTS

The optical waveguide is the basic component of optoelectronic integration. It is used to interconnect various active and passive components in optoelectronic integrated circuits (OEIC). In this chapter, the basic results from waveguide theory, for both planar and rectangular dielectric waveguides, are reviewed. The major sources of propagation loss in optical waveguides are discussed. The design and assessment of several kinds of waveguides, using InGaAs/AlInGaAs, are documented.

### 3.1 Characteristics of guided optical waves in planar waveguides

The propagation behavior of light in a waveguide can be described by Maxwell's equations. Making the assumptions of  $\rho = 0$  and  $J = 0$ , we can derive the wave equation as:

$$\nabla^2 E = \mu\epsilon \frac{\partial^2 E}{\partial t^2} = \frac{n^2}{c^2} \frac{\partial^2 E}{\partial t^2} \quad (3.1.1)$$

Here,  $n = \sqrt{\epsilon_r}$  is the refractive index of the material,  $\epsilon_r$  is the relative dielectric constant,  $\epsilon_0$  is the dielectric constant of vacuum,  $\mu$  is the magnetic permeability, and  $c = (\mu\epsilon_0)^{-1/2}$  is the light velocity in vacuum.

Normally, the electric field  $E$  is a function of space position  $(x, y, z)$  and time  $t$ . To simplify the problem,  $E(x, y, z, t)$  is assumed to consist of two independent parts, a spatial dependence of the electric field  $E(x, y, z)$  and an exponential  $e^{j\omega t}$  describing the time-variation,

$$E(x, y, z, t) = E(x, y, z)e^{j\omega t} \quad (3.1.2)$$

With this assumption, the wave equation can be reduced to

$$\nabla^2 E(x, y, z) = -n^2 \frac{\omega^2}{c^2} E(x, y, z) = -n^2 K_0^2 E(x, y, z) \quad (3.1.3)$$

where  $K_o$  is the propagation constant in free space defined as  $K_o = \omega/c = 2\pi/\lambda_o$ , and  $\lambda_o$  is the wavelength of light in free space.

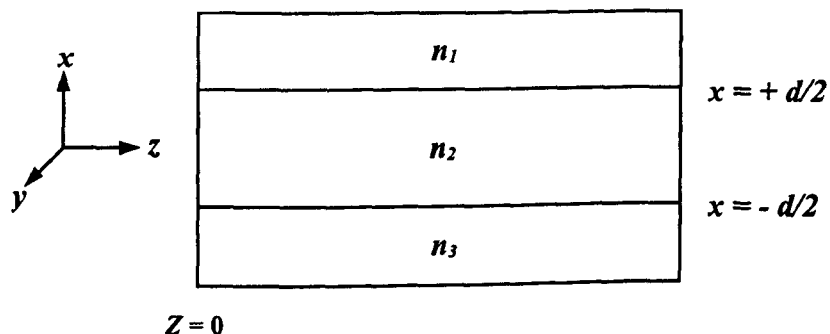


Fig.3.1.1 Schematic Structure of the planar optical waveguide

The boundary conditions at the interfaces of the waveguide lead to the waves travelling in distinct modes, spatial distributions of optical energy in one or more dimensions. The simplest waveguides are one-dimensional planar waveguides (See Fig.3.1.1) in which the optical waves are guided in one dimension. The refractive index of the central layer is selected to be higher than that of the other two layers,  $n_1 = n_3 < n_2$ . In such a three layer planar waveguide, the light is confined or “guided” when the light propagates along the waveguide.

For simplicity, only TE polarisation will be considered in the first instance. In this case, the spatial dependence of the electric field  $E(x,y,z)$  has only one component,  $E_y(x)$ . The  $E$  of a wave travelling in the  $z$  direction, with propagation constant  $\beta$  can be written as:

$$E(x, y, z) = E_y(x)e^{j(-\beta z)} \quad (3.1.4)$$

Combining the above equation with (3.1.3), we can obtain,

$$\frac{d^2 E_y(x)}{dx^2} - (\beta^2 - n_i^2 K_0^2) E_y(x) = 0 \quad (3.1.5)$$

where  $n_i$  ( $i=1, 2, 3$ ) are the refractive indices of the three different layers. With a series of derivation [1], we can obtain the even mode solutions as,

$$E_y(x) = A_e \cos(\kappa x) \quad |x| < d/2 \quad (3.1.6a)$$

$$E_y(x) = A_e \cos\left(\frac{\kappa d}{2}\right) \exp(-\gamma|x| - \frac{d}{2}) \quad |x| > d/2 \quad (3.1.6b)$$

and the odd mode solutions as,

$$E_y(x) = A_o \sin(\kappa x) \quad |x| < d/2 \quad (3.1.6c)$$

$$E_y(x) = \frac{x}{|x|} A_o \sin\left(\frac{\kappa d}{2}\right) \exp(-\gamma|x| - \frac{d}{2}) \quad |x| > d/2 \quad (3.1.6d)$$

where,

$$\gamma^2 = \beta^2 - n_1^2 K_0^2 \quad (3.1.7a)$$

$$\kappa^2 = n_2^2 K_0^2 - \beta^2 \quad (3.1.7b)$$

$A_e$  and  $A_o$  are arbitrary constants. Thus the solution to the wave equation for guided modes in a planar waveguide is, as would be expected, oscillatory in the guiding region and exponentially decaying outside of that region.

For the case of TM modes, the development is exactly the same as that performed for TE case but with different boundary continuity conditions at the interfaces. For simplicity, no more discussion of TM modes will be given here.

In order for the planar waveguide to guide light, the propagation constant must satisfy  $n_1K_0 < \beta < n_2K_0$ . If  $\beta = n_1K_0$ , for a particular wavelength, light will no longer be confined by the waveguide, but refract into the cladding layers. In this case, the waveguide cannot propagate light at this frequency. This is known as the 'cut-off' condition.

The analysis shows that larger refractive index differences and larger waveguide widths will support more modes. The lowest mode (zero order mode or fundamental mode) does not exhibit a *cut-off* as all the others do, which implies that light at any wavelength is guided in this mode no matter how small the refractive change, or guided layer thickness.

### **3.2 Characteristics of guided optical waves in rectangular waveguides**

In the analysis of a planar waveguide, it was assumed that the waveguide is infinite in the direction  $y$ , which means only one-dimensional optical confinement is obtained. Actually, the waveguides in many optoelectronic devices are two-dimensional which provide optical confinement in both the directions  $x$  and  $y$ .

The additional confinement can help to bring about desirable device characteristics. Using a rectangular waveguide geometry can, for example, bring low threshold currents to laser diodes, single-mode operation to OEIC/PIC interconnects or savings in drive power for electro-optic modulators, etc.

The basic rectangular waveguide structure consists of a waveguide region of index  $n_1$  surrounded on all sides by a confining medium of index  $n_2$  ( $n_1 > n_2$ ). Such waveguides are often called channel waveguides, stripe waveguides or 3-dimensional waveguides.

In reality, the more common situation is that the waveguide region is surrounded by different materials with different indices, all less than  $n_1$ , on different sides. It should be pointed out that, in such a case, the mode distributions would not be symmetric. The exact solution of the wave equation for this general case is extremely complicated.

**Effective index method (EIM).** For rectangular waveguides, a simple and effective method of solving the wave equation is the so-called the *effective index method* [2]. The effective index method is a relatively straightforward means of analysing a strip waveguide structure. Although the effective index method is less accurate than the most other numerical methods, this approach has been used since the beginnings of integrated optics, because of its immediate intuitive appeal.

A ridge waveguide structure (shown as Figure 3.2.1) can be divided into three regions labeled as 1, 2 and 3. Due to the fact that the central waveguide is thicker than the regions alongside, the effective index of central region is larger than that of the adjacent regions. By applying the slab waveguide theory to the three regions separately, we can obtain the effective indices  $n_{eff1}$ ,  $n_{eff2}$  and  $n_{eff3}$ , corresponding to the three regions respectively. Then the original 2-D problem is now simplified to a 1-D problem (also shown in Figure 3.2.1), which has been investigated before. For a TE wave, we model  $n_{eff1}$ ,  $n_{eff2}$  and  $n_{eff3}$  for TE polarisation first. Then the 1-D problem is solved in TM polarisation.

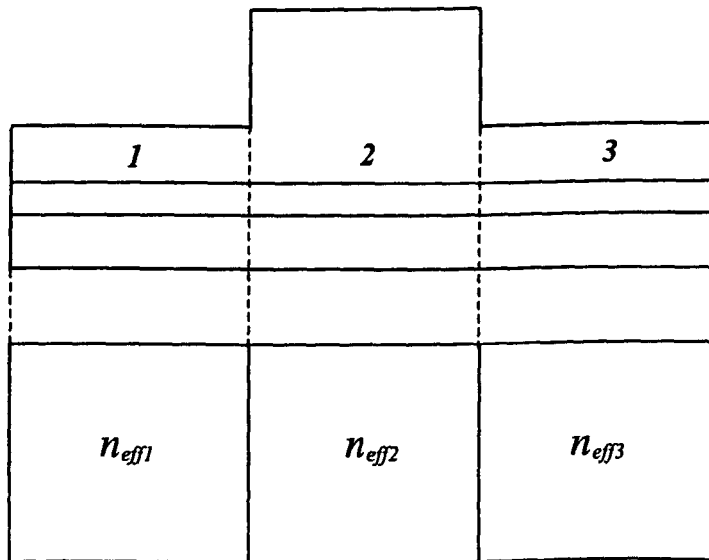


Figure 3.2.1 a ridge waveguide structure and its equivalent slab problem

**Numerical analysis.** For simplicity, Figure 3.1.1 shows abrupt transitions of refractive index. However, it should be noted that fabrication techniques such as diffusion may produce guide cross sections with graded-index profiles. In a channel guide the refractive index  $n$  is a function of both transverse coordinates.

As a result, the analysis of waveguide modes becomes a more complex task than for slab guides. In such cases, numerical analysis becomes a very useful tool. A variety of methods has been reported, such as the *beam propagation method* (BPM) [3-4], *finite element method* (FEM) [5-6] and *finite difference method* (FDM) [7]. Some of those will be applied in later analyses and designs.

### **3.3 Propagation loss in optical waveguide**

#### **3.3.1 Scattering loss**

There are two types of scattering losses in an optical waveguide: volume scattering and surface scattering.

Volume scattering is caused by the imperfections in the volume of the waveguide, such as voids, contaminant atoms and defects. The loss coefficient is proportional to the number of imperfections (scattering centers) per unit length and the relative size of the imperfections. In all but the crudest of waveguides, volume imperfections are so small compared to wavelength, and so few in number, that this mechanism is negligible compared to surface scattering loss.

Surface scattering loss can be significant even for relatively smooth surfaces, especially in the case of high-order modes because the propagating waves interact with the waveguide surface strongly.

Generally, an exponential intensity loss coefficient is used to describe the magnitude of optical loss. In this case, the intensity at any point along the length of the waveguide is given by:

$$I(z) = I_0 \exp(-\alpha z) \quad (3.3.1)$$

Where  $I_0$  is the initial intensity at  $z=0$ . It can be derived that the loss in  $dB/cm$  is related to  $\alpha$  by:

$$\alpha \text{ (dBcm}^{-1}\text{)} = 4.3 \alpha \text{ (cm}^{-1}\text{)} \quad (3.3.2)$$

An expression for the scattering loss coefficient  $\alpha_s$  due to surface roughness, is given by Tien [8],

$$\alpha_s = A^2 \left( \frac{1 \cos^3 \theta'_m}{2 \sin \theta'_m} \right) \left( \frac{1}{d + (1/p) + (1/q)} \right) \quad (3.3.3)$$

where  $\theta'_m$  is the incident angle of the light ray reflecting on the inner surface of the waveguide if a ray-optic description is used to describe the wave propagation in the waveguides;  $p$  and  $q$  are the extinction coefficients in the confining layers;  $A$  is a coefficient describing the surface roughness;  $d$  is the thickness of the waveguide layer.

It can be seen from (3.3.3) that the loss coefficient is proportional to the square of the waveguide surface roughness represented by  $A$ . It is also related to the

waveguide thickness plus the terms  $1/p$  and  $1/q$  which are related to the penetrating tails of the mode. Obviously, well-defined modes may be more affected by surface scattering than modes with large evanescent tails. If  $1/p$  and  $1/q$  are large compared with  $d$ , scattering will be reduced. Physically, the penetration of the wave at the interface makes it less sensitive to surface roughness. (3.3.3) also implies that higher-order modes (with small  $\theta_m$ ) have greater loss because they suffer more reflections at the surface per unit length in the direction of propagation.

A more sophisticated theory of surface scattering in slab waveguides has been developed by Marcuse as part of a larger effort to calculate total waveguide loss [9]. Marcuse's theory treats surface scattering as a form of radiation loss in which irregularities in the surfaces of the waveguide couple energy from propagating modes into radiation modes. With proper approximations, the results of Marcuse's theory correlate well with those predicted by (3.3.3).

Surface scattering is generally the dominant loss in dielectric film waveguides. For a typical surface variation of about  $0.1 \mu\text{m}$ , this mechanism contributes 0.5-5 dB/cm to the fundamental mode loss and more to that of the higher-order modes [10].

In semiconductor waveguides, there are two situations. For planar and shallow etched waveguides, the waveguide surfaces are the interfaces of epitaxial layers. With precisely controlled growth techniques, it is not difficult to limit the surface variation to  $\sim 0.01 \mu\text{m}$  and effectively eliminate surface scattering. For deep

etched waveguides, however, the sidewalls of the waveguides are quite rough because of the limited accuracy of lithography and dry etching. In this situation, surface scattering becomes an important factor in considering propagation loss.

### **3.3.2 Absorption loss**

Although absorption losses in amorphous thin films and crystalline ferro-electric material are generally negligibly small compared to surface scattering loss, significant absorption occurs in semiconductor material because of interband and free carrier absorption processes.

**Interband absorption.** Photons with an energy greater than the bandgap energy are strongly absorbed in a semiconductor by transferring the photon energy to electrons and exciting the electrons from the valence band to the conduction band. Generally, this effect is very strong, resulting in absorption coefficients larger than  $10^4 \text{ cm}^{-1}$  in direct bandgap semiconductors. To avoid interband absorption, the optical wavelength should be significantly longer than the absorption edge wavelength of the material.

In optoelectronic integration, interband absorption can be avoided by using some approaches, such as selective re-growth, selective area epitaxy and quantum well intermixing.

Regardless of which approach is used to avoid interband absorption in semiconductor optical waveguides, additional steps must be taken to eliminate free carrier absorption if practical waveguides are to be realised.

**Free carrier absorption.** When a photon transfers its energy to an electron in the conduction band or a hole in the valence band, exciting the carrier to a higher energy level within the same band, free carrier absorption (or intraband absorption) occurs.

The absorption coefficient  $\alpha_{fc}$  due to free carrier absorption can be derived from classical electromagnetic theory.

From the differential equation describing the motion of an electron in the presence of an applied field and the definition of dielectric constant, we can obtain [11]:

$$\alpha_{fc} = \frac{Ne^3 \lambda_0^2}{4\pi^2 n (m^*)^2 \mu \epsilon_0 c^3} \quad (3.3.4)$$

where  $N$  is the free carrier concentration,  $\lambda_0$  the wavelength,  $n$  the refractive index of the material,  $m^*$  the effective mass of electron,  $\mu$  the mobility,  $\epsilon_0$  the dielectric constant in vacuum and  $c$  the velocity of light in vacuum.

For the typical case of 1.55  $\mu\text{m}$  InP, with  $n=3.168$ ,  $m_e^*=0.08m_0$ ,  $m_h^*=0.6m_0$ ,  $\mu_e=5400 \text{ cm}^2/\text{V}\cdot\text{s}$ ,  $\mu_h=200 \text{ cm}^2/\text{V}\cdot\text{s}$ , (data quoted from the database of semiconductor material of Loffe Physico-Technical Institute, Russian Federation, <http://www.ioffe.rssi.ru/SVA/NSM/>), we can determine the absorption coefficient for both electrons and holes,  $(\alpha_{fc})_e$  and  $(\alpha_{fc})_h$ , in term of carrier concentration  $p$  and  $n$ ,

$$(\alpha_{fc})_e [cm^{-1}] = 1.148 \times 10^{-18} n \quad (3.3.5a)$$

$$(\alpha_{fc})_h [cm^{-1}] = 0.551 \times 10^{-18} p \quad (3.3.5b)$$

If the doping concentration is  $p=n=5 \times 10^{17} \text{ cm}^{-3}$ , then the estimated free carrier absorption losses are  $1.2 \text{ dB cm}^{-1}$  and  $2.5 \text{ dB cm}^{-1}$ , for the  $p$  and  $n$  doping layers respectively.

**Intervalence band absorption (IVBA).** Intervalence band absorption was first proposed by Adams et al in 1980 [12] as having a deleterious effect on long wavelength lasers, in particular their temperature performance.

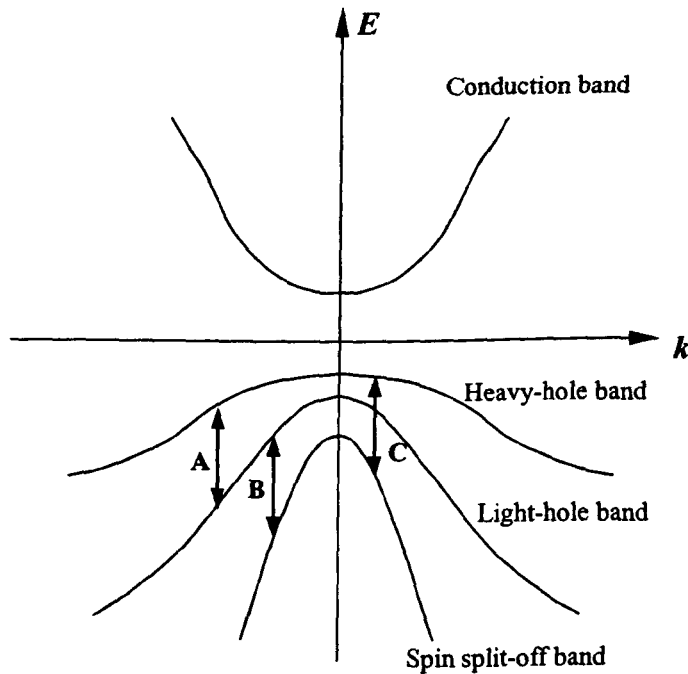


Fig 3.3.1 Three possible types of intervalence band absorption

The three possible types of vertical transition are illustrated in Figure 3.3.1. Among these three kinds of transitions, the light-heavy-hole band transition (A) is

not important as the transition energies are small for all heavy-hole states with a high probability of hole occupancy. The spin-split-off-light-hole band transition (B) is neglected on the basis of a low density of states in the light-hole band and a very low hole occupancy of final states for transitions at the band-gap energy. The larger density of states and hole occupancy in the heavy-hole band produce much greater absorption at relevant wavelengths for the spin split-off-heavy-hole band transition (C) than the other two transitions [13].

Childs and co-workers [13] calculated the IVBA coefficients of GaAs, InGaAs and InGaAsP for the hole concentration of  $1 \times 10^{18} \text{ cm}^{-3}$  at room temperature. They found the concentration dependence of the IVBA coefficients at a given energy are approximately linear for all the materials considered in the range  $p = 0.75\text{-}3 \times 10^{18} \text{ cm}^{-3}$ . This agrees well with Casey and Carter who found that, in p-type InP, IVBA varies with hole concentration  $p$  as  $\alpha(\text{cm}^{-1}) = 20 \times 10^{-18} p$  at the wavelength of  $1.5 \text{ }\mu\text{m}$  and  $\alpha(\text{cm}^{-1}) = 14 \times 10^{-18} p$  at  $1.3 \text{ }\mu\text{m}$  [14].

A further reassessment of IVBA in InGaAsP/InP carried out by Adams et al, based on the analytical results of Childs, showed that IVBA could account almost entirely for the temperature sensitivity of  $1.55 \text{ }\mu\text{m}$  active devices [15].

It has been shown that the application of strain results in a modification of the band shape. The in-plane mass of heavy holes is considerably reduced and consequently the transition probability for the IVBA process is also reduced, which leads to a significant decrease of the IVBA coefficient and even the complete 'switch-off' of IVBA [16-17].

Another affect of IVBA is related to the propagation loss of passive waveguides. From the numbers given by Casey, and Carter, we find that, for InP with doping concentration of  $5 \times 10^{17} \text{ cm}^{-3}$ , the estimated IVBA loss is about  $43 \text{ dB cm}^{-1}$ . Compared with the estimated free carrier absorption loss ( $2.5 \text{ dB cm}^{-1}$ ), we can conclude that this mechanism is a major factor in the propagation loss of passive waveguides, especially within P-doped upper cladding layers of  $1.55 \text{ }\mu\text{m}$  (and longer wavelength) material systems.

### 3.3.3 Radiation losses

The losses due to the waveguide structure itself arise mainly from power leakage and bending. Optical energy can be lost from the guided mode by radiation, in which case photons are emitted into the cladding areas and are no longer guided.

**Radiation loss from planar and straight channel waveguides.** For well-confined modes that are far from the *cut-off* condition, the radiation losses are generally negligible for both planar and channel waveguides. However, at *cut-off*, all of the energy is transferred into the radiation modes. Since the higher-order modes of a waveguide are either *cut-off* or closer to *cut-off* than low-order modes, radiation is greater for higher-order modes. In an ideal waveguide, there is no energy coupling from low-order modes to higher-order modes, as they are orthogonal. However in practical waveguides, energy coupling from low-order modes to higher-order modes takes place because of the irregularities and non-uniformities of the waveguides. That means even a well-confined mode may suffer energy loss through coupling to higher-order modes. This problem is not

encountered in typical waveguides of good quality, and radiation losses can generally be neglected compared to scattering and absorption losses. The one important exception is the case of curved channel waveguides.

**Radiation loss from curved channel waveguides.** When guided modes propagate through a curved channel waveguide, the optical field will be disturbed and the radiation loss may be increased greatly. This determines the so-called minimum allowable radius of curvature of a waveguide. As curved waveguides are necessary components of OEICs, radiation loss from curved waveguides is a compulsory consideration in design.

A convenient way of analyzing radiation loss is the velocity approach [18].

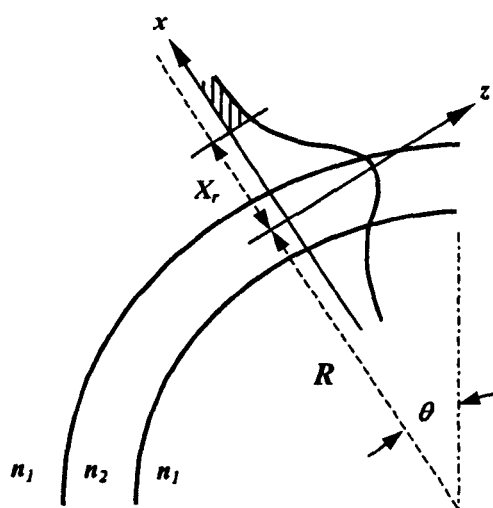


Fig.3.3.2 Diagram illustrating the velocity approach to the determination of radiation loss

The tangential phase velocity of waves in a curved waveguide must be proportional to the distance from the center of curvature because otherwise the phase front would not be preserved.

Consider a waveguide mode propagating in a circular bend of radius  $R$ , with propagation constant  $\beta_z$ , as shown in Fig. 3.3.2. There exists a radius  $R+X_r$ , beyond which the phase velocity would have to exceed the velocity of the unguided wave in order to preserve the phase front. Since the angular velocity  $d\theta/dt$  should be the same for all waves along the phase front, we obtain:

$$(R + X_r) \frac{d\theta}{dt} = \frac{\omega}{\beta_0} \quad (3.3.6)$$

$$R \frac{d\theta}{dt} = \frac{\omega}{\beta_z} \quad (3.3.7)$$

where  $\beta_0$  is the propagation constant of the unguided wave in the cladding material. Combining (3.3.6) and (3.3.7),

$$X_r = \frac{\beta_z - \beta_0}{\beta_0} R \quad (3.3.8)$$

The radiation process can be described as follows. Photons of the guided wave located at radii greater than  $R+X_r$  (the shadow area in Figure 3.3.2) cannot travel fast enough to keep up with the rest of the wave. They split away and are radiated into the cladding area so resulting in a radiation loss.

The loss coefficient related to the power lost per unit length of waveguide is defined as:

$$\alpha = \frac{1}{P(z)} \frac{dP(z)}{dz} \quad (3.3.9)$$

where  $P(z)$  is the power transmitted. If  $P_l$  is defined as the power lost by radiation within a length  $Z_c$  and  $P_0$  as the total power transmitted in the waveguide,  $\alpha$  can be expressed as:

$$\alpha = \frac{1}{P_0} \frac{P_l}{Z_c} \quad (3.3.10)$$

$Z_c$  is given by [19]:

$$Z_c = \frac{d}{\varphi} = \frac{d^2}{2\lambda_1} \quad (3.3.11)$$

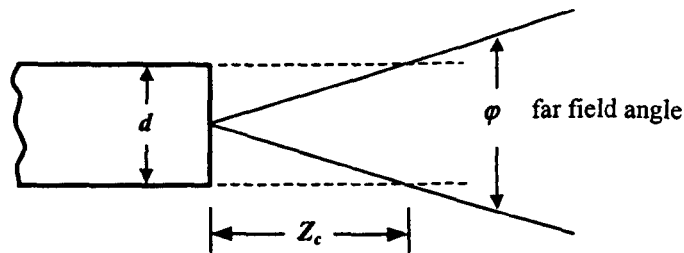


Fig.3.3.3 Light emission from a truncated waveguide

where  $d$  is the thickness of waveguide,  $\varphi$  the far field angle and  $\lambda_1$  the wavelength in the cladding material.

Given the field distribution, we can obtain a value of  $\alpha$  from:

$$\alpha = \frac{1}{Z_c} \frac{\int_{x_r}^{\infty} E^2(x) dx}{\int_{-\infty}^{\infty} E^2(x) dx} \quad (3.3.12)$$

The equation from (3.3.12) is quite complex. Normally, it has a simpler form:

$$\alpha = C_1 \exp(-C_2 R) \quad (3.3.13)$$

where  $C_1$  and  $C_2$  are constants that depend on the dimensions of the waveguide and the distribution of the optical mode. From (3.3.13), it should be noted that the radiation loss coefficient in curved waveguides depends exponentially on the curve radius.

### **3.4 Optical waveguide: design and characterisation**

#### **3.4.1 The material structure**

The material structure used in the design of optical waveguide is the same as that described in Chapter 2 (see Table 2.2.1), and was grown by molecular beam epitaxy (MBE) on a (100)-oriented n-type InP substrate.

It is necessary to obtain accurate values of the refractive indices of the layers to design the waveguide device. Here the first-order Sellmeier equation is used to calculate the refractive index of quaternary material AlInGaAs in the 1.55  $\mu\text{m}$  wavelength range:

$$n(\lambda)^2 = A + \frac{B\lambda^2}{\lambda^2 - C^2} \quad (3.4.1)$$

where the coefficients of A, B, C can be obtained from [20]. Table 3.4.1 shows the refractive indices of the layers in the wafer structure shown in Table 2.2.1. Here a precisely measured datum of InP is quoted from [21].

Table 3.4.1 Refractive indices of the materials

Material	Refractive Index
$\text{Ga}_{0.47}\text{In}_{0.53}\text{As}$	3.5741
$\text{In}_{0.52}\text{Al}_{0.48}\text{As}$	3.2004
$\text{Al}_{0.2}\text{In}_{0.525}\text{Ga}_{0.275}\text{As}$	3.3494
InP	3.1688

### 3.4.2 The design of optical waveguides

The basic requirements of the optical access waveguides are good mode confinement/distribution and low propagation loss. In addition, from the viewpoint of coupling between a monolithic device and optical fibres, the smaller the ellipticity of the mode transversal distribution, the better the coupling. (Here ellipticity is defined as the ratio of the beam waists in  $x$  and  $y$  directions,  $\omega_x/\omega_y$ ).

Numerical analysis of modes in the ridge-profiled access waveguides was carried out using the *finite difference method* (FDM). The FDM is based on the discretisation of Maxwell's equation with appropriate boundary conditions. The modal field solution is transformed into a matrix eigenvalue problem and solved by a standard numerical iterative procedure.

Here, the mode profile was calculated using FWAVE IV, written by Michael Taylor of this Department, a vector electromagnetic wave solving program used to solve field distributions in waveguides, couplers and arbitrarily defined structures.

Fig.3.4.1 shows the result of modeling for shallow-etched waveguides in InGaAs/InGaAlAs wafer B829. The ridge waveguide is 2  $\mu\text{m}$  wide and 0.8  $\mu\text{m}$  deep. A similar result for a deep-etched waveguide (2.4  $\mu\text{m}$  deep) is shown in Fig.3.4.2. Comparing Fig.3.4.1 and Fig.3.4.2, we can make some interesting deductions.

First, the deep-etched structure has a better mode distribution with the ellipticity of about 1.35, while that of the shallow-etched waveguide is about 4.7.

Furthermore, the field of the shallow-etched waveguide has a large extension in the direction parallel to the junction plane. If two such waveguides were located close together (i.e, a directional coupler), significant crosstalk would occur between them, which is fatal to the operation of an optical switch. That means that, if the shallow-etched waveguides are intended to be the access waveguides of the MMI coupler, the two waveguides should be sufficiently separated. This would increase the width of MMI section and hence its length (see Chapter 4). Obviously, this is undesirable.

Compared with shallow-etched waveguides, the major drawback of deep-etched waveguides is surface scattering from the sidewalls. As the waveguide width is reduced, the propagation loss caused by the surface scattering increases. There exists an optimal structure for the deep-etched waveguides that provides both good mode confinement and low propagation loss.

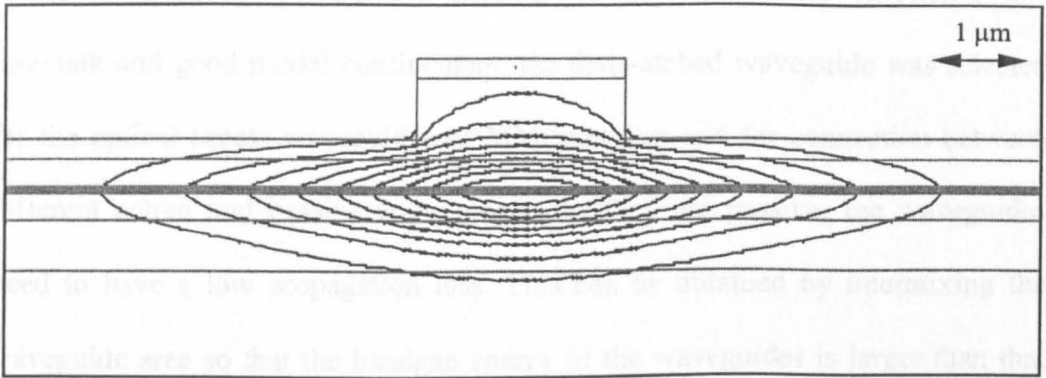


Fig.3.4.1 Simulated fundamental mode distribution in shallow-etched ridge waveguide of 2  $\mu\text{m}$  width

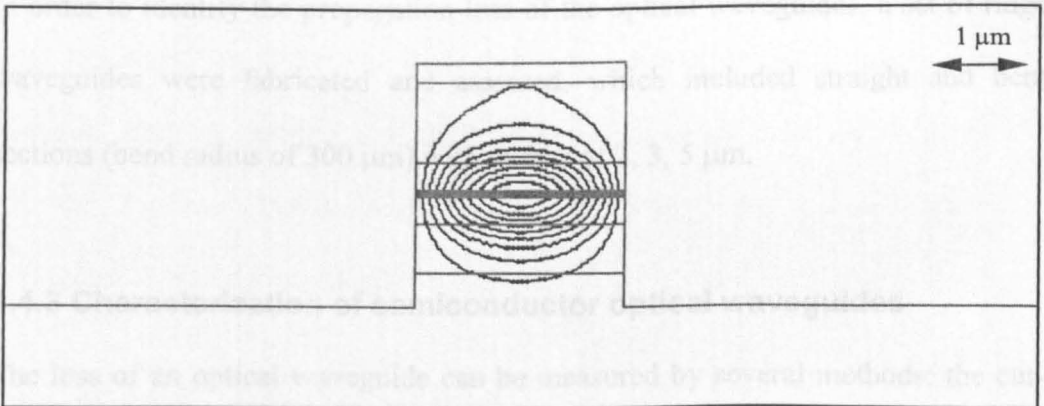


Fig.3.4.2 Simulated fundamental mode distribution in deep-etched ridge waveguide of 2  $\mu\text{m}$  width

In this project, considering the requirement of small mode ellipticity, low crosstalk and good modal confinement, the deep-etched waveguide was selected for the optical access waveguides of MMI couplers and for connection between different active and passive components. As they are passive, the waveguides need to have a low propagation loss. This can be obtained by intermixing the waveguide area so that the bandgap energy of the waveguides is larger than that of active components (see Chapter 5). Normally the required bandgap shift is larger than 100 nm.

In order to identify the propagation loss of the optical waveguides, a set of ridge waveguides were fabricated and assessed, which included straight and bent sections (bend radius of 300  $\mu\text{m}$ ) with widths of 2, 3, 5  $\mu\text{m}$ .

### **3.4.3 Characterization of semiconductor optical waveguides**

The loss of an optical waveguide can be measured by several methods: the cutback (two-point) method, the insertion loss method, the backscattering method and Fabry-Perot method.

As the Reference Test Method recommended by CCITT-G.652, the cutback method is the most widely used, and the most precise and accurate, but the major drawback is it is destructive. The output power through an optical waveguide  $P_{out}$  is first measured. The waveguide is then cut back to a certain length  $L$  from the optical source and the power  $P_{in}$  re-measured, without disturbing the launch condition. Finally, the propagation loss of the waveguide section can be obtained from:

$$\alpha = -10 \log \left( \frac{P_{out}}{P_{in}} \right) \quad (\text{dB}) \quad (3.4.1)$$

and the propagation loss of the waveguide per unit length,

$$\alpha = -\frac{10}{L} \log \left( \frac{P_{out}}{P_{in}} \right) \quad (\text{dB/mm}) \quad (3.4.2)$$

Normally, loss measurements of many kinds of optical waveguides, for example, the waveguides on semiconductor wafers and in bulk glass, cannot be carried out with the cutback method. This is mainly because the light launching system is separated from the sample, it is difficult to maintain the same launch condition after the 'cut-back'. For this reason, the insertion loss method is widely used in the loss measurement of optical waveguides.

The insertion loss method is recommended as the alternative to the cutback method by CCITT G.652. The insertion loss technique is similar to the cutback method. The output power through an optical waveguide is first measured. Then the loss of the waveguides can be obtained by considering the estimated coupling losses between the waveguide and launching system. This does avoid cutting the waveguides, but it introduces an uncertainty (sometimes very large) because the coupling losses can only be estimated. Particularly in the case of measurement of semiconductor optical waveguides, the coupling loss is very difficult to estimate with enough accuracy.

Figure 3.4.3 is a diagram of the experimental set-up for propagation loss measurement. The light from a 1.55  $\mu\text{m}$  tunable laser was coupled into waveguides via a standard 1.55  $\mu\text{m}$  single mode fibre. A polarization controller (PC) was employed to maintain TE mode input. On the tapered output end of the fibre, a micro-lens was formed using fibre splicer so that a relatively high coupling efficiency ( $\sim 4\text{-}5$  dB) could be achieved. The tunable laser was stabilized at 1 mW CW output power with 25% sinusoidal modulation. A 25 $\times$  objective lens was used to collimate the output beams from the waveguides. A Hamamatsu Photomultiplier Tube (PMT) camera was used for quick observation to find the output beams then it was replaced by a Ge photodetector. The signal was amplified by a lock-in amplifier.

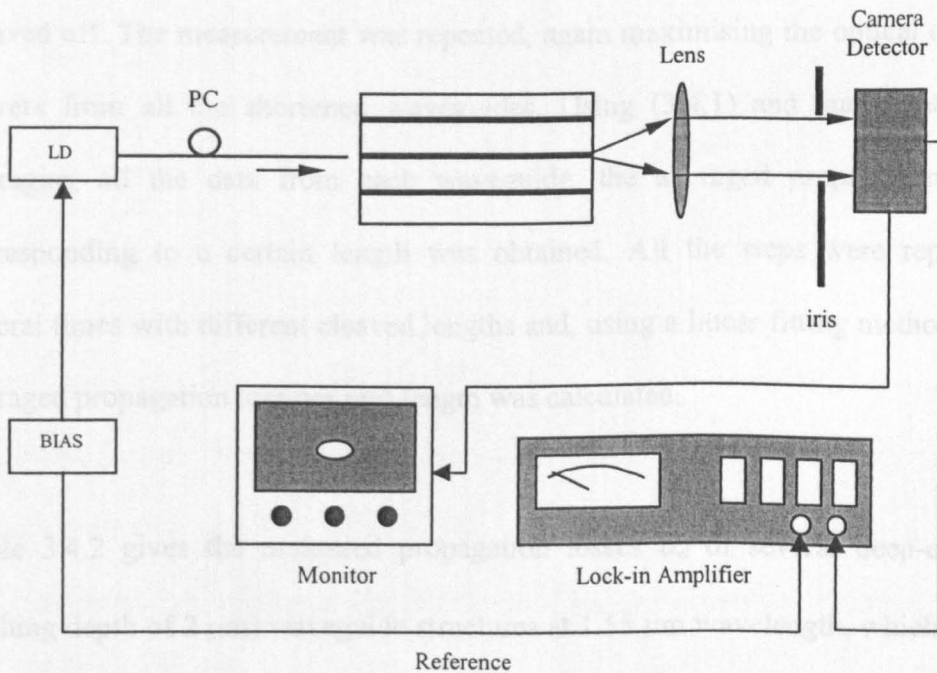


Fig.3.4.3 Set-up of loss measurement of passive waveguides

In our experiments, multiple measurements and mathematical averaging were employed to minimize the uncertainty introduced by changing the coupling condition.

In the fabrication stage, first quantum well intermixing was applied to the whole wafer to minimize the interband absorption. Then, several waveguides with nominally identical features were fabricated parallel to each other using photolithography and dry etching. In the measurement, the relative position of the fibre to the waveguide was carefully adjusted to obtain the maximum optical output power from the waveguide. Then the sample was moved laterally so that the second waveguide was aligned with the coupling system and the maximum output from this waveguide was obtained. After the output powers from all the waveguides were measured, a certain length of the sample (e.g., 1 mm) was cleaved off. The measurement was repeated, again maximising the optical output powers from all the shortened waveguides. Using (3.4.1) and mathematically averaging all the data from each waveguide, the averaged propagation loss corresponding to a certain length was obtained. All the steps were repeated several times with different cleaved lengths and, using a linear fitting method, the averaged propagation loss per unit length was calculated.

Table 3.4.2 gives the measured propagation losses  $\alpha_d$  of several deep-etched (etching depth of 2  $\mu\text{m}$ ) waveguide structures at 1.55  $\mu\text{m}$  wavelength, which were fabricated using photolithography. All the waveguides were made on InGaAs/AlInGaAs material (structure shown in Table 2.2.1). PL measurements showed that, at 77K, the peak wavelength of the intermixed wafer was around

1260 nm, far from that of as-grown wafers (~1420 nm) at same temperature. This indicates that interband absorption was negligible in our loss measurement.

For comparison, the measurement of propagation losses  $\alpha_s$  of 2  $\mu\text{m}$  wide straight/bend and 5  $\mu\text{m}$  wide, straight shallow-etched (etching depth of 0.8  $\mu\text{m}$ ) waveguide structures fabricated in the same way were also carried out and given in Table 3.4.2.

Table 3.4.2 Measured propagation loss of several waveguide structures

Waveguide Structure	$\alpha_d$ (dB/mm)	$\alpha_s$ (dB/mm)
	Deep-etched	Shallow-etched
2 $\mu\text{m}$ wide, straight	6.7	3.4
3 $\mu\text{m}$ wide, straight	4.5	
5 $\mu\text{m}$ wide, straight	3.2	2.5
2 $\mu\text{m}$ wide, bent, $R_{curve} = 300 \mu\text{m}$	11	$\infty^*$
3 $\mu\text{m}$ wide, bent, $R_{curve} = 300 \mu\text{m}$	8	

\*: very strong mode leakage

It can be seen that, for the deep-etched profile, narrower waveguides have higher propagation losses. It is believed that the difference comes from the scattering by the sidewall surface of the waveguides. All the waveguides tested here were fabricated using photolithography, which has a limited resolution of the order of  $10^{-1} - 10^{-2} \mu\text{m}$ . This leads to a quite rough sidewall surface after the dry etching process, as shown in Figure 3.4.4.

Simulation of the fundamental mode distributions in different waveguides shows that the narrower the waveguide, the closer the mode distribution is to the sidewall (See Figure 3.4.5). Consequently, sidewall surfaces with the same roughness cause significantly higher energy scattering from narrower waveguides. Of course, the roughness of the sidewall surface could be improved significantly by using expensive e-beam lithography combined with a complicated lift-off technique.

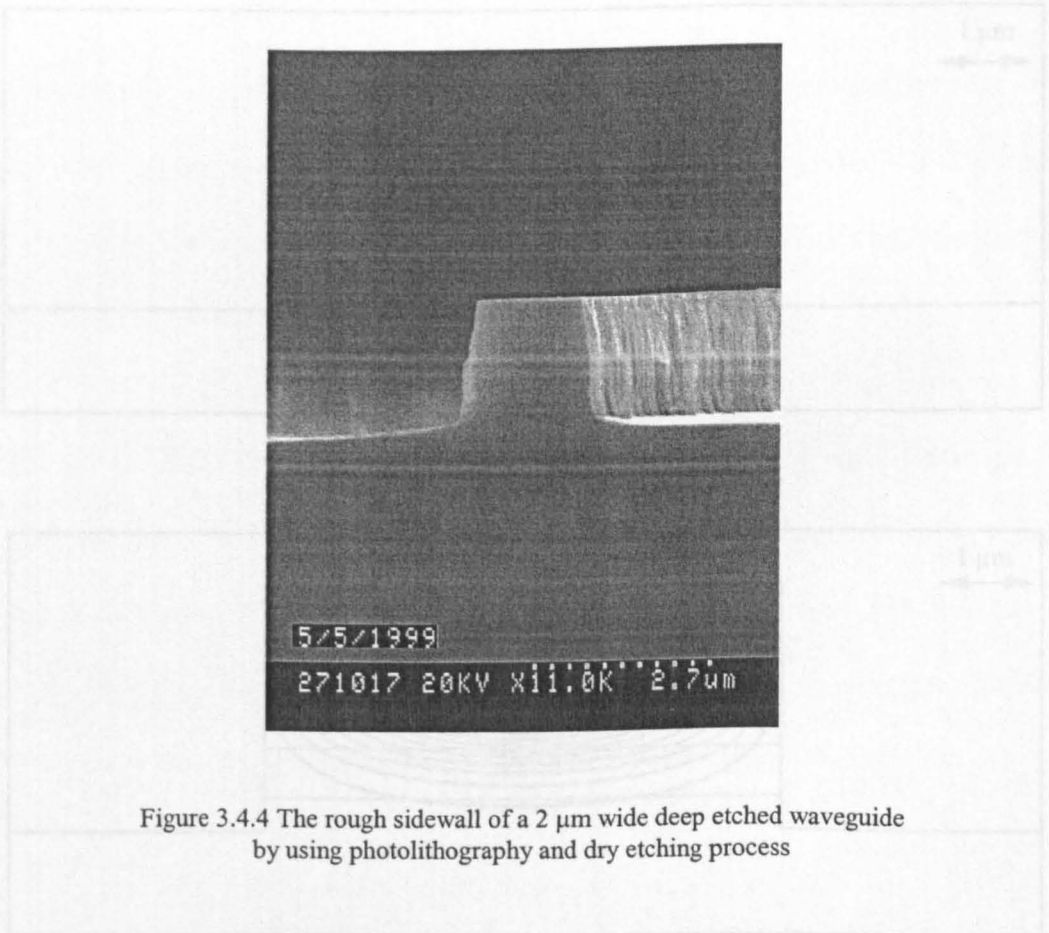
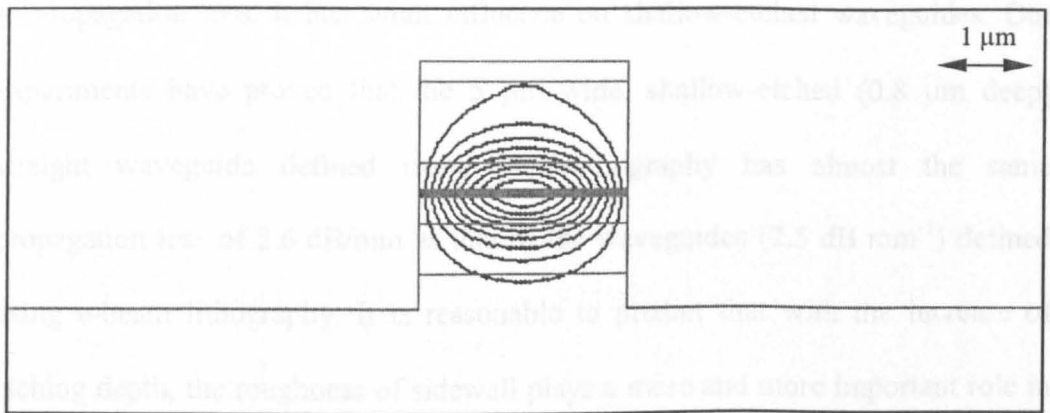
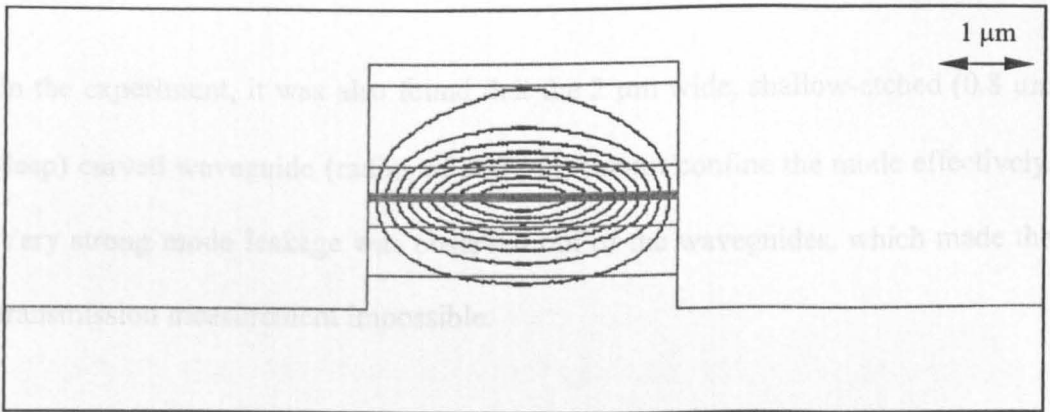


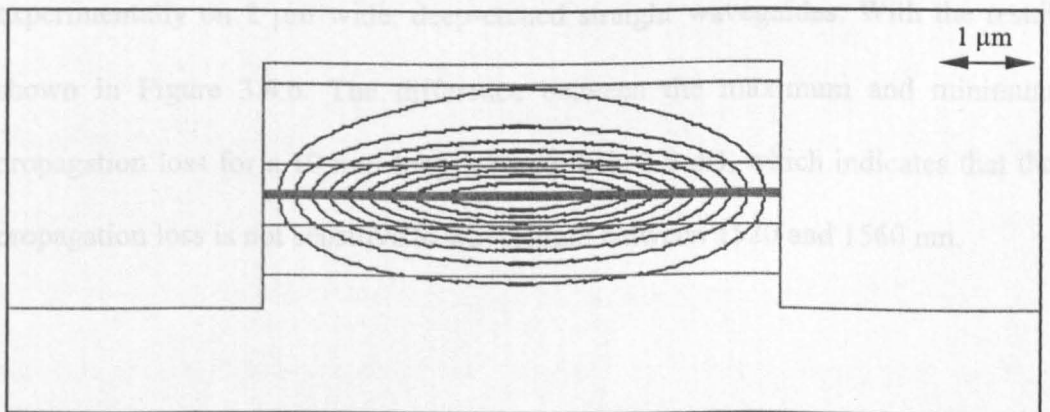
Figure 3.4.4 The rough sidewall of a 2 μm wide deep etched waveguide by using photolithography and dry etching process



(a) width of 2  $\mu\text{m}$



(b) width of 3  $\mu\text{m}$



(c) width of 5  $\mu\text{m}$

Fig.3.4.5 Simulated fundamental mode distributions in deep-etched ridge waveguides of 2, 3, 5  $\mu\text{m}$  width

Although the sidewall roughness of deep-etched waveguides contributes strongly to propagation loss, it has small influence on shallow-etched waveguides. Our experiments have proved that the 5  $\mu\text{m}$  wide, shallow-etched (0.8  $\mu\text{m}$  deep) straight waveguide defined using photolithography has almost the same propagation loss of 2.6 dB/mm as that of the waveguides (2.5 dB  $\text{mm}^{-1}$ ) defined using e-beam lithography. It is reasonable to predict that with the increase of etching depth, the roughness of sidewall plays a more and more important role in propagation loss of the waveguides.

In the experiment, it was also found that the 2  $\mu\text{m}$  wide, shallow-etched (0.8  $\mu\text{m}$  deep) curved waveguide (radius of 300  $\mu\text{m}$ ) cannot confine the mode effectively. Very strong mode leakage was observed out of the waveguides, which made the transmission measurement impossible.

The wavelength dependence of the propagation loss was also investigated experimentally on 2  $\mu\text{m}$  wide, deep-etched straight waveguides. With the result shown in Figure 3.4.6. The difference between the maximum and minimum propagation loss for a 10 mm long waveguide is 2.9 dB, which indicates that the propagation loss is not sensitive to wavelength between 1520 and 1560 nm.

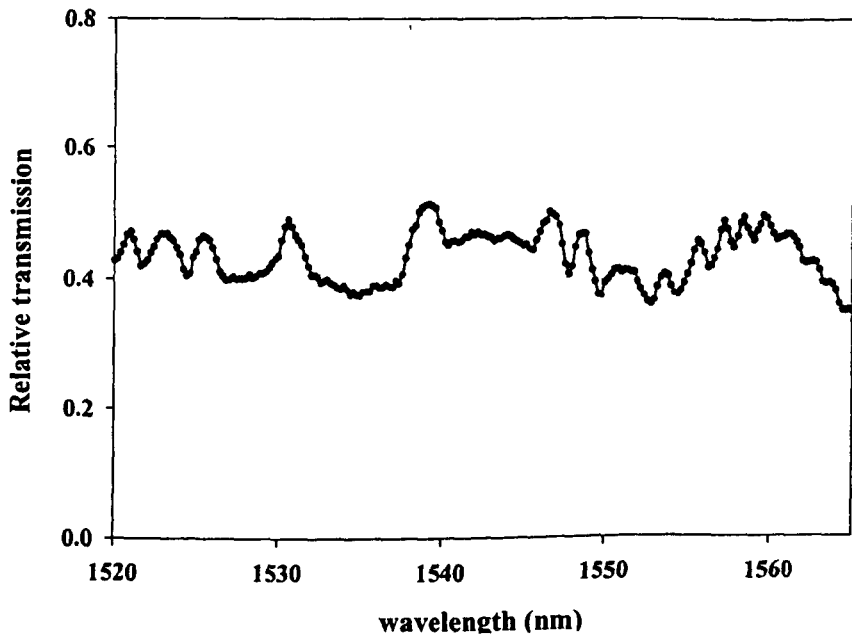


Fig. 3.4.6 Wavelength dependence of propagation loss

Although the 5  $\mu\text{m}$  wide deep-etched waveguide showed the lowest propagation loss in all the three deep-etched profiles, its major drawbacks limited its applications in our research project. First, with an ellipticity of about 2.5, the mode distribution is not good enough to satisfy the requirement of effective coupling between devices and single mode fibres. Moreover, if the 5  $\mu\text{m}$  wide deep-etched waveguides were used as the access waveguides of MMI couplers, the MMI section would be too long to be acceptable. For this reason, 2 and 3  $\mu\text{m}$  wide deep-etched waveguides were selected as passive waveguides in our research project.

### **3.5 Summary**

In this chapter, the basic theory of waveguides was reviewed. The simulation and design of several kinds of waveguides have been carried out. Theoretical and experimental results clearly show that narrow, deep etched waveguides can achieve a low ellipticity mode distribution, which is important for interconnection between semiconductor integrated devices and single mode fibres. However, the rough sidewall surface could result in a very high propagation loss due to surface scattering for some of the waveguides. By considering the mode distribution, propagation loss and design of MMI couplers, 2 and 3  $\mu\text{m}$  wide deep-etched waveguides were selected as the passive waveguides in our research project.

## REFERENCE

- [1] D. Marcuse, 'Light transmission optics', Van Nostrand, New York, pp.305, 1972
- [2] J. Buus, 'The effective index method and its application to semiconductor lasers', *IEEE J. of Quantum. Electronics*, Vol.QE18, No.7, pp.1083-1089, 1982
- [3] M. D. Feit, J.A. Fleck, 'Light propagation in graded-index optical fibre', *Applied Optics*, Vol.17, pp.3990-3997, 1978
- [4] C. W. Yeh, 'Optical waveguide theory', *IEEE Transaction of Circuit System*, Vol.CAS-26, pp.1011-1019, 1979
- [5] B. M. A. Rahman, F.A. Fernandez, and J.B. Davies, 'Review of finite-element methods for microwave and optical wave-guides', *Proceedings of IEEE*, Vol.79, pp.1442-1448, 1991
- [6] T. Yamamoto, M. Koshiya, 'Numerical-analysis of curvature loss in optical wave-guides by the finite-element method', *J. of Lightwave Technology*, Vol.11, pp.1579-1583, 1993
- [7] M. S. Stern, 'Semivectorial polarized finite-difference method for optical wave-guides with arbitrary index profiles', *Proceedings of IEE*, Vol.135, pp.56-63, 1988
- [8] P.K. Tien, 'Light waves in thin films and integrated optics', *Applied Optics*, Vol.10, pp.2395-2413, 1971
- [9] D. Marcuse, R.M. Derosier, 'Mode conversion caused by diameter changes of a round dielectric waveguide', *J. of Bell System Technology*, Vol.48, pp.3187-3233, 1969

- [10] D. D. North, 'Dielectric-waveguide-modal properties: a new analysis of the one-dimensional wave equation', *IEEE J. of Quantum Electronics*, Vol. **QE-15**, pp.17-26, 1979
- [11] A. Yariv, 'Introduction to Optical Electronics', 2<sup>nd</sup> edition, Holt Rinehart and Winston, New York, pp.100, 1976
- [12] A.R. Adams, M. Asada, Y. Suematsu, and S. Arai, 'The temperature dependence of the efficiency and threshold current of  $\text{In}_{1-x}\text{Ga}_x\text{As}_y\text{P}_{1-x}$  lasers related to intervalence band absorption', *Japanese J. of Applied Physics*, Vol. **19**, pp.L621-624, 1980
- [13] G.N. Childs, S. Brand, and R.A. Abram, 'Intervalence band absorption in semiconductor laser materials', *Semiconductor Science & Technology*, Vol. **1**, pp.116-120, 1986
- [14] H.C. Casey, and P.L. Carter, 'Variation of intervalence band absorption with hole concentration in p-type InP', *Applied Physics Letters*, Vol. **44**, pp.82-83, 1984
- [15] R. Adams, K.C. Heasman, and J Hilton, 'A reassessment of intervalence band absorption in 1.6  $\mu\text{m}$  (GaIn)(AsP)/InP', *Semiconductor Science & Technology*, Vol. **2**, pp761-764, 1987
- [16] I. Joindot, and J.L. Beylat, 'intervalence band absorption coefficient measurement in bulk layer, strained and unstrained multi quantum well 1.55  $\mu\text{m}$  semiconductor lasers', *Electronics Letters*, Vol. **29**, pp604-605, 1993
- [17] G. Fuchs, J. Horner, A. Hangleiter, V. Harle, F. Scholz, R.W. Glew, and L. Goldsten, 'Intervalence band absorption in strained and unstrained InGaAs multiple quantum-well structure', *Applied Physics Letters*, Vol. **60**, pp321-233, 1992

- [18] E.A.J. Marcatili, 'Bends in optical dielectric guides', *J. of Bell System Technology*, Vol.48, pp.2103-2132, 1969
- [19] S. E. Miller, *J. of Bell System Technology*, Vol.43, pp.1727, 1964
- [20] M.J. Mondry, 'Refractive indexes of (Al, Ga, In) As epilayers on InP for optoelectronic applications', *IEEE Photonics Technology Letters*, Vol.4, No.6, pp.627-630, 1992
- [21] G.D. Petti, 'Refractive index of InP', *J. of Applied Physics*, Vol.36, pp.2081-2083, 1965

## CHAPTER 4

# MULTIMODE INTERFEROMETER (MMI) COUPLERS: THEORY, DESIGN, FABRICATION AND CHARACTERISATION

Multi-mode interferometer (MMI) couplers are very important components in integrated opto-electronic devices due to their significant advantages compared to other kinds of couplers. In this chapter, the basic theory of the multi-mode interferometer (MMI) coupler is reviewed, and the design, fabrication and assessment of MMI couplers are presented. Important MMI coupler performance parameters such as the split ratio, the insertion loss of the MMI section and wavelength dependence are investigated.

## 4.1 Introduction

Today's telecommunication networks are increasingly focusing on flexibility and re-configurability, which require enhanced functionality of photonic integrated circuits (PICs). In addition, modern wavelength demultiplexing (WDM) systems will require signal routing and coupling devices to have large optical bandwidth and polarisation insensitivity, as well as small device dimensions and improved fabrication tolerances to reduce process costs and contribute to large-scale PIC production.

The optical coupler is such a kind of component. It is widely used in power dividers, modulators, switches, multiplexers/de-multiplexers and polarisation splitters. There are several types of couplers being used, such as directional couplers, two-mode interference (TMI) couplers and multimode interference (MMI) couplers.

The major drawback of directional couplers is their large size (typically several mm) which is due to their weak synchronous coupling effect. As a simpler alternative, TMI couplers consist of a two-mode central waveguide (TMI section) connected to two pairs of single mode input/output access waveguides. TMI couplers are shorter, more tolerant to fabrication precision and less polarisation dependent than directional couplers. But the requirement of high power coupling efficiency and proper excitation from the single mode input access waveguides to the TMI section limit the branching angle of the input access waveguides to very small values (typically  $< 2^\circ$ ) [1]. Due to the finite resolution of lithographic

processes, part of the area between the access waveguides cannot be well defined and fabricated. This leads the actual TMI section length to deviate from its design and causes uncertainty in the coupler operation. Moreover, extra mode coupling occurs due to the proximity of the access waveguides, increasing the performance uncertainty [2].

The self-imaging property of a multimode waveguide as result of the multimode interference (MMI) effect was first discussed as early as 1975 [3]. Because of their advantages over directional couplers and TMI couplers, MMI couplers have attracted much attention. Research has taken MMI couplers into practical use [4-6] and contributed much to the understanding of their operating principles and properties [7-8].

As the MMI section is wider than the equivalent TMI section, a good separation between the access waveguides is allowed, which eliminates the performance uncertainty due to the limited resolution of lithographic processes and unwanted coupling between the access waveguides. Furthermore, the high number of modes supported by the MMI section means high power coupling efficiencies. Consequently the excess losses of the MMI couplers are lower than those of TMI couplers. One of the MMI coupler's outstanding features is that the multiple access is permitted. The size of a multiple access MMI coupler is more compact than a group of directional couplers or TMI couplers performing the same function, making MMI couplers very suitable integrated multiplexing/demultiplexing devices.

## 4.2 Basic theory of MMI couplers

Self-imaging of periodic objects illuminated by coherent light was first described in 1836 by H. F. Talbot. Self-focusing (graded index) waveguides can also produce periodic real images of an object. However, the possibility of achieving self-imaging in uniform index slab waveguides was first suggested by Bryngdahl [9] and explained in more detail by Ulrich [3].

The principle can be stated as follows: self-imaging is a property of multimode waveguides by which an input field profile is reproduced in single or multiple images at periodic intervals along the propagation direction of the waveguide.

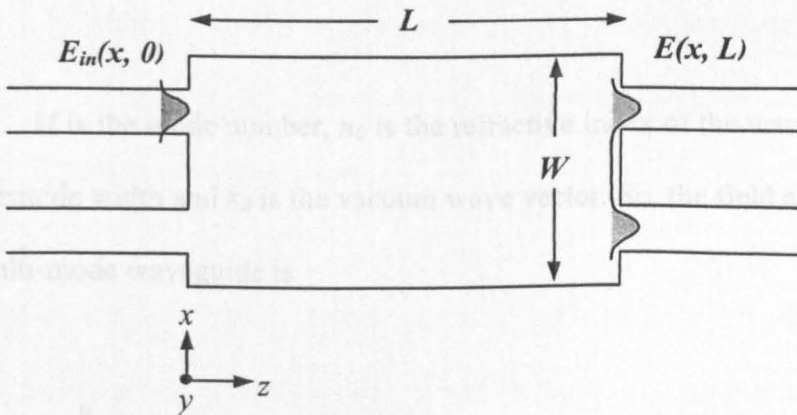


Fig.4.2.1 Schematic structure of a multimode interference (MMI) coupler

When a field  $E_{in}(x, 0)$  is launched into a multi-mode waveguide, it will excite all the eigenmodes  $E_k(x)$  of the waveguide.  $E_{in}(x, 0)$  can be expressed as a function of  $E_k(x)$  [10]:

$$E_{in}(x,0) = \sum_{k=0}^M a_k E_k(x) \quad (4.2.1)$$

$$a_k = \frac{\int E_{in}(x,0) E_k^*(x) dx}{\int E_k E_k^* dx} \quad (4.2.2)$$

The eigenmodes include two kinds of modes: propagating modes travelling along the waveguide with propagation constants  $\beta_k$  and radiative modes resulting in loss. In the step-index profile planar waveguide, the propagation constant  $\beta_k$  can be expressed as [11]:

$$\beta_k \cong k_0 n_0 - \frac{\pi^2 (k+1)^2}{2k_0 n_0 W^2} \quad (4.2.3)$$

$k = 0, 1, 2 \dots M$  is the mode number,  $n_0$  is the refractive index of the waveguide,  $W$  is the waveguide width and  $k_0$  is the vacuum wave vector. So, the field at a section  $z$  of the multi-mode waveguide is

$$E(x,z) = \sum_{k=0}^M a_k E_k(x) \exp(-j\beta_k z) \quad (4.2.4)$$

Defining  $L_\pi$  as the so-called beat length given by

$$L_\pi = \frac{2k_0 n_0 W^2}{3\pi} \quad (4.2.5)$$

and

$$\beta_k = k_0 n_0 - \frac{\pi(k+1)^2}{3L_\pi} \quad (4.2.6)$$

from (4.2.4) and (4.2.6), it can be seen that the field  $E(x, z)$  is a periodic function of  $z$  whose period is  $6L_\pi$ . The input field repeats itself every  $6L_\pi$  because of interference between the modes. Meanwhile, at a distance of  $6L_\pi/N$  from the entrance,  $N$  images of the input field are formed, laterally separated from each other by a distance  $W/N$  [12]. This forms the basis of the multimode interference (MMI) coupler. If the waveguide supports an appreciate number of propagating modes, so that the summed field  $\sum a_k E_k(x)$  resembles the input field  $E_{in}(x, 0)$  to a high fidelity, an effective energy coupling will occur between the input mode and the propagation modes, which leads to a low energy loss and back-reflection. This is important in practical device design.

It can be seen from (4.2.5) that a small change of width of the MMI section leads to a significant variation of MMI section length because  $L_\pi$  is proportional to  $W^2$ . This leads to two important conclusions. First, in the design of MMI couplers, narrow access waveguides are preferred so that a compact MMI structure can be achieved. Second, in the manufacture of MMI couplers, fabrication tolerances are tight as fabrication errors will seriously influence the performance of the MMI coupler, especially the splitting ratio, which is vital to the proper performance of integrated optical switches.

### **4.3 Modeling and design of MMI couplers**

The material used in the design and fabrication of MMI couplers was the InGaAs/AlInGaAs, the structure, previously described in table 3.4.1.

Normally, there are two important aspects in the design of MMI couplers: the designs of the access waveguides and the MMI section. In Chapter 3, the design and characterisation of optical access waveguides was described. As we have already known, shallow-etched waveguides has several drawbacks when employed as access waveguides of the MMI couplers. The large ellipticity is negative to the coupling between single mode fibre and device. Large extension in the direction parallel to the junction plane means that large separation between the access waveguides has to be adapted to avoid the crosstalk. Obviously, this would cost us large MMI sizes, which is undesirable. For these reasons, in this project, deep-etched waveguides were selected as the access waveguides of the MMI couplers.

We are interested in the MMI coupler specification required by integrated optical switches such as demultiplexers. The basic requirements such MMI couplers must meet are:

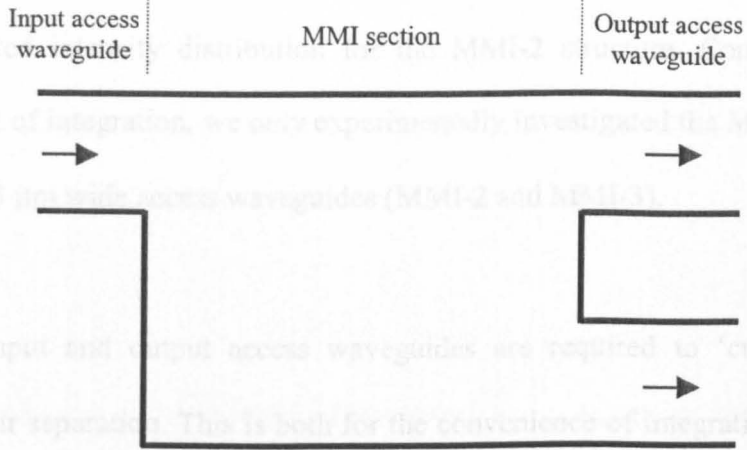
1. A 50:50 split ratio
2. Negligible cross-talk. This can be achieved by using a deep-etched profile and ensuring there is sufficient separation between access waveguides.
3. Compact structure. This is achieved by using narrow access waveguides.

The design of the MMI section was carried out using the beam propagation method (BPM). The beam propagation method (BPM) is based on the BPM equation, which links the electromagnetic fields in two axially separated parallel planes. The electrical magnetic field in a particular plane is calculated numerically from its distribution in the previous plane using the BPM equation. This process is then repeated to give a complete simulation of wave propagation on a step by step basis with an arbitrary excitation boundary condition. The BPM equations inherently take both guided and radiation modes into account. They also allow axial index variations. Because of these two important features, the BPM has become one of the most useful numerical tools for studying optoelectronic waveguide devices.

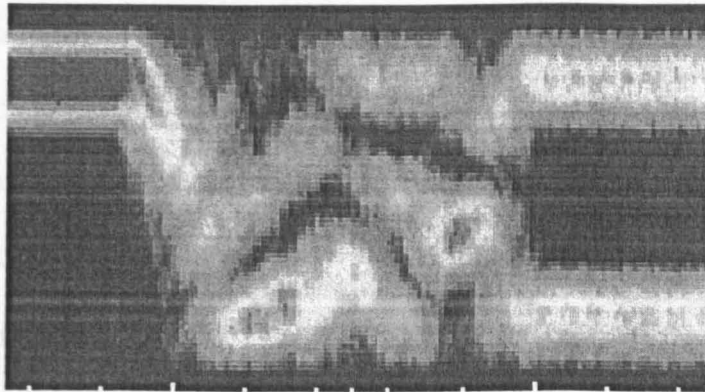
The MMI coupler was simulated and designed using 'BPM\_CAD', from OPTIWAVE Corporation Ltd., a powerful, user-friendly application that allows computer-aided design of a wide variety of integrated optical waveguides. This software package uses the BPM to analyse and simulate mode propagation in the waveguides. From a knowledge of the input parameters, BPM\_CAD can be used to determine the optimum structure of MMI couplers. Three different MMI coupler geometries were designed, with the dimensions given in Table 3.4.1.

Table 3.4.1 Structure parameters of designed MMI couplers

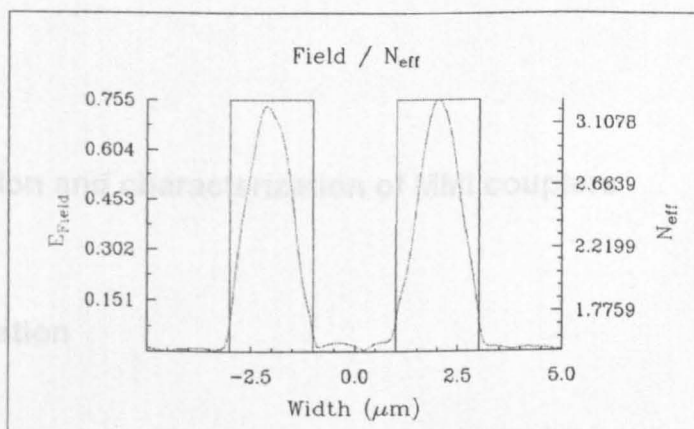
Structure parameters of the MMI couplers	MMI-2	MMI-3	MMI-5
Width of access waveguide ( $\mu\text{m}$ )	2	3	5
Separation of access waveguides ( $\mu\text{m}$ )	2	3	5
Split ratio	50:50	50:50	50:50
Width of MMI section ( $\mu\text{m}$ )	6	9	15
Length of MMI section ( $\mu\text{m}$ )	160	360	980



(a) Design of the MMI coupler



(b) Optical field distribution in the MMI coupler



(c) Field distribution and  $N_{eff}$  in output waveguides of the MMI coupler

Fig.4.3.1 Simulated mode distributions in the MMI section

From Table 4.3.1, we can get a clear impression of the relationship between the width and length of the MMI couplers as predicted by (4.2.5). Figure 4.3.1 shows the calculated intensity distribution for the MMI-2 structure. Considering the requirement of integration, we only experimentally investigated the MMI couplers with 2 and 3  $\mu\text{m}$  wide access waveguides (MMI-2 and MMI-3).

Both the input and output access waveguides are required to ‘curve out’ to increase their separation. This is both for the convenience of integration (e.g. 2×2 crosspoint switch and demultiplexers) and to eliminate coupling and interference between the access waveguides. Furthermore, a larger separation between the access waveguides is an advantage for the optical coupling between access waveguides and fibres. A previously reported simulation suggested that a curvature radius of 200  $\mu\text{m}$  for a circular waveguide should be acceptable in terms of propagation loss [13]. In our design, a series of several 300  $\mu\text{m}$  radius bends was employed to give a sufficient distance (0.25~1 mm) between the access waveguides as well as a relatively compact structure.

## **4.4 Fabrication and characterization of MMI couplers**

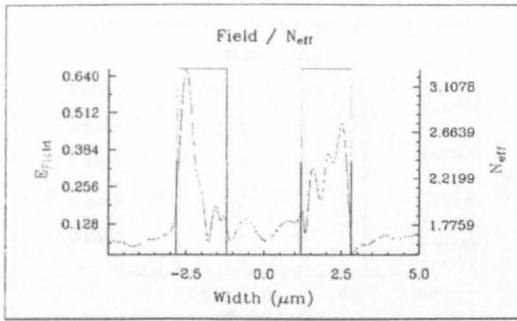
### **4.4.1 Fabrication**

As we know, the limited accuracy of photolithography used in the fabrication of MMI couplers will influence the final performance. Fig.4.4.1 shows the simulated output field distribution of a 160  $\mu\text{m}$  long MMI section with widths in the range

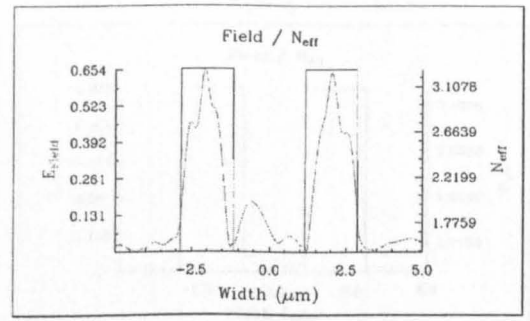
of 5.6-6.1  $\mu\text{m}$ . It is clear that the splitting ratio and mode distribution are very sensitive to the width of MMI section. This can be explained from (4.2.5). The estimated 1 dB tolerance of the MMI section width is only about  $\pm 0.2 \mu\text{m}$  [14]. In contrast, the operation of the MMI coupler is not sensitive to variations of the MMI section length (See Fig.4.4.2).

Apart from the photolithographical accuracy, further fabrication error comes from the dry etch process. It was found that dry etched waveguide were likely to have a smaller width than the intended design. Sometimes over-etching of both the mask and the substrate resulted in misshapen MMI profiles. Considerable attentions should therefore be paid to the fabrication process.

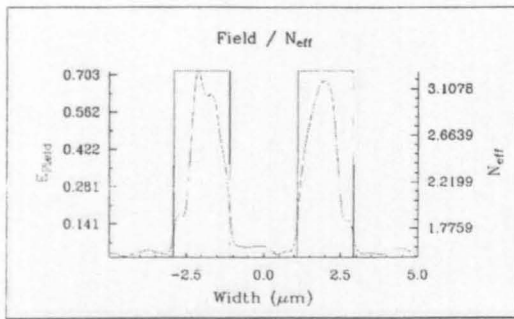
As described previously, the MMI couplers were fabricated in InGaAs/AlInGaAs material. The whole device structure was intermixed using the method of sputtering process induced disordering (See Chapter 5) so that a low transmission loss could be obtained. To obtain the required fabrication accuracy, a combined Ti/SiO<sub>2</sub> mask system was employed to transfer the patterns from the photolithographic mask. Fig.4.4.3 shows SEM micrographs of an MMI coupler.



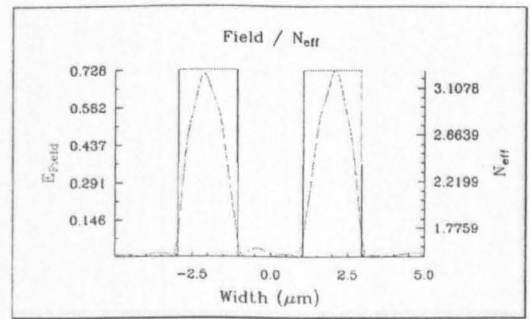
(a)  $W = 5.6 \mu\text{m}$



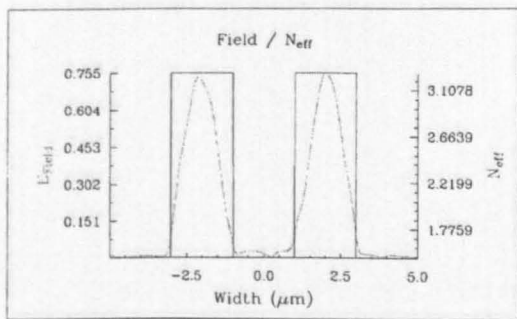
(b)  $W = 5.7 \mu\text{m}$



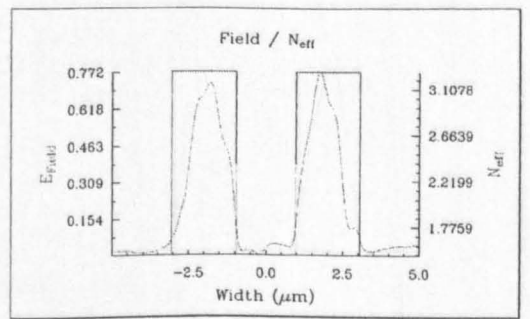
(c)  $W = 5.8 \mu\text{m}$



(d)  $W = 5.9 \mu\text{m}$

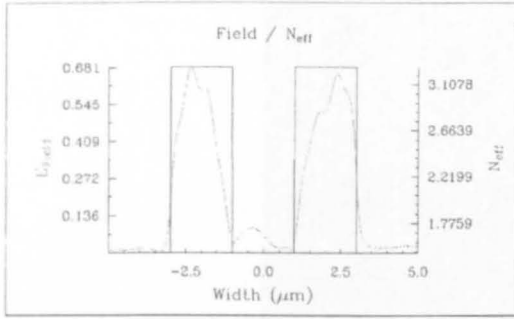


(e)  $W = 6.0 \mu\text{m}$

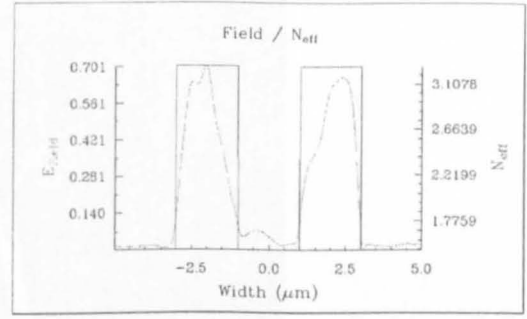


(f)  $W = 6.1 \mu\text{m}$

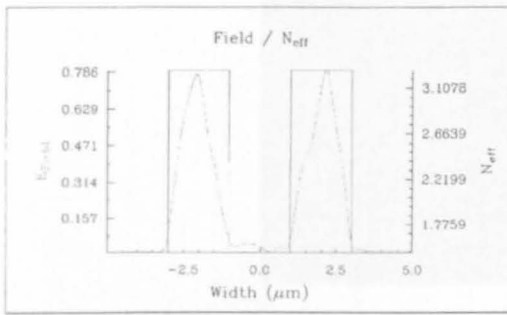
Fig.4.4.1 Simulated output field distribution of a  $160 \mu\text{m}$  long MMI with different widths by using BPM CAD



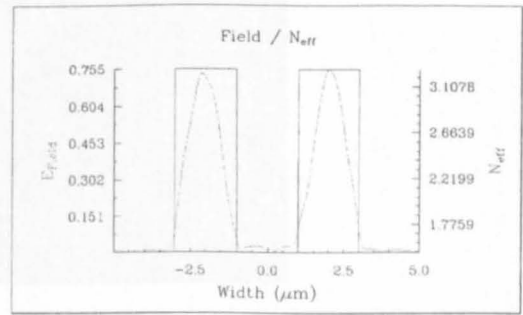
(a)  $L = 154 \mu\text{m}$



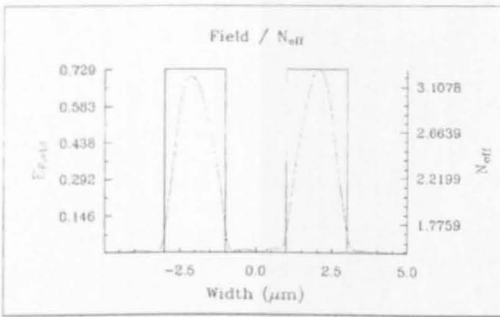
(b)  $L = 156 \mu\text{m}$



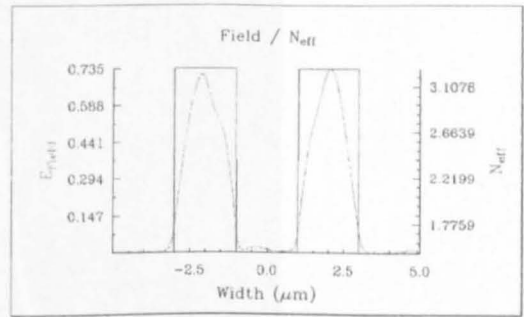
(c)  $L = 158 \mu\text{m}$



(d)  $L = 160 \mu\text{m}$



(e)  $L = 162 \mu\text{m}$



(f)  $L = 162 \mu\text{m}$

Fig.4.4.2 Simulated output field distribution of a  $6 \mu\text{m}$  wide MMI with different lengths  $L$  by using BPM CAD

4.4.2 Characteristics of MMI coupler

Figure 4.4.3

Fig. 4.4.3

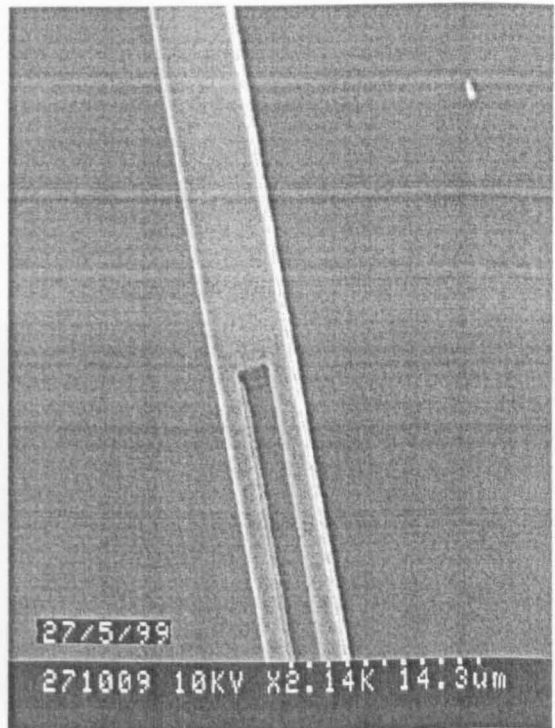
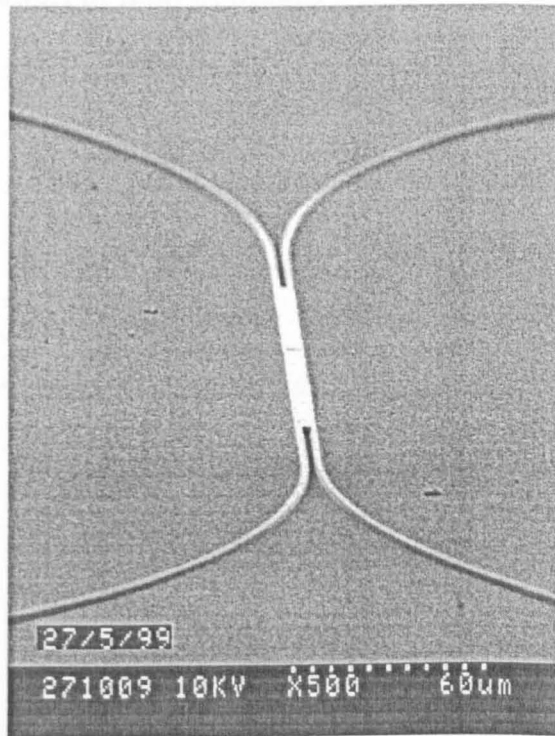


Fig.4.4.3 Profiles of the MMI coupler

#### 4.4.2 Characterization of MMI couplers

The performance of MMI couplers was assessed using the basic test bed shown in Fig.4.4.4.

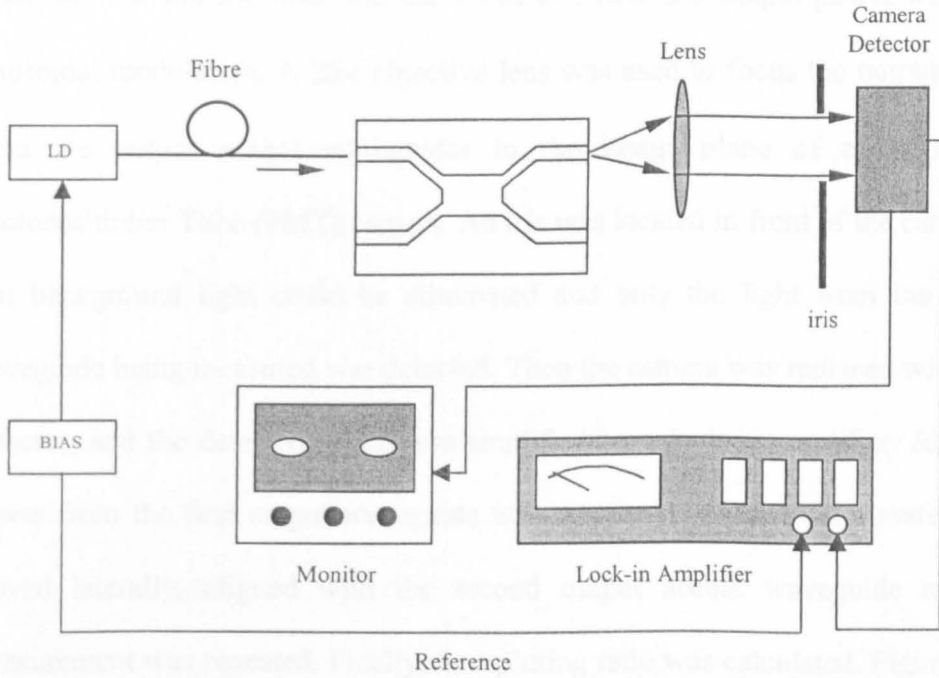


Fig.4.4.4 Set-up of loss measurement of passive waveguides

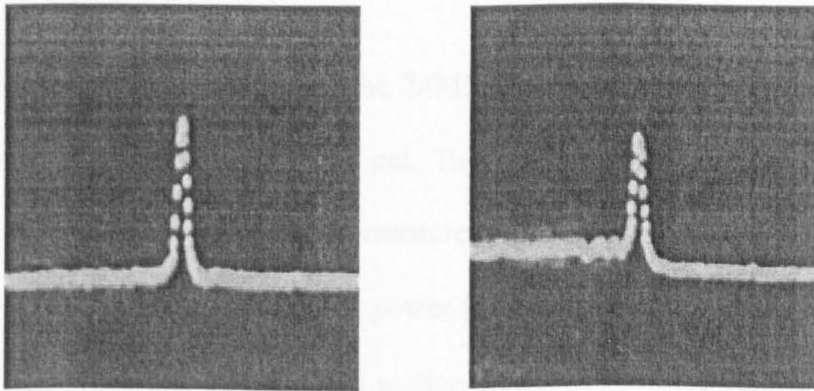


Fig.4.4.5 Photographs of optical output distributions from the two output access waveguides of a MMI coupler

To measure the splitting ratio, the light from a 1.55  $\mu\text{m}$  tunable laser was coupled into one of the input access waveguides via a standard 1.55  $\mu\text{m}$  single mode fibre. On the output tapered end of the fibre, a micro-lens was formed using a BFS-60 portable fibre fusion splicer so that relatively low coupling loss (~4-5 dB) could be achieved. The tunable laser was stabilized at 1 mW DC output power with 25% sinusoidal modulation. A 25 $\times$  objective lens was used to focus the output beams from the output access waveguides to the image plane of a Hamamatsu Photomultiplier Tube (PMT) camera. An iris was located in front of the camera so that background light could be eliminated and only the light from the output waveguide being measured was detected. Then the camera was replaced with a Ge detector, and the detected signal was amplified by a lock-in amplifier. After the power from the first output waveguide was measured, the detecting system was moved laterally, aligned with the second output access waveguide and the measurement was repeated. Finally, the splitting ratio was calculated. Figure 4.4.5 shows photographs of the optical distributions from the two output waveguides of a MMI coupler.

To measure the insertion loss of the MMI section, a similar method to that introduced in Chapter 3 was carried out. The maximum optical power launched from the end of MMI section was measured first. Then the MMI section was cleaved off and the maximum optical power from the input access waveguide was measured. The insertion loss of MMI section was then obtained using (3.4.1). To improve the accuracy, the measurement was repeated on several MMI couplers fabricated on the same wafer. Finally the insertion loss data were mathematically averaged.

Table 4.4.1 gives the measured parameters of two kinds of MMI couplers.

Table 4.4.1 Characterization of MMI sections

	MMI-2	MMI-3
Splitting ratio of MMI coupler	46:54	51:49
Insertion loss of MMI section (dB)	1.95±0.32	2.70±0.30

The wavelength dependence of the MMI splitting ratio was found by repeating the measurement described above, while changing the laser wavelength. Fig.4.4.6 shows both the simulated and experimental wavelength dependence of the splitting ratio. It is clear that this ratio is not sensitive to wavelength in the range 1530-1570 nm.

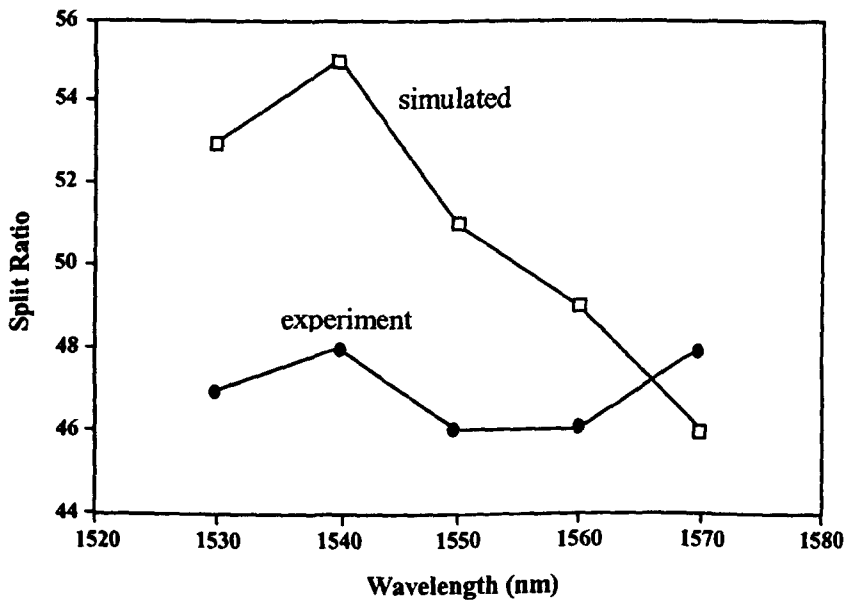


Fig.4.4.5 Wavelength dependence of split ratio of the MMI coupler

## **4.5 Summary**

The basic theory of multimode interference (MMI) coupler has been reviewed, and the design of 50:50 MMI couplers has been described. Two kinds of MMI couplers have been fabricated and characterized. The experimental results show good agreement with design and simulations.

## Reference

- [1] C. Caldera, N. Caponio, C. DeBernardi, F. Delpiano, G. Destefanis, and M. Billard, '3-dB couplers integrated in InGaAlAs/InP for coherent applications', *Proceeding of ECOC'90 (Amsterdam)*, pp.357-360, 1990
- [2] S. Gevorgyan, et al, 'Coupling among waveguides of small spacing,' *Electronics Letter*, Vol.24, No.1, pp.814-815, 1988
- [3] R. Ulrich, 'Image formation by phase coincidences in optical waveguides', *Optics Communications*, Vol.13, No.3, pp.259-264, 1975
- [4] E.C.M. Pennings, R.J. Deri, A. Scherer, R. Bhat, T.R. Hayes, N.C. Andreadakis, M.K. Smit, L.B. Soldano, and R.J. Hawkins, 'Ultra-compact, low-loss directional-couplers on InP based on self-imaging by multimode interference', *Applied Physics Letters*, Vol.59, No.16, pp.1926-1928, 1991
- [5] L.B. Soldano, F.B. Veerman, M.K. Smit, B.H. Verbeek, A.H. Dubost, and E.C.M. Pennings, 'Planar monomode optical couplers based on multimode interference effects', *J. of Lightwave Technology*, Vol.10, No.12, pp.1843-1850, 1992
- [6] L.B. Soldano, and E.C.M. Pennings, 'Optical multimode interference device based on self-imaging: principles and applications', *J. of Lightwave Technology*, Vol.13, No.4, pp.615-627, 1995
- [7] M. Bachmann, P.A. Besse, and H. Melchior, 'General self-imaging properties in N×M multimode interference couplers including phase-relations', *Applied Optics*, Vol.33, No.18, pp.3905-3911, 1994

- [8] M. Bachmann, P.A. Besse, and H. Melchior, 'Overlapping-image multimode interference couplers with a reduced number of self-images for uniform and non-uniform power splitting', *Applied Optics*, Vol.34, No.30, pp6898-6910, 1995
- [9] O. Bryngdahl, 'Image formation using self-imaging techniques', *J. of Optics Society of America*, Vol.63, No.4, pp.416-418, 1973
- [10] A.W. Snyder, 'Optical waveguide theory', Chapman and Hall, 1983
- [11] L.B. Soldano, F.B. Veerman, M.K. Smit, B.H.Verbeek, A.H. Dubost, and E.C.M. Pennings, 'Planar monomode optical couplers based on multimode interference effects', *J. of Lightwave Technology*, Vol.12, pp.1843-1850, 1992.
- [12] J.M. Heaton, et al, 'Novel 1-to N way integrated optical beam splitters using symmetric mode mixing in GaAs/AlGaAs multimode waveguides', *Applied Physics Letter*, Vol.61, pp.1754-1756, 1992
- [13] T. Yamamoto, and M. Koshiha, 'Numerical analysis of curvature loss in optical waveguides by the finite-element method', *J. of Lightwave Technology*, Vol.11, pp.1579-1583, 1993
- [14] S. Yu, 'Semiconductor ring lasers for high speed communications', PhD thesis. University of Glasgow, 1997

## CHAPTER 5

### QUANTUM WELL INTERMIXING

In this chapter, several techniques of quantum well intermixing are briefly introduced. Then a novel intermixing technique, sputtering process induced disordering (SID), is described and experimentally investigated. SIMS analysis showed that during the SID process, Cu was involved and played an important role in QWI.

## 5.1 The development of quantum well intermixing

With the increasing demand for extremely high data transmission in optical communication systems, there has been considerable interest in monolithic integration of light sources, modulators and switching devices. When considering the integration of several kinds of devices on a semiconductor substrate, it is important that each device is fabricated within semiconductor material with the appropriate bandgap energy. To realise this, selective control is required spatially over the local optical and electrical characteristics of the multiple quantum well (MQW) material. Many techniques, such as selective regrowth and selective area epitaxy, have been reported. Although it appears promising, selective regrowth requires expensive facilities such as metal organic vapor phase epitaxy (MOVPE) during the whole production process [1], and yields tend to be low. Selective area epitaxy, using silica masks, enables regions with different bandgaps to be realised across a wafer in a single growth step, but such an approach does not allow complete control of the bandgap in two dimensions [2].

As an alternative, quantum well intermixing (QWI) has been developed. Quantum well intermixing is a disturbance to the lattice of the semiconductor crystal caused by introducing either impurities, interstitial native elements, vacancies or a combination of them. Such disturbances may change the energy band structure and bandgap energy of the semiconductor by modifying the quantum well profile. This is because diffusion of the point defects intermixes the previously well-defined interface between wells and barriers, so inducing a change in the effective

bandgap [3]. The first report of an intermixing technique, performed on GaAlAs/GaAs structures, was by W.D. Laidig, et al [4].

Since then, a number of QWI techniques have been developed. These include impurity induced disordering (IID), impurity free vacancy disordering (IFVD), ion implantation induced disordering, and several laser induced disordering techniques such as photo-absorption induced disordering (PAID) and Pulsed PAID. When intermixing techniques are applied in photonic integration, three parameters are especially important: the absorption coefficient, the material resistivity and the refractive index change induced by intermixing. An ideal loss target within a photonic integrated circuit (PIC) is  $<1 \text{ dB cm}^{-1}$  but  $10 \text{ dB cm}^{-1}$  would be acceptable in many applications, and values as high as  $220 \text{ dB cm}^{-1}$  in a DBR grating will still give sufficient fineness for single mode operation [3]. A further requirement is that the electrical resistance of waveguides should be sufficiently high to isolate individual components, and studies of an integrated laser/modulator structure have demonstrated that the required isolation resistance between the laser and the modulator might need to be as large as  $100 \text{ k}\Omega$  [5].

### **5.1.1 Impurity induced disordering (IID)**

In IID processes, an electronically active impurity is introduced into an epitaxial wafer using surface dopant diffusion or ion implantation [4]. The presence of such impurities alters the Fermi level so changing the equilibrium concentration of certain point defects, resulting in an increased rate of atomic interdiffusion during a subsequent anneal stage. The technique has been applied to different MQW systems such as GaAs/AlGaAs, InGaAs/InGaAsP and InGaAs/AlInGaAs.

Current understanding of the IID process suggests that the role of impurities is to induce the disordering process through the generation of free carriers that increase the equilibrium number of vacancies or interstitials at the annealing temperature [6].

A number of species have been demonstrated to disorder the GaAs/AlGaAs system, the most important of which are Zn (p-type) and Si (n-type). Impurities need to be present in concentrations greater than around  $10^{18} \text{ cm}^{-3}$  in order to enhance the interdiffusion rates of the lattice elements significantly. This consideration leads to serious problems when electrically active dopants are used as intermixing species: high free carrier/intervalence band absorption and low material resistivity. The most commonly reported impurity for IID is Si and the typical absorption coefficients are above  $43 \text{ dB cm}^{-1}$  ( $10 \text{ cm}^{-1}$ ), which is a consequence of free carrier absorption. Furthermore, for waveguide dimensions of  $3 \mu\text{m} \times 1 \mu\text{m} \times 0.5 \text{ mm}$  long, a carrier density below  $10^{17} \text{ cm}^{-3}$  is necessary to provide electrical isolation  $\sim 100 \text{ k}\Omega$ . It appears that Si (or Zn) IID is unlikely to give required performance. As a consequence, some electrically neutral dopants F and B have been used as implantation species to circumvent the large optical propagation losses associated with IID techniques [7].

However, neutral impurities still introduce substantial changes in the material resistivity and trap concentration and the residual damage associated with implantation.

### 5.1.2 Impurity free vacancy disordering (IFVD)

IFVD can yield large bandgap energy shifts without many of the disadvantages of IID. In IFVD of the GaAlAs/GaAs system, a high-temperature anneal induces the out-diffusion of Ga from the epilayer cap into a suitable dielectric cap and results in an increase in Ga vacancies close to the wafer surface. During the anneal stage, the vacancies thermally diffuse into the QW region and promote the interdiffusion of Ga-Al in the wells and barriers [8].

While certain dielectric caps (e.g., SiO<sub>2</sub>) enhance out-diffusion, others, such as Si<sub>3</sub>N<sub>4</sub> [9], suppress it. Therefore, it is possible to obtain spatially selective intermixing by defining different dielectric caps in different areas with photolithographic patterning.

Unfortunately, IFVD has poor reproducibility from run to run and poor discrimination between intermixed and unintermixed areas. It is very hard to deposit a Si<sub>3</sub>N<sub>4</sub> film with high purity: such films are usually a mixture of Si<sub>3</sub>N<sub>4</sub> and SiO<sub>2</sub>. In addition, Si<sub>3</sub>N<sub>4</sub> films are highly strained. It is believed that both the presence of SiO<sub>2</sub> in the silicon nitride and the high interface strain can affect the intermixing beneath the cap.

Further complications occur due to chemical reactions between the dielectric cap and the semiconductor. This is a particularly serious problem with Al-containing semiconductor alloys because Al is a very effective reducing agent. When a SiO<sub>2</sub> cap is in direct contact with an Al-containing alloy, a reaction of the type



occurs, and the resulting free Si can then act as IID species.

Therefore, a dielectric cap is needed to match the thermal and mechanical properties of the semiconductor. It is found that  $\text{SrF}_2$  [10] and  $\text{P:SiO}_2$  [11] are very good candidates. Experimental results show that using  $\text{SrF}_2$  as the cap almost completely inhibits QWI under conditions where  $\text{SiO}_2$  and  $\text{Si}_3\text{N}_4$  promote rapid intermixing. However,  $\text{SrF}_2$  masks induce surface damage of GaAs/AlGaAs due to thermal and mechanical stress when annealing temperature is above  $930^\circ\text{C}$ , limiting the maximum degree of selective intermixing achievable in this material system [12].

Bandgap shift differences as large as 100 mV have been observed from GaAs/AlGaAs samples capped with  $\text{SiO}_2$  and  $\text{P:SiO}_2$  [12]. This is attributed the well known fact that  $\text{P:SiO}_2$  films are more dense and void-free compared to that of  $\text{SiO}_2$  films and have a reduced built-in stress as compared with  $\text{SiO}_2$  [13], making them impermeable to Ga atoms. Extended cavity lasers of high quality have been fabricated with this technique [14].

As with IID, it is difficult to achieve large selective bandgap energy shifts in the InGaAs/InGaAsP MQW system using IFVD, due to the material's poor thermal stability as a high temperature annealing stage is employed.

### **5.1.3 Laser induced disordering (LID)**

Several laser induced disordering techniques have been developed. In some of these techniques, high power densities are used to melt the material and form an alloy semiconductor during the re-crystallisation [15]. On contrast to other techniques, this class of intermixing techniques does not rely on the introduction of point defects to enhance intermixing rates. However, the quality of the recrystallised material may be poor. Moreover, due to the requirement of a high temperature, dielectric capping is vital to preserve the stoichiometry of the semiconductor.

Other processes utilise the transient melting of CW and pulsed laser scanning to introduce encapsulant Si or other species into the epitaxial layers as sources for IID. IID takes place during a subsequent thermal annealing stage [16-17]. Such processes severely suffer from increased free-carrier absorption.

Although LID processes, which are clearly effective, have the potential to be impurity-free and to offer the possibility of direct-write, they can introduce thermal shock damage when using high energy pulses and cause a potentially undesirable redistribution of dopants outside the active layers. Furthermore, melting the semiconductor followed by recrystallisation gives complete intermixing and cannot be controlled to obtain partial bandgap shifts.

#### **5.1.4 Photo-absorption induced disordering (PAID)**

As an alternative technique to LID, photo-absorption induced disordering (PAID), which was first demonstrated by C.J. McLean et al [18], represents a promising QWI process, especially for the relatively unstable InGaAsP system.

During the process, a high density of photo-induced carriers is generated through band-to-band absorption of incident laser photons from a 1064 nm CW Nd:YAG laser within the active region of a MQW structure. The subsequent carrier relaxation and non-radiative recombination lead to the generation of heat within the active region and promote thermal inter-diffusion of the well and barrier atoms. The extent of the heating depends on many factors including the total energy absorbed by the active region, the power density and the period of illumination, as well as the degree of heat loss due to heat transport through the substrate and due to radiation. More importantly, it is layer composition-selective and potentially self-limiting. Intermixing only occurs in structures containing layers with smaller bandgap energy than that of the injected photon energy. Once the equivalence between the intermixed bandgap energy and the photon energy is reached, band-to-band absorption ceases and the heat generated in absorbing region is greatly reduced. This method is impurity free, requires only low power and does not involve a melt phase. Hence material with high optical and electrical quality can be obtained [19-20]. Spatial selectivity can be achieved by using a gold mask to reflect the incident photons thereby suppressing intermixing in the masked area. However, due to its thermal nature, diffusion of heat beneath the gold mask leads to a poor spatial resolution of 100-200  $\mu\text{m}$  [21].

### **5.1.5 Pulsed photo-absorption induced disordering (P-PAID)**

P-PAID employs high-energy laser pulses from a Q-switched laser to irradiate the MQW material and produce transient heating in the crystal. Point defects, created by the thermal expansion, diffuse during a high temperature anneal and enhance the QWI rate. This technique offers a considerable improvement in spatial resolution, which is better than 25  $\mu\text{m}$  [22-23]. One of the potential problems of P-PAID is the possible formation of extended defects. When a high density of point defects is created, the point defects may coalesce into extended defects that, in turn, are believed to trap mobile point defects and decrease the rate of intermixing [24]. In order to overcome this problem, a combination of P-PAID and PAID has been employed. In this combined process, the thermal energy supplied by PAID assists the rapid diffusion of point defects, reducing the probability of extended defect formation. This enables large bandgap shifts to be obtained and leads to an overall quality improvement in the processed wafer [25].

### **5.1.6 Ion implantation induced disordering**

The use of ion implantation to generate point defects through high-energy impact with the crystal matrix atoms has been used widely in many III-V material systems (AlGaAs, InP, etc.). This involves the use of relatively high-energy ion implantation to considerable depths ( $\sim 1 \mu\text{m}$ ), usually using electrically inactive implant species such as P and As [26-27]. Recently, to reduce the impact damage (i.e., unrecoverable non-radiative recombination centres within the wells), low-energy ion implantation has also been developed [28]. Although it has been shown that InGaAsP/InP bandgap widened lasers fabricated using ion implantation can

be actually reliable [29], the requirement for specialised facilities for implantation makes it relatively complicated and expensive.

## **5.2 Sputtering process induced disordering (SID)**

Recently, a novel intermixing technique, sputtering process induced disordering (SID), was developed in this Department and by Intense Photonics Ltd. The technique has been used on a number of different material systems including GaAs/AlGaAs, GaInP/AlGaInP, InGaAs/InGaAsP and InGaAs/InAlGaAs [30]. It is based on the generation of point defects during the sputtering process and the acceleration of atomic interdiffusion during a subsequent annealing stage and has so far proved highly successful for all of the above-mentioned material systems. In addition to its wide applicability, it is low cost and involves relatively simple processing stages.

In the process, the sample is first treated with a sputtering process for a period of time, during which a thin layer of SiO<sub>2</sub> is sputtered upon the sample surface with deposition rate of ~ 1 nm/minute. Then samples are annealed in a rapid thermal annealer (RTA) at a certain temperature. During the annealing stage, samples are placed between two Si wafers to prevent evaporation of the Group V elements. Finally, photoluminescence (PL) measurements are carried out at 77K to determine the bandgap shifts.

In the experiments of Kowalski et al [30], the intermixing rates of InGaAs/InGaAsP and InGaAs/AlInGaAs were clearly enhanced with bandgap shifts occurring at temperatures around 550°C. The shifts increased rapidly to give a large shift (~100 meV), at annealing temperatures of 700-750°C. Meanwhile, samples capped with PECVD SiO<sub>2</sub> exhibited no measurable bandgap shift up to 650°C. This clearly demonstrates the potential of the technique for achieving large bandgap shifts in some regions while complete suppression is maintained in other regions of the same sample.

### **5.3 Experimental investigation on sputtering process induced disordering**

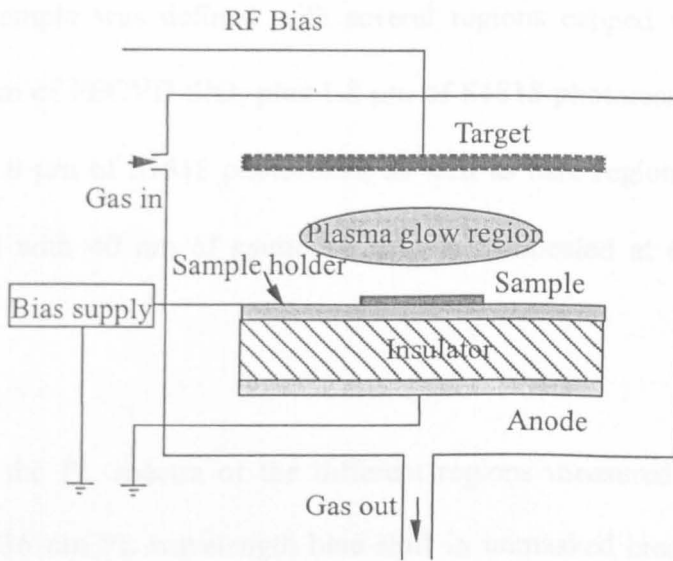
Some investigations of SID in the InGaAs/AlInGaAs material system were carried out to understand the influences of several parameters on the amount of intermixing.

The InGaAs/AlInGaAs (hereafter referred to as AlInGaAs) material investigated in the experiments was a standard un-strained multiple QW (MQW) laser structure grown on an (100)-oriented n<sup>+</sup>-type InP substrate by molecular beam epitaxy (MBE). The structure details are shown in Table 2.2.1.

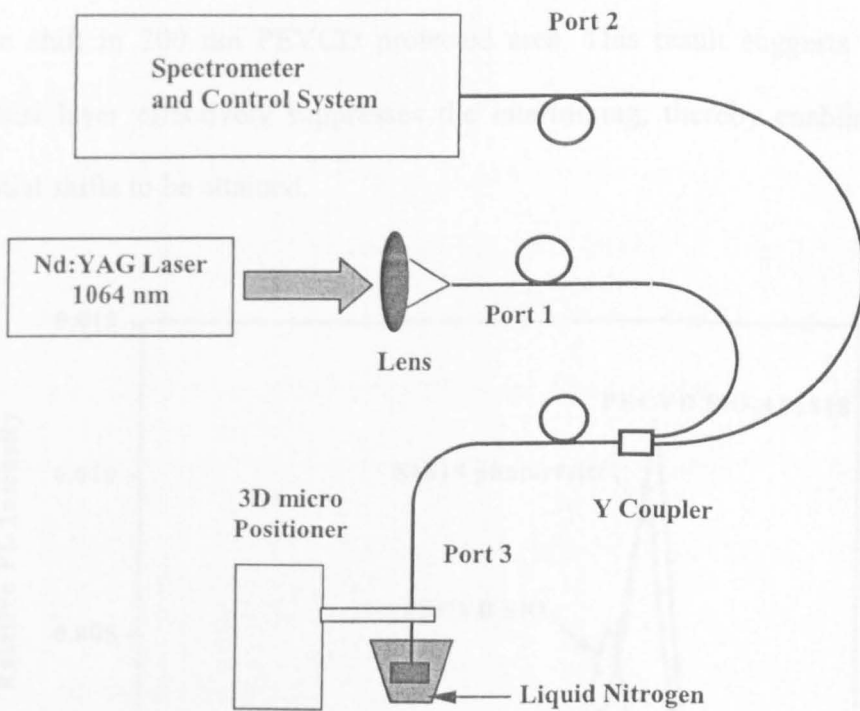
### 5.3.1 Experiment set-up

Sputtering was carried out in a Nordiko RF sputtering machine (see Figure 5.3.1(a)), at a RF power of 100 W and an self DC bias of 1 kV, using a 9:1 Ar:O<sub>2</sub> mixture with gas pressure of  $5 \times 10^{-3}$  mbar to generate the sputtering plasma.

The PL measurement set-up is shown in Figure 5.3.1(b). The beam from a Nd:YAG laser operating at 1064 nm is coupled into port 1 of a multimode optical fibre Y-type coupler using a 10× objective lens. The beam is launched out from port 2 of the coupler and stimulates the PL from the sample, which is glued, or mechanically attached by using a micro-positioner, on the fibre tip of port 2 of the coupler. The PL signal is collected by the fibre and launched out of port 3 of the coupler and coupled into a double spectrometer. A computer is used to control the spectrometer to scan the spectrum and record the signal. PL can be measured at both room temperature and 77 K (by immersing the samples in liquid nitrogen).



(a) Diagram of Nordiko RF sputtering machine



(b) Diagram of PL testing set-up

Fig.5.3.1 Diagrams of experiment set-up

### 5.3.2 Protection material

An AlInGaAs sample was defined with several regions capped with different materials: 200 nm of PECVD SiO<sub>2</sub> plus 1.8 μm of S1818 photoresist, 200 nm of PEVCD SiO<sub>2</sub>, 1.8 μm of S1818 photoresist, as well as bare region. The sample then was coated with 40 nm of sputtered SiO<sub>2</sub> and annealed at 640°C for 60 seconds.

Fig.5.3.2 shows the PL spectra of the different regions measured at 77 K. In contrast to the 136 nm PL wavelength blue shift in unmasked area, there is no shift in the area capped by 200 nm of PECVD SiO<sub>2</sub> plus 1.8 μm S1818 photoresist, a 3 nm blue shift in 1.8 μm S1818 photoresist protected area and a 16 nm blue shift in 200 nm PEVCD protected area. This result suggests that the photoresist layer effectively suppresses the intermixing, thereby enabling large differential shifts to be attained.

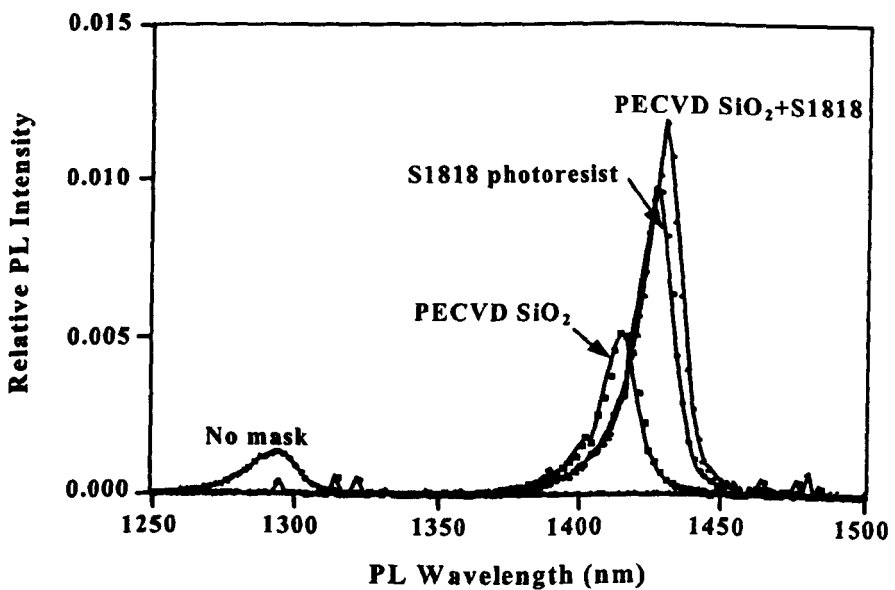


Fig.5.3.2 PL spectra of intermixed AlInGaAs samples protected with different materials

Figure 5.3.2 clearly indicates that, for this technique, spatial control can be easily achieved by masking the special region/regions with a 1.8  $\mu\text{m}$  thick layer of photoresist plus 200 nm of PECVD  $\text{SiO}_2$ .

### **5.3.3 Annealing temperature**

The annealing temperature is one of the major factors influencing the intermixing behaviour. A sample was defined with half its surface uncoated and the other half capped with 200 nm of PECVD  $\text{SiO}_2$  plus 1.8  $\mu\text{m}$  of photoresist. After sputtering 40 nm of  $\text{SiO}_2$ , the sample was cleaned to remove the photoresist and cleaved into small pieces, then annealed at different temperatures. Fig.5.3.3 shows the wavelength shift as a function of annealing temperature. It can be seen that there exist two particular temperature values: a threshold temperature and a saturation temperature. Above the threshold temperature, intermixing takes place and the bandgap energy shift is almost linearly proportional to the change in annealing temperature until the saturation temperature is reached. When the annealing temperature is higher than the saturation temperature, the bandgap energy shift is much less sensitive to the annealing temperature. For comparison, the wavelength shift against annealing temperature of a sample capped only with 200 nm of PECVD  $\text{SiO}_2$  plus 1.8  $\mu\text{m}$  of photoresist is also shown. Clearly, there is no bandgap energy shift below 650°C, which means the suppression of the intermixing is well maintained.

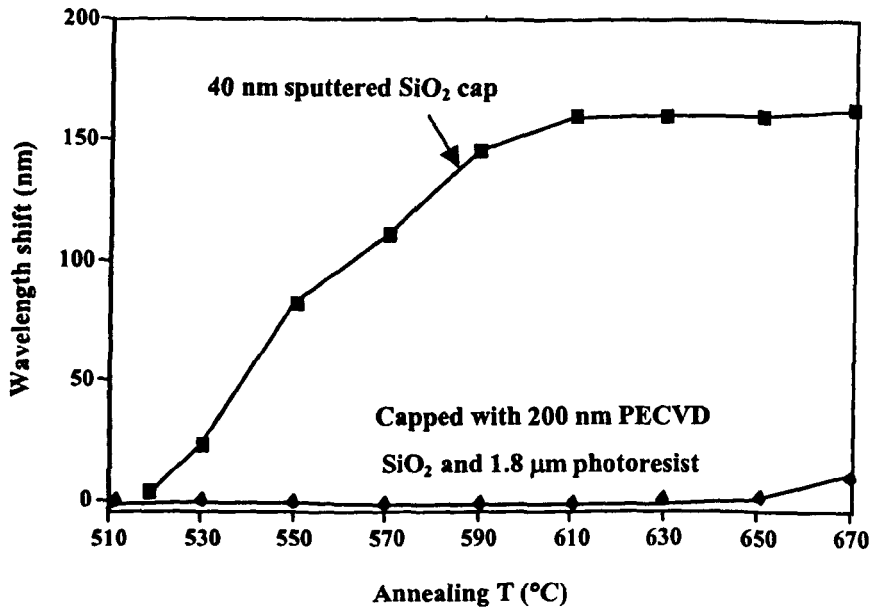


Fig.5.3.3 Wavelength shift as a function of annealing temperature in sputtering process induced disordering

As predicted in [30], we found the presence of an increased density of point defects may also promote atomic out-diffusion, especially during high temperature annealing. Fig.5.3.4 shows a micrograph of an intermixed area of an AlInGaAs sample after 750°C/60 s annealing. The diameters of the small out-diffusion spots are around one to several micrometers. Such spots were not found on the suppressed areas of the same sample. Clearly, such out-diffusion would influence the local optical and electric characteristics and degrade the performance of the device. Therefore, choosing a suitable annealing temperature is important so that both effective intermixing/suppression and minimal degradation in surface morphology can be achieved. In our situation, 630-640°C is chosen as the annealing temperature when making passive devices.

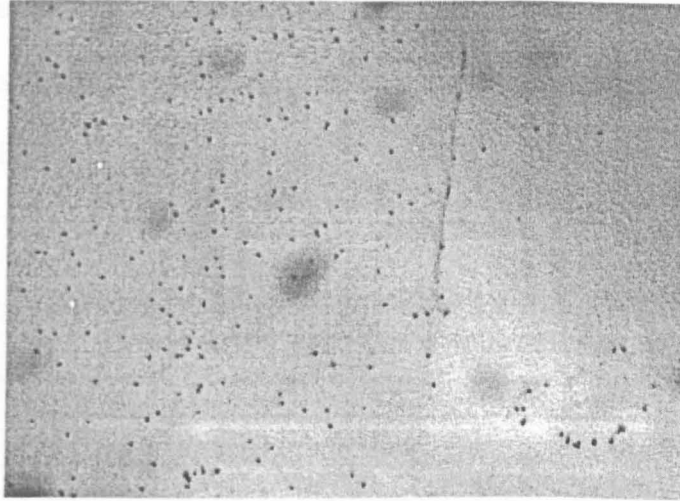


Fig.5.3.4 Evaporation spots on intermixed sample

### 5.3.4 Time of sputtering process

Experiment showed that at the selected annealing temperature of 630-640°C, samples treated for different sputtering times (10~200 minutes) achieved almost the same bandgap energy shift.

Uniformity is another issue that should be considered. The enhancement of intermixing is based on the generation of point defects. It is understandable that, if the sputtered layer is not thick enough, neither a sufficiently large concentration of point defects nor a uniform distribution of the point defect across the sample could be achieved. This would cause the poor uniformity of intermixing. It has been found that, although the deposition of as little as 5 nm of sputtered SiO<sub>2</sub> can yield a large bandgap energy shift, the uniformity of intermixing is not good. It is believed that using less than 10 nm of sputtered SiO<sub>2</sub> cannot give satisfactory intermixing uniformity. A 20 nm of sputtered SiO<sub>2</sub> process was therefore selected for our fabrication.

### 5.3.5 Measurement of spatial resolution

Spatial resolution measurements were carried out using the same set-up as shown in Figure 5.3.1(b). Instead of being glued or attached to the sample, the fibre tip of port 3 of the Y-type coupler was kept very close to the sample surface by adjusting the 3-dimensional micro-positioner. During the experiment, the fibre was moved across the boundary between the intermixed and suppressed regions in steps. Being a near field measurement, the minimum system resolution is determined by the receiver aperture, i.e. the diameter of the core of the multi-mode fibre. The scan step was also set to the same value of 50  $\mu\text{m}$ .

Figure 5.3.5 shows the measured spatial resolution of this novel technique is 50  $\mu\text{m}$ , equal to the minimum system resolution. The actual spatial resolution is therefore equal to or less than 50  $\mu\text{m}$ . Further research in the Department found that, with more accurate measuring techniques, the spatial resolution was of the order of a few micrometers [31]. This is much better than some intermixing techniques, such as PAID.

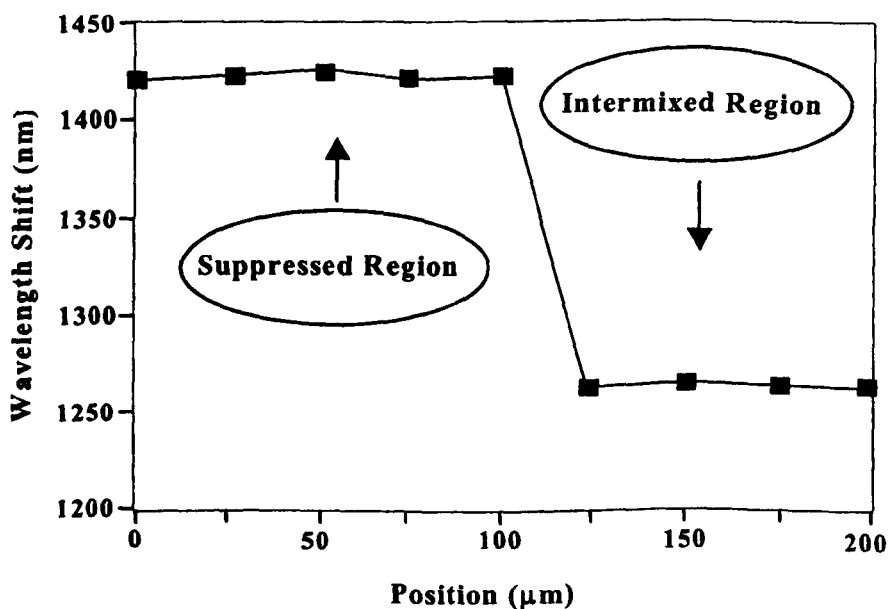


Fig.5.3.5 Spatial resolution measurement at 77K

Furthermore, SID is simpler, more reliable, more accurate and a much more practical technique than PAID.

Although the process is very similar to IFVD, the fundamental intermixing mechanism is very different to that of IFVD because a large bandgap shift was achieved at a much lower temperature than that of IFVD.

## 5.4 SIMS Measurement

To investigate the physics and chemistry underlying SID, secondary ion mass spectroscopy (SIMS) analysis was carried out by Loughborough Surface Analysis Limited using a 'IMS 4f' system. The experimental conditions are shown in Table 5.4.1.

Table.5.4.1 SIMS measurement conditions

Primary ion species	$O_2^+$
Primary ion energy	10 keV
Primary ion current	0.2~0.5 $\mu A$
Raster size	150~250 $\mu m$
Secondary ions	Positive and Negative
Transfer lens	150 $\mu m$
Analysed area	10, 30, 60 $\mu m$
Contrast aperture	No.3
Mass resolution	250

Analysis of the samples was performed using  $O_2^+$  primary ion bombardment and positive secondary ion detection as these conditions give good sensitivity to metals. The data was quantified using implanted reference materials and the depth scales were determined by measuring the sputtered crater depths by interference microscopy.

Two groups of samples were prepared. In Group 1, two InGaAsP samples were coated with 200 nm of sputtered  $SiO_2$ , then one of them was annealed in the RTA at a certain temperature for a period of time. For comparison, two samples of the same structure as Group 1 were coated with 200 nm of PECVD  $SiO_2$ , then one of them was annealed in the RTA with the same conditions as that of group 1.

Some interesting results arose from the SIMS measurements [32]:

The unannealed sample coated with 200 nm of sputtered  $SiO_2$  showed the presence of Cu at a concentration of  $1 \times 10^{21}$  through the  $SiO_2$  layer (Figure 5.4.1). Repeating the analysis after stripping the  $SiO_2$  showed Cu at  $1 \times 10^{21} \text{ cm}^{-3}$  was present on the semiconductor surface. The Cu concentration decreased very quickly within the InGaAs contact layer and reached below the detection level in the InP cladding region (Figure 5.4.2). No gallium was found in the sputtered  $SiO_2$  layer.

The annealed sample covered with 200 nm sputtered  $SiO_2$  also showed a high Cu concentration of  $4 \times 10^{20} \text{ cm}^{-3}$  through the sputtered  $SiO_2$  layer (Figure 5.4.3).  $SiO_2$ -stripped samples showed that Cu was present at  $1 \times 10^{21} \text{ cm}^{-3}$  on the

semiconductor surface and at more than  $1 \times 10^{18} \text{ cm}^{-3}$  through the InP cladding region and the core region (Figure 5.4.4). In this sample, a clear out-diffusion profile of Ga from InGaAs cap into  $\text{SiO}_2$  layer was also observed.

No copper was found above the instrumental detection limit in the samples covered with the PECVD layer, either before or after annealing. No great differences were found between the annealed and non-annealed samples, although a low concentration of gallium ( $\sim 10^{17} \text{ cm}^{-3}$ ) was detected in the silica layer of the annealed sample (Figure 5.4.5 and Figure 5.4.6).

These results strongly suggest that the diffusion of Cu, which is introduced during the sputtering process, is involved in the QWI and enhances the QWI. As one of the 3d transition metals, Cu has a very high diffusion coefficient  $D = 2 \times 10^{-3} \text{ cm}^2/\text{sec}$  at  $900 \text{ }^\circ\text{C}$ , and even at temperatures as low as  $400 \text{ }^\circ\text{C}$   $D = 2.5 \times 10^{-5} \text{ cm}^2/\text{sec}$  [33]. Cu is known to diffuse interstitially and to move onto group III lattice sites through the ‘kick-out’ mechanism. Because of its fast diffusion, Cu is much more efficient than many other impurities in generating point defects. For the same reason, it can enhance QWI at relatively low temperatures, as reported in Section 5.3.3.

Although SID has been proved a very effective method in QWI enhancement, there are still some issues to be solved. The most important one is the control of Cu concentration within the semiconductor. Figure 5.4.4 clearly shows that directly depositing a layer of sputtered  $\text{SiO}_2$  on a semiconductor causes a Cu concentration as high as  $1 \times 10^{18} \text{ cm}^{-3}$  across the core region. This could lead to

strong impurity-related non-radiation absorption, which is not acceptable in any opto-electronic integration. In fact, the high absorption has been observed in the fabrication of monolithically integrated Mach-Zehnder asymmetric interferometer demultiplexer (See Chapter 8). In the next chapter, we will introduce an improved SID technique, which can significantly reduce the Cu concentration within the core region and makes SID a practical technique in opto-electronic integration.

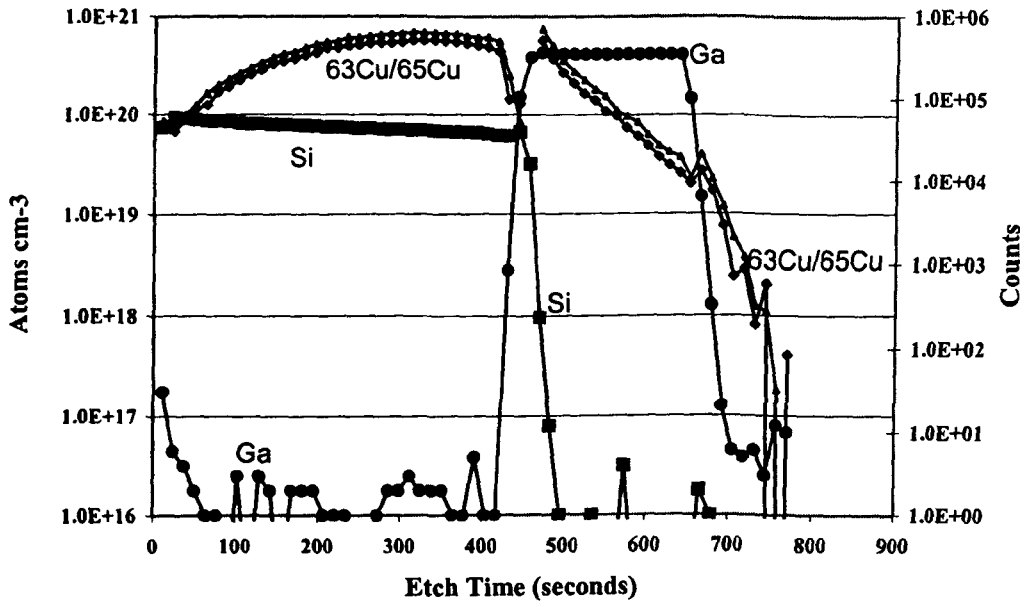


Fig. 5.4.1 SIMS of non-annealed MR1377 sample covered with 200 nm sputtered SiO<sub>2</sub>

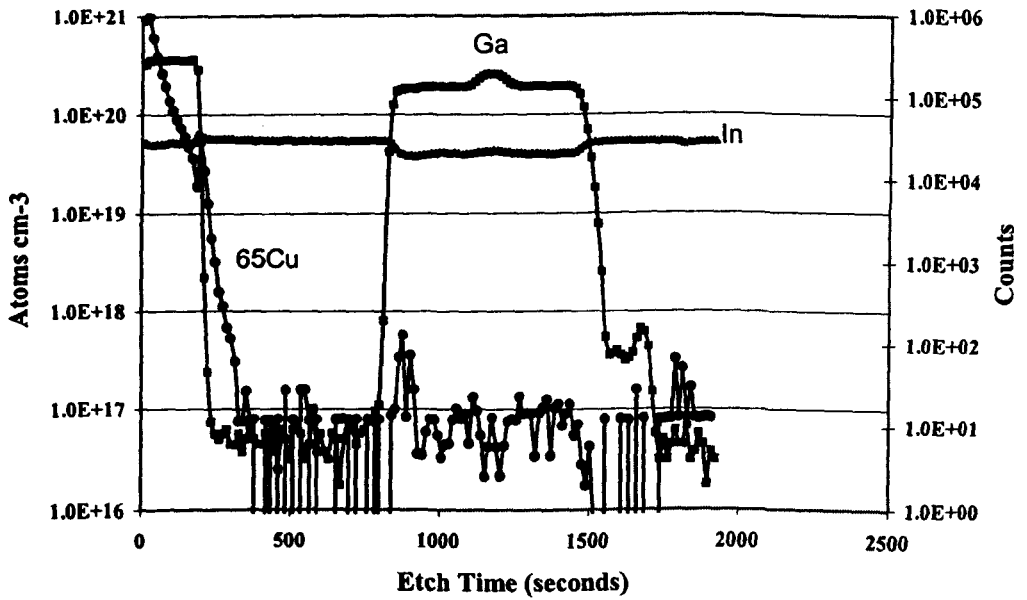


Fig 5.4.2 High accuracy SIMS of non-annealed MR1377 sample with 200nm sputtered SiO<sub>2</sub> stripped-off

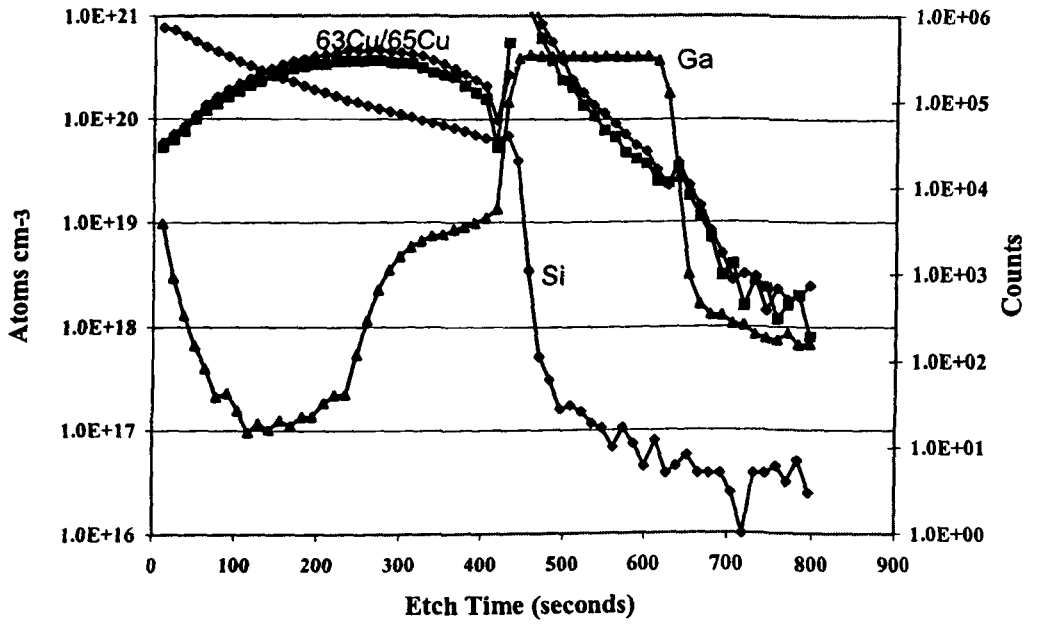


Fig. 5.4.3 SIMS of annealed MR1377 sample covered with 200 nm sputtered SiO<sub>2</sub>

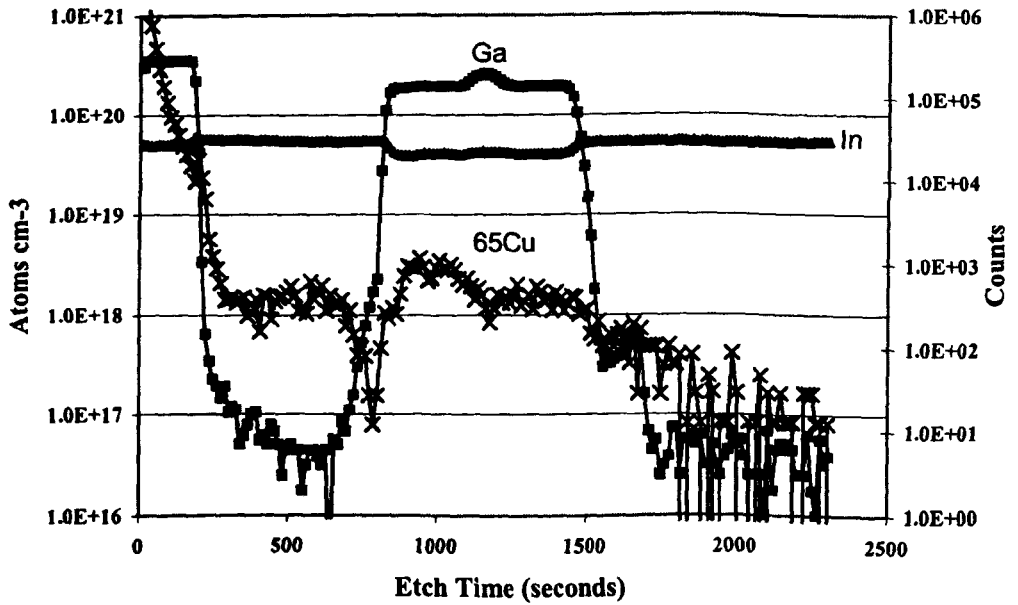


Fig 5.4.4 SIMS of annealed MR1377 sample with 200 nm sputtered SiO<sub>2</sub> stripped-off

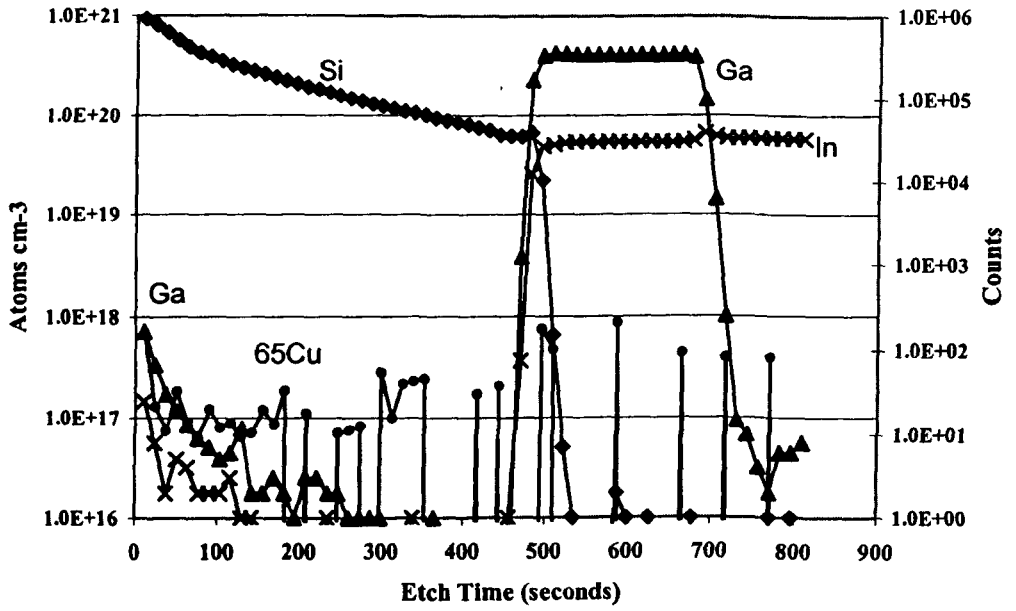


Fig. 5.4.5 SIMS of MR1377 non-annealed sample covered with 200 nm PECVD SiO<sub>2</sub>

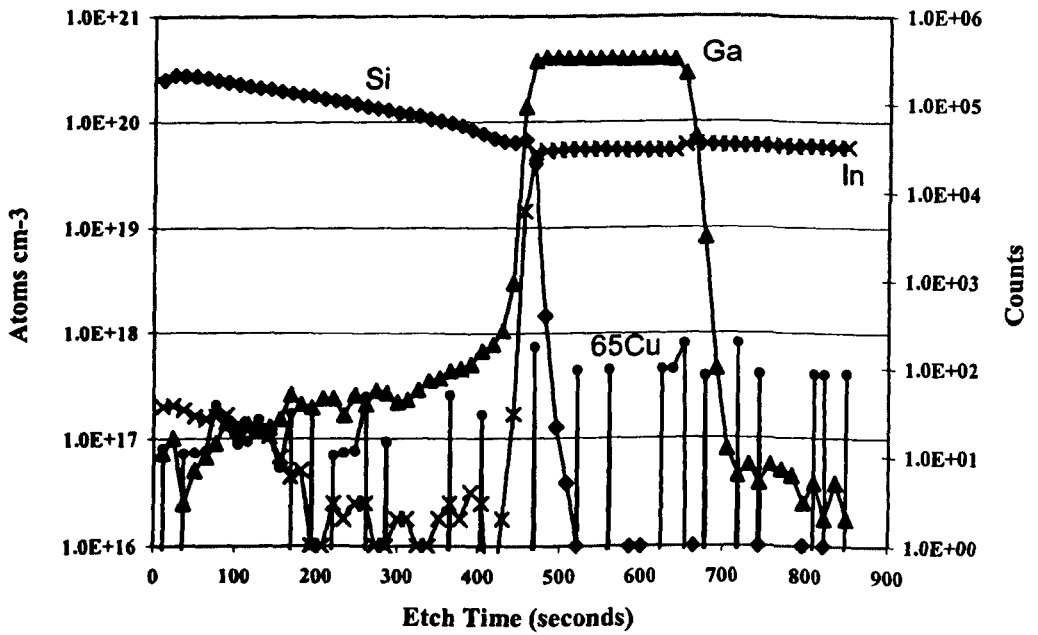


Fig. 5.4.6 SIMS of MR1377 annealed sample with 200 nm PECVD SiO<sub>2</sub>

## 5.5 Summary

In this chapter, several quantum well intermixing techniques have been reviewed. A novel intermixing technique, sputtering process induced disordering (SID), has been described. The influence of several physical parameters on the intermixing, including the annealing temperature, protection material, thickness of sputtered SiO<sub>2</sub> have been reported, and the conditions giving good uniformity determined. The largest bandgap shift of 170 nm was achieved in 1.55 μm InGaAs/AlInGaAs MQW material. Measurements of the spatial resolution have suggested that SID has high spatial resolution of the orders of a few micrometers, which is very useful for two-dimensional opto-electronic integration. SIMS analysis has disclosed that during the SID, Cu was introduced, which leads to a change in the concentration of point defects, and is responsible for the increased rate of atomic interdiffusion during the anneal stage and enhancing the QWI.

## Reference

- [1] M. Aoki, M. Suzuki, H. Sano, T. Kawano, T. Ido, T. Taniwatari, K. Uomi and A. Takai, 'InGaAs/InGaAsP MQW electroabsorption modulator integrated with a DFB laser fabricated by band-gap energy control selective-area MOCVD', *IEEE J. Quantum Electronics*, Vol.29, pp.2088-2096, 1993
- [2] M. Gibbon, J.P. Stagg, C.G. Cureton, E.J. Thrush, C.J. Jones, R.E. Mallard, R.E. Pritchard, N. Collins, and A. Chew, 'Selective area low-pressure MOCVD of GaInAsP and related materials on planar InP substrates', *Semiconductor Science & Technology*, Vol.8, pp.998-1010, 1993
- [3] J.H. Marsh, 'Quantum well intermixing', *Semiconductor Science & Technology*, Vol.8, pp.1136-1155, 1993
- [4] V.W.D. Laidig, N. Holonyak Jr., M.D. Camras, K. Hess, J.J. Coleman, P.D. Dapkus, and J. Bardeen, 'Disordering of an AlGaAs/GaAs super-lattice by impurity diffusion', *Applied Physics Letter*, Vol.38, pp.776-778, 1981
- [5] M. Suzuki, H. Tanaka, S. Akiba, and Y. Kushiro, 'Electrical and optical interactions between integrated InGaAsP/InP DFB lasers and electroabsorption modulators', *J. Lightwave Technology*, Vol.6, pp779-785, 1988
- [6] D.G. Deppe, N. Holonyak Jr., 'Atom diffusion and impurity-induced layer disordering in quantum well III-V semiconductor heterostructures', *J. of Applied Physics*, Vol.64, R93-R113, 1988
- [7] A.C. Bryce, J.H. Marsh, R. Gwiliam, and R.W. Glew, 'Impurity induced disordering in InGaAs/InGaAlAs quantum wells using implanted fluorine and boron', *J. of IEE Proceeding*, Vol.138, pp87-90, 1991

- [8] L.J. Guido, N. Holonyak Jr., K.C. Hsieh, R.W. Kaliski, W.E. Plano, R.D. Burnham, R.L. Thornton, J.E. Epler, and T.L. Paoli, 'Effect of dielectric encapsulation and As overpressure on Al-Ga interdiffusion in  $\text{Al}_x\text{Ga}_{1-x}\text{As}$  quantum well heterostructures', *J. of Applied Physics*, Vol.55, pp.540-542, 1989
- [9] L.J. Guido, K.C. Hsieh, N. Holonyak Jr., R.W. Kaliski, V. Eu, M. Feng, and R.D. Burnham, 'Impurity induced layer disordering of Si implanted  $\text{Al}_x\text{Ga}_{1-x}\text{As}/\text{GaAs}$  quantum well heterostructures – layer disordering via diffusion from extrinsic dislocation loops', *J. of Applied Physics*, Vol.61, pp1329-1334, 1987
- [10] B.S. Ooi, K. McIlvaney, M.W. Street, A.S. Helmy, S.G. Ayling, A.C. Bryce, J.H. Marsh, and J.S. Roberts, 'Selective quantum well intermixing in GaAs-AlGaAs structure using impurity free vacancy diffusion', *IEEE J. of Quantum Electronics*, Vol.33, pp.1784-1793, 1997
- [11] E.V.K. Rao, A. Hamoudi, Ph. Krauz, M. Juhel, and H. Thibierge, 'New encapsulant source for III-V quantum well disordering', *Applied Physics Letter*, Vol.66, pp472-474, 1995
- [12] P. Cusumano, B.S. Ooi, A.S. Helmy, S.G. Ayling, A.C. Bryce, J.H. Marsh, B. Voegelé, and M.J. Rose, 'Suppression of quantum well intermixing in GaAs/AlGaAs laser structures using phosphorus-doped  $\text{SiO}_2$  encapsulant layer', *J. of Applied Physics*, Vol.81, pp2445-2447, 1997
- [13] S.K. Ghandi, *VLSI Fabrication Principles*, 2<sup>nd</sup> edition. New York: Wiley, pp530-532, 1994, and references therein.
- [14] P. Cusumano, J H. Marsh, M.J. Rose, and J.S. Roberts, 'High-quality extended cavity ridge lasers fabricated by impurity free diffusion with a novel masking technique', *IEEE Photonics Technology Letter*, Vol.9, pp.282-284, 1997

- [15] J.D. Ralston, A.L. Moretti, R.K. Jain, and F.A. Chambers, 'Intermixing of AlxGaAs/GaAs superlattices by pulsed laser irradiation', *Applied Physics Letter*, Vol.50, pp.1817-1819, 1987
- [16] J.E. Epler, F.A. Ponce, F.K.J. Endicott and T.L. Paoli,, 'Laser-induced disordering of GaAs/AlGaAs superlattice and incorporation of Si impurity', *Applied Physics Letter*, Vol.49, pp.1447-1449, 1986
- [17] A. Rys, Y. Shieh, A. Compaan, H. Yao, and A. Bhat, 'Pulsed laser annealing of GaAs implanted with Se and Si', *Optical Engineering*, Vol.29, pp.329-338, 1990
- [18] C.J. McLean, J.H. Marsh, R.M. De La Rue, A.C. Bryce, B. Garrett, and R.W. Glew, 'Layer selective disordering by photoabsorption-induced thermal-diffusion in InGaAs/InP based multiquantum well structures', *Electronics Letter*, Vol.28, pp.1117-1119, 1992
- [19] A. McKee, C.J. McLean, A.C. Bryce, R.M. De La Rue, and J.H. Marsh, 'High-quality wavelength tuned multiquantum-well GaInAs/GaInAsP laser fabricated using photoabsorption induced disordering', *Applied Physics Letter*, Vol.28, pp.2263-2265, 1994
- [20] G. Lullo, A. McKee, C.J. McLean, A.C. Bryce, C. Button, and J.H. Marsh, 'Fabrication of electroabsorption optical modulators using laser disordered GaInAs/GaInAsP multiquantum-well structures', *IEEE J. of Quantum Electronics*, Vol.33, pp.1623-1625, 1994
- [21] A. McKee, C.J. McLean, G. Lullo, A.C. Bryce, R.M. De La Rue, and J.H. Marsh, 'Monolithic integration in InGaAs/InGaAsP multi-quantum-well structures using laser intermixing', *IEEE J. of Quantum Electronics*, Vol.33, pp.45-55, 1997

- [22] C.J. McLean, A. McKee, G. Lullo, A.C. Bryce, R.M. De La Rue, and J.H. Marsh, 'Quantum-well intermixing with high spatial selective using a pulsed-laser technique', *Electron. Letter*, Vol.31, pp.1285-1286, 1995
- [23] S.J. Fancey, G.S. Buller, J.S. Massa, A.C. Walker, C.J. McLean, A. McKee, A.C. Bryce, J.H. Marsh, and R.M. De La Rue, 'Time-resolved photoluminescence microscopy of GaInAs/GaInAsP quantum wells intermixed using pulsed laser technique', *J. of Applied Physics*, Vol.79, pp.9390, 1996
- [24] B.S. Ooi, A.C. Bryce, J.H. Marsh, and J. Martin, 'Transmission electron-microscopy study of fluorine and boron-implanted and annealed GaAs/GaAlAs', *Applied Physics Letter*, Vol.65, pp.85-87, 1994
- [25] B.C. Qiu, A.C. Bryce, R.M. De La Rue, and J.H. Marsh, 'Monolithic integration in InGaAsP/InP multiple quantum well structures using laser processing', *IEEE Photonics Technology Letter*, Vol.10, pp769-771, 1998
- [26] L.B. Allard, G.C. Aers, P.G. Piva, P.J. Poole, M. Buchanan, I.M. Templeton, T.E. Jackman, S. Charbonneau, U. Akano, and I.V. Mitchell, 'Threshold dose for ion-induced intermixing in InGaAs/GaAs quantum wells', *Applied Physics Letters*, Vol.64, pp2412-2414, 1994
- [27] S. Charbonneau, P.J. Poole, Y. Feng, G.C. Aers, M. Dion, M. Davies, R.D. Goldberg, and I.V. Mitchell, 'Band-gap tuning of InGaAs/InGaAsP/InP laser using high energy ion implantation', *Applied Physics Letters*, Vol.67, pp2954-2965, 1995
- [28] M. Paquette, V. Aimez, J. Beauvais, P.J. Poole, S. Charbonneau, and A.P. Roth, 'Blueshifting of InGaAsP-InP laser diodes using a low energy ion implantation technique: comparison between strained and lattice matched

quantum well structures', IEEE J. of Selected Topics in Quantum Electronics, Vol.4, pp741-745, 1998

[29] J.P. Noel, D. Melville, T. Jones, F.R. Shepherd, C.J. Miner, N. Puetz, K. Fox, P.J. Poole, Y. Feng, E.S. Koteles, S. Charbonneau, R.D. Goldberg, I.V. Mitchell, 'High-reliability blue-shifted InGaAsP/InP lasers', *Applied Physics Letter*, Vol.69, pp.3516-3518, 1996

[30] O.P. Kowalski, C.J. Hamilton, S.D. McDougall, J.H. Marsh, A.C. Bryce, R.M. De La Rue, B. Vögele, C.R. Stanley, C.C. Button, J.S. Roberts, 'A universal damage induced technique for quantum well intermixing', *Applied Physics Letter*, Vol.72, pp.581-584, 1998

[31] A.S. Helmy, personal communication.

[32] 'SIMS analysis of samples MR1377, B725 and M4-5228', *Test report of No.SI.IPL.929*, Loughborough Surface Analysis Limited, November, 2000

[33] M.S. Skolnick, E.J. Foulkes, and B. Tuck, 'Transition metal diffusion in InP: Photoluminescence investigation', *J. of Applied Physics*, Vol. 51, pp2951-2961, 1984

## CHAPTER 6

### NOVEL MULTI-BANDGAP QUANTUM WELL INTERMIXING TECHNIQUE IN 1.55 $\mu\text{m}$ InGaAs/AlInGaAs AND InGaAs/InGaAsP MQW MATERIAL AND ITS APPLICATIONS

In this chapter, a novel QWI technique based on SID, which addresses the creation of multi-bandgap structures, is introduced. Assessment of the optical and electrical characteristics of the bandgap-widened material is presented. Several applications of the novel QWI technique are described, such as bandgap tuned stripe/ridge waveguide lasers and an integrated crosspoint switch.

## 6.1 Introduction

Monolithic integration of different optical components onto a single epitaxial layer is highly desirable in optical communication systems. One of the fundamental demands for monolithic integration is to realise multiple semiconductor bandgaps within one epitaxial layer. For example, a  $2 \times 2$  cross-point switch incorporating semiconductor optical amplifiers, passive waveguide splitters and electro-absorption (EA) modulators typically requires three bandgaps [1]. The operation wavelength for the switches, and therefore for the amplifiers, is  $1.55 \mu\text{m}$ , but a much wider bandgap is required for the passive waveguides in order to minimise the absorption of light propagating in the waveguides. Moreover, the optimum absorption bandgap for the EA modulators is  $\sim 20\text{-}50 \text{ nm}$  shorter than that of the amplifiers, to realise a low insertion loss and high extinction ratio.

Another example of multi-bandgap energy structure would be a multi-wavelength laser array, of considerable importance for wavelength division multiplexing (WDM) [2]. Multi-bandgap energy structures also find applications in devices such as optical colour printing [3], remote sensing [4] and photo-detectors [5].

Many techniques are currently under investigation for such a purpose. Selective regrowth techniques appear promising, but are complicated and expensive [6]. Other approaches are based on quantum well intermixing (QWI). Several QWI techniques, such as those described in Chapter 5, have previously been reported for producing several bandgaps on one chip. In the GaAs/AlGaAs QW system,

impurity free vacancy disordering (IFVD) has been adapted to achieve selective intermixing in selected areas [7]. Recent development of ion implantation induced disordering has made it a promising way to achieve multiple bandgap structures. Although it has been shown that InGaAsP/InP bandgap widened lasers fabricated using ion implantation can be reliable [8], the requirement for specialised implantation facilities makes it relatively complicated and expensive. Photo-absorption induced disordering (PAID) is one potential approach for the InGaAs/InGaAsP material system [9]. In this process, different regions were irradiated by the laser for different times to give different bandgap energies. However the PAID process uses a CW laser to induce heating, so its spatial selectivity is very poor and the Gaussian beam profile of the laser intensity causes nonuniformity across the intermixing area. Another problem generated from the nonuniform, high temperature heating is degradation of the surface planeness, which makes subsequent fabrication very difficult. Furthermore, as it relies on the limited thermal stability of the material system being processed, PAID is confined mainly (though not exclusively) to the InGaAsP system. For more thermal-stable material systems, such as AlInGaAs, PAID is of limited application as the process temperature is too high.

The recently developed sputtering induced intermixing [10, 11] has been applied to fabricate three-bandgap integrated devices (amplifier, modulator and passive waveguide) on III-V semiconductors such as InGaAs/InGaAsP [12] and InGaAs/AlInGaAs structures. During the fabrication, deposition of silica onto surface of the passive regions took place for 200 minutes while the other two regions were protected by PECVD SiO<sub>2</sub> plus photoresist to suppress any

intermixing. After removing the photoresist, the sample was annealed in a rapid thermal annealer (RTA) and giving a QW shift of  $\sim 100$  nm in the passive regions. The sample was then patterned by photolithography and HF wet etching to allow a second sputtering step directly onto both the passive and modulator regions, while the amplifier region was capped by PECVD SiO<sub>2</sub> and photoresist. Again, after removing the photoresist the sample was annealed in the RTA. By controlling the temperature of the second annealing process, a 40~50 nm blue shift was achieved in the modulator region. Obviously, this process involved repetitive sputtering and annealing steps, and therefore was slow and not very reliable.

Qiu et al. reported a different approach to create two-shifted-bandgap structure, again using SID [13]. The approach is based on the fact that samples treated with SID process exhibit bandgap shifting at a significantly lower temperature than those required for thermally induced intermixing of the material (See Figure 5.3.3). This means that, for temperatures higher than the saturation value discussed in Chapter 5, it is possible to obtain two different bandgap shifts in one annealing stage. Although it has been successfully applied to the 2×2 integrated crosspoint optical switch (modulator, passive waveguides and couplers), it is impossible to achieve a three-bandgap structure (especially including the as-grown bandgap) with this technique. Another major drawback is that a high annealing temperature is needed which may cause poor surface morphology as described in Section 5.3.3.

In this chapter, we will introduce a novel technique, based on SID, to create multi-bandgap structures. Compared with the other methods discussed above, this

technique is simpler, more reliable and the tuning of bandgap is precise [14]. In this chapter, following the sections describing the optical and electrical characteristics of the processed material, several applications of this novel QWI technique will be presented.

## **6.2 Multi-bandgap structure addressed using SID**

In section 5.4, it was disclosed that Cu, as an impurity, plays an important role in SID. Diffusing interstitially into the semiconductor, Cu alters the Fermi level, moves onto group III lattice sites through the 'kick-out' mechanism and leads to the change of the equilibrium concentration of certain point defects, resulting in an increased rate of atomic interdiffusion during a subsequent anneal stage and enhancing the QWI. From Fig.5.3.2, we can find that, with 20 nm of sputtered SiO<sub>2</sub> directly on the sample surface and 640°C annealing for 60 seconds, there was a blue shift of 136 nm in the region without the protection layer. Under the same process conditions, there is only a 16 nm blue shift in the region capped with 200 nm of PECVD SiO<sub>2</sub> prior to sputter deposition. Considering the annealing temperature is lower than the threshold temperature of thermally induced intermixing, this much smaller blue shift can only be explained by the PECVD cap partially inhibiting the diffusion of Cu from the sputtered SiO<sub>2</sub> layer into the semiconductor. This reduces the density of point defects and concentration of Cu, leading to a significantly reduced degree of intermixing during annealing.

This means that, by locally controlling the thickness of the PECVD silica cap, it is possible to control the concentration of point defects generated by the diffusion of Cu in the III-V semiconductor during the anneal stage, hence the local bandgap shift in the QW.

From the above discussion, one of the most attractive features of this method is that, by defining the local thickness of PECVD SiO<sub>2</sub>, as many bandgap energies as desired can be defined across the same sample. Furthermore, being a diffusion barrier, the PECVD SiO<sub>2</sub> layer could significantly reduce the concentration of Cu diffused into the semiconductor, which should lead to reduction of any optical absorption related to Cu.

To investigate the relationship between the blue shift in the bandgap and the thickness of the protection layer, a set of experiments was designed for both the InGaAs/AlInGaAs and InGaAs/InGaAsP material systems.

The InGaAs/AlInGaAs structure is shown in Table 2.2.1. Similar to the InGaAs/AlInGaAs samples, InGaAs/InGaAsP structure was a standard unstrained multiple QW (MQW) laser structure grown on a (100)-oriented n-type InP substrate by metal organic vapour phase epitaxy (MOVPE). The structure was capped with a p-doped ( $5 \times 10^{18} \text{cm}^{-3}$ ) 200 nm In<sub>0.53</sub>Ga<sub>0.47</sub>As contact layer. Consisting of five 6.5 nm wide InGaAs wells with 12 nm wide InGaAsP barriers, the active region was bounded by a 50 nm undoped stepped graded index (GRIN) waveguide core consisting of 80 nm InGaAsP confining layers, centrally located within a 1.4 μm thick InP cladding layer. The first 0.2 μm of the upper cladding

layer was an undoped spacer layer and the remaining  $1.2\ \mu\text{m}$  was doped with Zn to a concentration of  $7 \times 10^{17}\ \text{cm}^{-3}$ . The lower cladding layer was Si doped to a concentration of  $5 \times 10^{18}\ \text{cm}^{-3}$ .

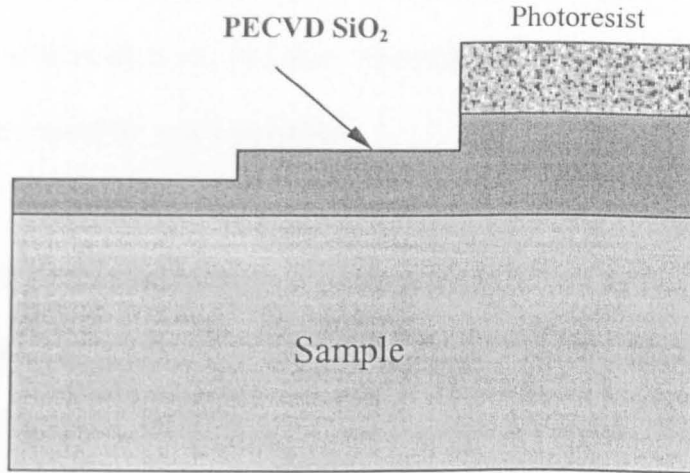


Fig.6.2.1. Schematic of sample patterned with different thickness of PECVD SiO<sub>2</sub>

The first step was to deposit a cap layer of 200 nm of PECVD SiO<sub>2</sub> onto the samples. The PECVD SiO<sub>2</sub> layer was then patterned such that its thickness varied over the sample, by using a combination of photolithography and etching (See Fig.6.2.1.). One area had a photoresist mask left on it, in order to suppress intermixing completely. Next, a 20 nm sputter process was carried out over the whole sample. The sample was then placed in acetone to remove the photoresist and annealed in a RTA at 650°C for 60 seconds. Finally, 77 K photoluminescence (PL) spectra were measured across the sample to determine the resultant PL shifts, using the set-up shown in Figure 5.3.1.

When defining the SiO<sub>2</sub> protection layer, two methods can be used. Reactive ion dry etching with C<sub>2</sub>F<sub>6</sub> or CHF<sub>3</sub> has a good uniformity and relatively slow etching

rate (40 nm/min. for  $C_2F_6$  and 35 nm/min. for  $CHF_3$ ). This offers good thickness control, but ion bombardment during the etch may introduce some defects. To avoid any confusion, HF wet etching was used in the experiment. As the etch rate of normal HF solution is quite high ( $\sim 20$  nm/sec.), a diluted HF solution (HF: water = 1:9) with an etch rate less than 10 nm/sec. was used so that the protection layer thickness could be well controlled.

Fig.6.2.2 shows the variation of the blue shift in the PL spectra as a function of the thickness of the PECVD  $SiO_2$ . It can be seen that, by using different PECVD  $SiO_2$  protection thicknesses, the blue shifts can be precisely tuned from 0 nm to over 160 nm for InGaAs/AlInGaAs and 0 nm to 100 nm for InGaAs/InGaAsP material [14].

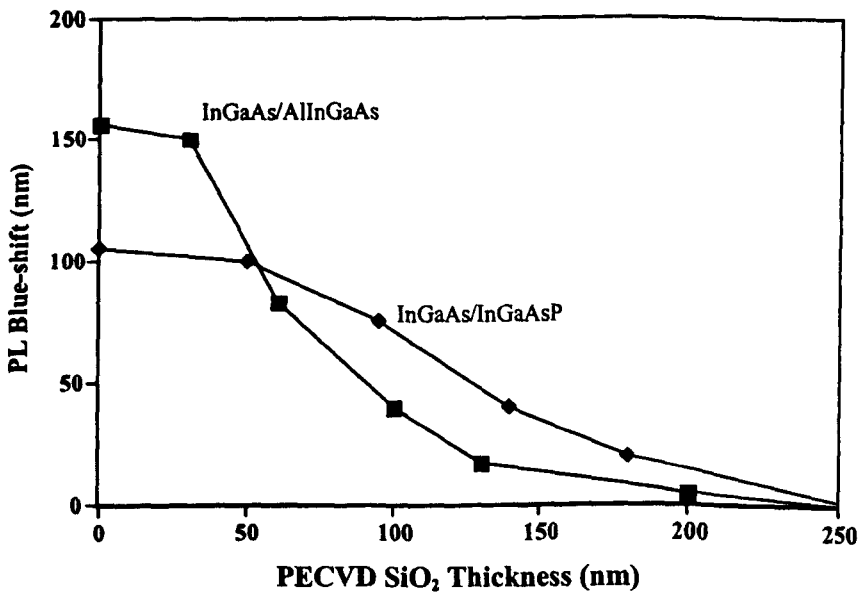


Fig. 6.2.2 PL blue shift as function of the thickness of PECVD

SIMS analysis was carried out on some InGaAsP bandgap-tuned samples (MOCVD MR1201, structure shown in Table. 6.2.1) again by Loughborough Surface Analysis Limited. The experimental conditions are shown in Table 6.2.2.

Table 6.2.1 Material structure MOCVD MR1201

Repeats	Thick. (nm)	Material	Dopant	Type	Conc(cm <sup>-3</sup> )
1	100	GaIn <sub>0.53</sub> As	Zn	p	3.0E+18
1	50	InGaAsP(1.18)	Zn	p	1.0E+18
1	1400	InP	Zn	p	7.0E+17
1	200	InP spacer		I	
1	80	InGaAsP (1.1)		I	
1	50	InGaAsP (1.18)		I	
5	12	InGaAsP (1.26)		I	
5	5.5	In <sub>0.53</sub> GaAs QW		I	
1	12	InGaAsP (1.26)		I	
1	50	InGaAsP (1.18)	Si	n	7.0E+17
1	80	InGaAsP (1.1)	Si	n	8.0E+17
1	900	InP	Si	n+	2.0E+18

Table.6.2.2 SIMS measurement conditions

Primary ion species	$O_2^+$
Primary ion energy	10keV
Primary ion current	30~200 nA
Raster size	125~175 $\mu\text{m}$
Secondary ions	Positive
Transfer lens	150 $\mu\text{m}$
Analysed area	10, 30, 60 $\mu\text{m}$
Contrast aperture	No.2 and No.3
Mass resolution	250

Analysis of the samples was performed using  $O_2^+$  primary ion bombardment and a positive secondary ion detection to optimise the sensitivity to Cu. The data were quantified using an implanted reference of Cu in InP and the depth scales were determined by measuring the sputtered crater depths by interference microscopy.

It was found that samples with different protection layers showed different concentrations of Cu at their surfaces but no significant differences in the cladding layers ( $\sim 3 \times 10^{18} \text{ cm}^{-3}$ ). The concentration decreased down to detection limit, which is around  $3 \times 10^{18} \text{ cm}^{-3}$ , within the core region [15].

### **6.3 Assessment of the post-process material characteristics**

General requirements of the processed material are maintaining good electrical and optical qualities in all the regions, so that different device functions can be realised.

A typical two-bandgap device consists of a completely suppressed region and an intermixed region. As the intermixed region is usually intended to form a passive section, for example an integrated external cavity, or a coupler or a waveguide, target specifications are mainly related to optical transmission. The assessment needs to address the amount of bandgap energy shift and optical transmission loss. For multi-bandgap energy structures, the requirements are different, especially for the partially intermixed regions. As such regions are mainly intended to be used in active devices (bandgap-tuned lasers and EA modulators, etc.), the basic requirement is that good quantum well characteristics, such as low threshold current density, high internal efficiency and low internal loss, should be maintained in intermixed material. Hence the assessment of multi-bandgap energy structures addresses these aspects.

In our investigation, to assess the material characteristics of a multi-bandgap energy structure after the intermixing process, oxide stripe lasers were made on both intermixed InGaAs/AlInGaAs and InGaAs/InGaAsP samples.

First, an InGaAs/AlInGaAs sample was defined into four regions with protection layers of 80 nm, 110 nm, 130 nm and 200nm plus S1818 photoresist. After the 20

nm sputtered SiO<sub>2</sub> process, the sample was cleaned and annealed in an RTA at 650°C for 90 seconds. Then, the PECVD protection layer, as well as the sputtered cap, were removed by HF wet etching. A fresh 200 μm PECVD SiO<sub>2</sub> layer was deposited onto the sample. 80 μm wide windows with a 300 μm pitch were then opened across the whole sample using photolithography and HF etching. The sample was thinned to 150 μm and metal contact layers (p-side, Ti : Pd : Au :: 20 : 20 : 150 nm; n-side, Au : Ge : Au : Ni : Au :: 14 : 14 : 14 : 10 : 200 nm) were evaporated onto both surfaces and alloyed in the RTA at 360°C for 60 seconds. Finally, the sample was cleaved into individual lasers with cavity lengths of 400, 600, 800 and 1000 μm, in each region. The lasers were tested under pulsed conditions (400 ns pulse at a 1 kHz repetition rate).

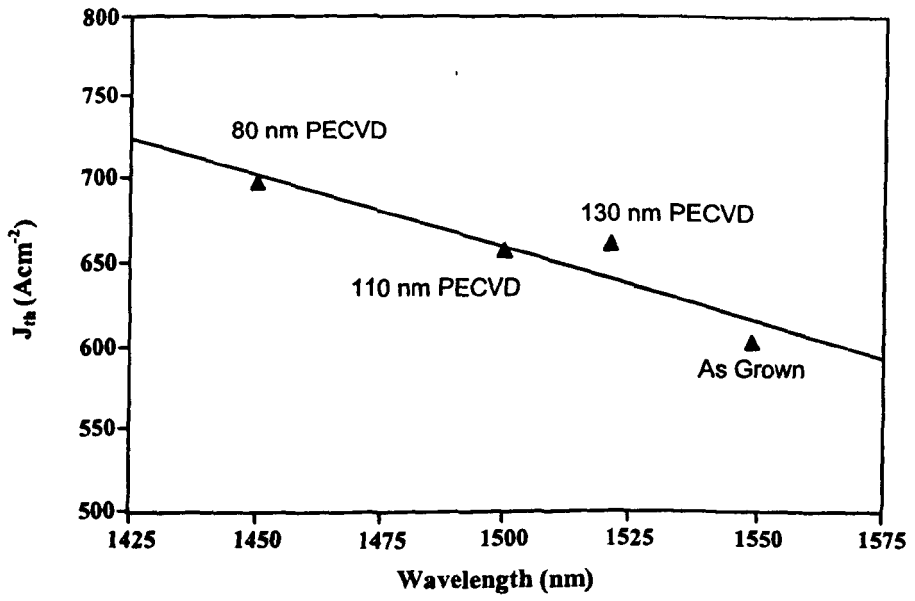
Fig. 6.3.1 (a) and (b) show the threshold current densities and internal quantum efficiencies of the InGaAs/AlInGaAs bandgap-tuned oxide stripe lasers. It can be seen that, for a laser wavelength shift as large as 100 nm, the threshold current density of the laser increases by only 16% compared to that of the as-grown laser. It is believed that the increase is mainly due to the well shape changing and the carriers becoming less confined within the wells. For the same bandgap shift, the internal quantum efficiency decreases by only ~4%, implying that the process does not introduce a significant number of nonradiative recombination centres [16].

The same assessment was also carried out on bandgap-tuned InGaAs/InGaAsP material. The material structure is shown in table 6.3.1.

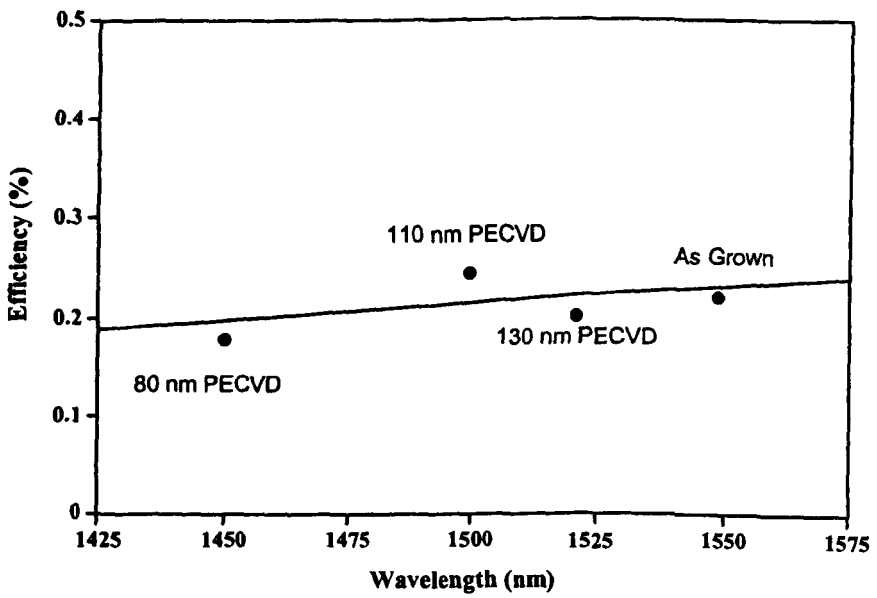
Table 6.3.1 Material structure used for making bandgap tuned lasers

Repeats	Thick. (nm)	Material	Dopant	Type	Conc(cm <sup>-3</sup> )
1	100	GaIn <sub>0.53</sub> As	Zn	p	3.0E+18
1	50	InGaAsP(1.18)	Zn	p	1.0E+18
1	1000	InP	Zn	p	5.0E+17
1	200	InP spacer		I	
1	80	InGaAsP (1.1)		I	
1	50	InGaAsP (1.18)		I	
5	12	InGaAsP (1.26)		I	
5	5.5	In <sub>0.53</sub> GaAs QW		I	
1	12	InGaAsP (1.26)		I	
1	50	InGaAsP (1.18)	Si	n	7.0E+17
1	80	InGaAsP (1.1)	Si	n	8.0E+17
1	900	InP	Si	n+	2.0E+18

It was found that, for a laser wavelength shift as large as 110 nm, the threshold current density of the laser increased by only 6% compared to that of the as-grown laser, while the internal quantum efficiency decreased by only ~3%.



(a)



(b)

Fig. 6.3.1 (a) Threshold current densities and (b) internal quantum efficiencies of the InGaAs/AlInGaAs bandgap-tuned oxide stripe lasers

Another issue of concern is the uniformity of the characteristics of the post-processed material. Although PL measurements are a good way to determine the size of the shift, they are not effective in determining other material characteristics, such as quantum efficiency, internal loss, etc. Here, the laser threshold current and slope efficiency are employed to indicate the uniformity of the sputtering process. Figure 6.3.2 shows the threshold currents and slope efficiencies of individual oxide stripe lasers on a bar of 600  $\mu\text{m}$  cavity length, which consisted of 15 individual devices separated by 340  $\mu\text{m}$ . Similar results were also found for different bars. Obviously, the uniformity of threshold currents and slope efficiencies is very good (within 10% variation), especially considering the deviation caused by cleaving process.

These results further demonstrate the usefulness of QWI techniques in monolithic integration. It has been previously demonstrated that electro-absorption modulators, bandgap-tuned using the sputtering process, retain a good switching response [17].

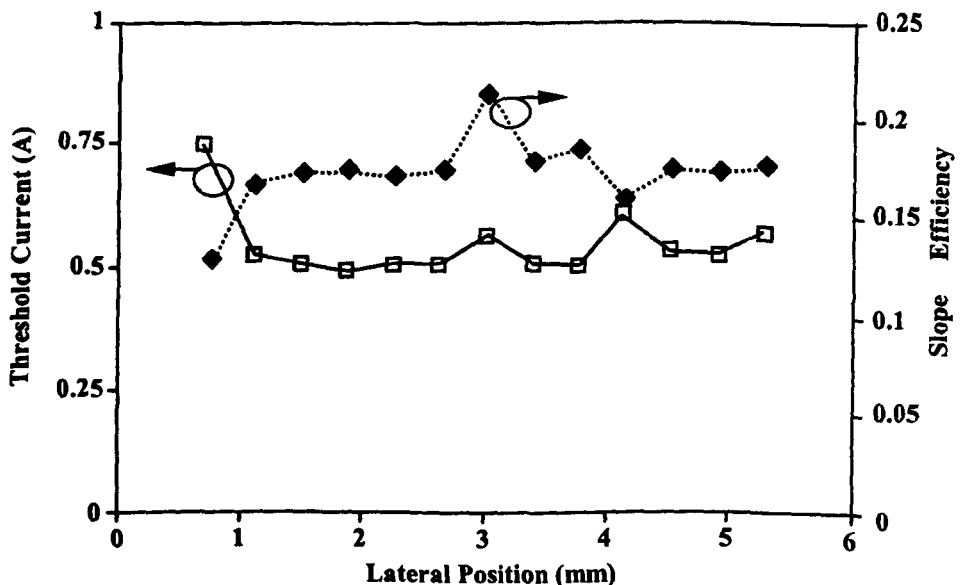


Fig 6.3.2 Uniformity of laser threshold current and slope efficiency

SIMS analysis was also carried out on some InGaAsP bandgap-tuned stripe laser (MR1287 MOCVD wafer, structure shown in Table 6.3.1). The experimental conditions are the same as shown in Table 6.2.2.

The laser diode did not show a well-resolved layer structure due to SIMS induced sample roughness arising when profiling through the metal contact layers. After removing the metal contact layers, a profile with good depth resolution was obtained (See Figure 6.3.3). It shows that the Cu concentration is lower than  $10^{17}$   $\text{cm}^{-3}$ , which is the machine resolution, in the core region.

Again, SIMS measurements on lasers with different bandgap shifts of 0.026 eV and 0.055 eV, which correspond to wavelength red shifts of 50 and 100 nm, show almost the same distributions of Cu through the structure. Considering the detail of the Cu concentration within the core region is not available due to instrumental detection limits, we assume Cu concentration within this region could be different for lasers with different bandgap shifts [15].

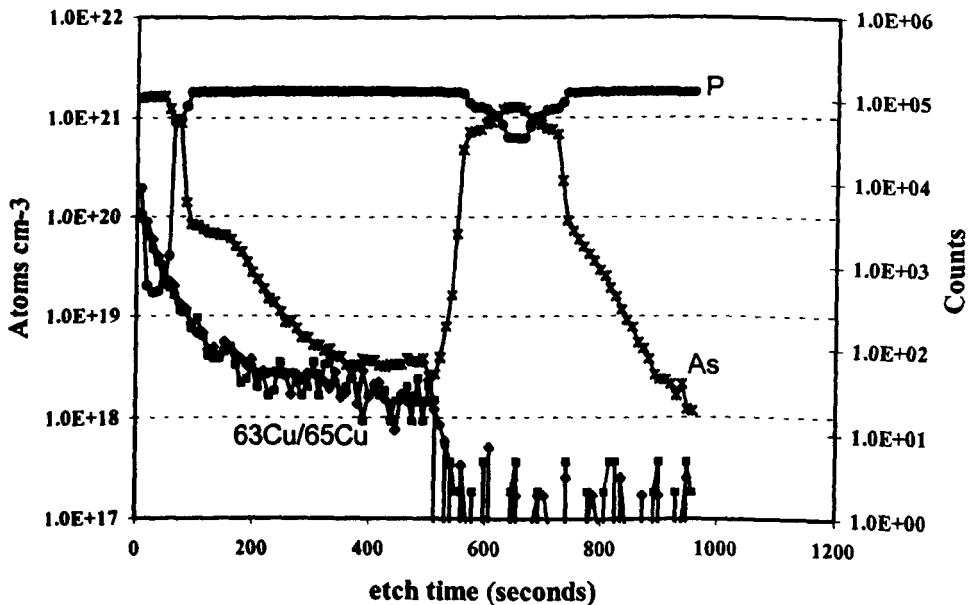


Fig 6.3.3 SIMS of a bandgap tuned InGaAsP laser

Comparing Figure 6.3.3 with Figure 5.4.4, an exciting fact is that the PECVD SiO<sub>2</sub> layer did reduce the diffusion of Cu into the core region and contributes to the low-internal-loss performance of the bandgap tuned lasers. This indicates one of the practical methods to form low loss waveguides in the future, using SID.

## **6.4 Applications of the novel multi-bandgap quantum well intermixing technique**

Several kinds of active components have been integrated on the same wafer with this novel multi-bandgap energy intermixing technique.

### **6.4.1 Integrated bandgap-tuned InGaAs/AlInGaAs and InGaAs/InGaAsP oxide stripe lasers and ridge waveguide lasers**

To demonstrate the great potential of this novel intermixing technique, several oxide stripe lasers with different bandgap energies were integrated on both InGaAs/AlInGaAs and InGaAs/ InGaAsP material with this technique.

Figure 6.4.1 gives the threshold current and slope efficiency characteristics of the four-wavelength integrated InGaAs/AlInGaAs bandgap-tuned oxide stripe lasers with cavity lengths of 400  $\mu\text{m}$ . It can be seen that, for a 100 nm blue shift in the lasing wavelength, there is only about 25% increase of threshold current.

Figure 6.4.2 shows the performance of a two-wavelength InGaAs/InGaAsP bandgap-tuned oxide stripe laser array fabricated in the same way. Significantly, there is only an 8% increase in threshold current for the bandgap-tuned laser for a wavelength blue shift of 110 nm.

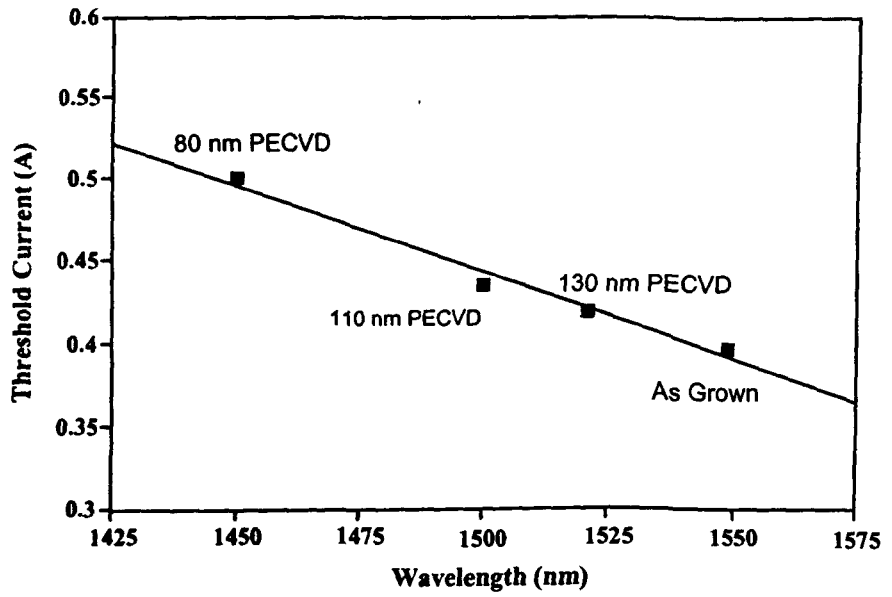
Apart from the bandgap tuned oxide stripe laser array, some integrated dual wavelength ridge waveguide lasers were also fabricated in InGaAs/AlInGaAs. In the fabrication, the PECVD SiO<sub>2</sub> protection layer was patterned so that its thickness was 110 nm on one of the two laser regions of the sample, while the other was 200 nm plus photoresist. After using the 20 nm sputtered SiO<sub>2</sub> process, the sample was annealed in an RTA at 650°C for 90 seconds. PL measurements showed that wavelength blue shift of the regions covered with 110 nm PECVD SiO<sub>2</sub> was 60 nm and that the other regions were completely suppressed. Then both the PECVD SiO<sub>2</sub> protection layer and sputtered cap were removed by HF so that a fresh 200 nm PECVD SiO<sub>2</sub> layer, which was used as dry etching mask material, could be deposited on the wafer surface.

5 μm wide ridge waveguide patterns, separated by 300 μm, were defined on both regions using photolithography and photoresist S1818. In the ion reactive etching processes, C<sub>2</sub>F<sub>6</sub> was employed to etch the 200 nm PECVD SiO<sub>2</sub> mask and CH<sub>4</sub>/H<sub>2</sub> for wafer etching. The etching time of InGaAs/AlInGaAs was about 22 minutes so that waveguides of 800 μm height could be obtained. Following the removal of the dry etching mask and a third 200 nm PECVD SiO<sub>2</sub> deposition, the sample was annealed at 530°C for 90 seconds to remove any residual damage generated during the dry etching process. The devices were completed by a p-contact

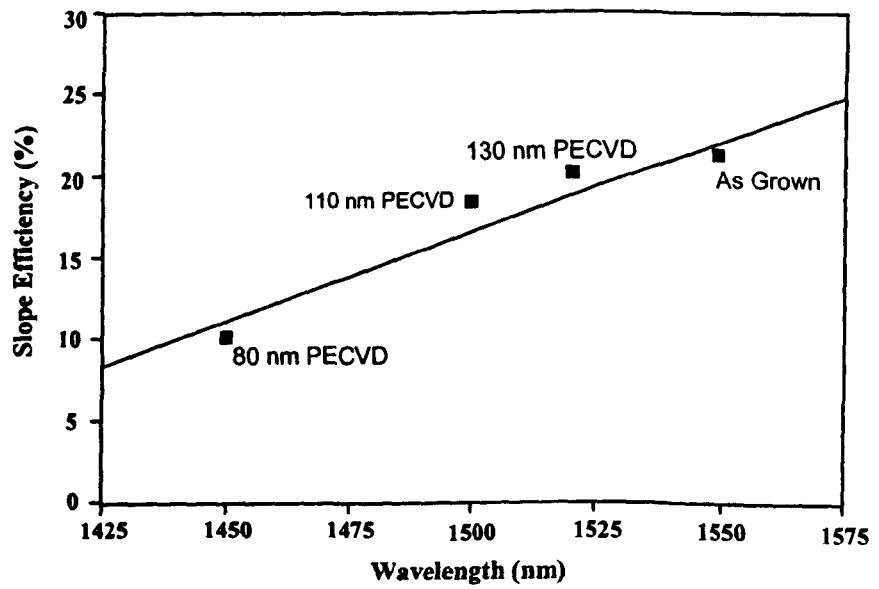
window opening, substrate thinning and metal contact evaporation. Finally, the lasers were cleaved to a 300  $\mu\text{m}$  cavity length and tested under pulsed conditions (400 ns pulse at a 1 kHz repetition rate).

Figure 6.4.3 shows the output characteristics of the integrated bandgap tuned ridge waveguide lasers. The lasing wavelengths are 1546 and 1503 nm. The threshold current of the 43 nm wavelength shifted laser increases by only 6 mA, compared to that of the as-grown laser (46 mA), while the slope efficiencies were very similar (12.1 and 12.8%) [18].

The bandgap-tuned oxide stripe laser arrays and ridge waveguide laser arrays are of limited practical application. But the results achieved here, for the first time, clearly demonstrate that light emitting sections with different operation wavelengths can be integrated at will with modulators and passive components with this simple, reliable multi-bandgap quantum well intermixing technique. The 100–110 nm emission wavelength range covers the equivalent of C band (1525–1565 nm) to L band (1570–1610 nm), which indicates that this technique could have wide application in WDM.

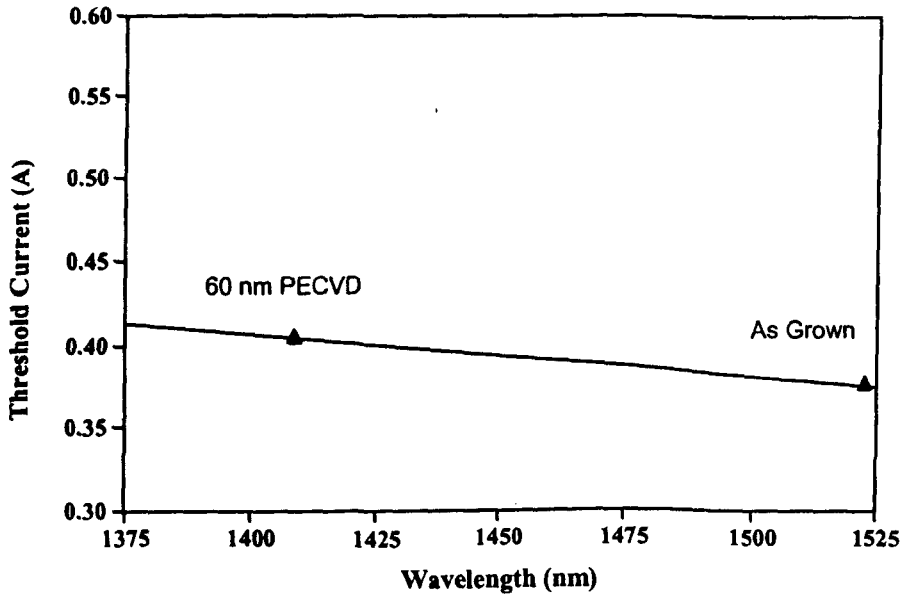


(a)

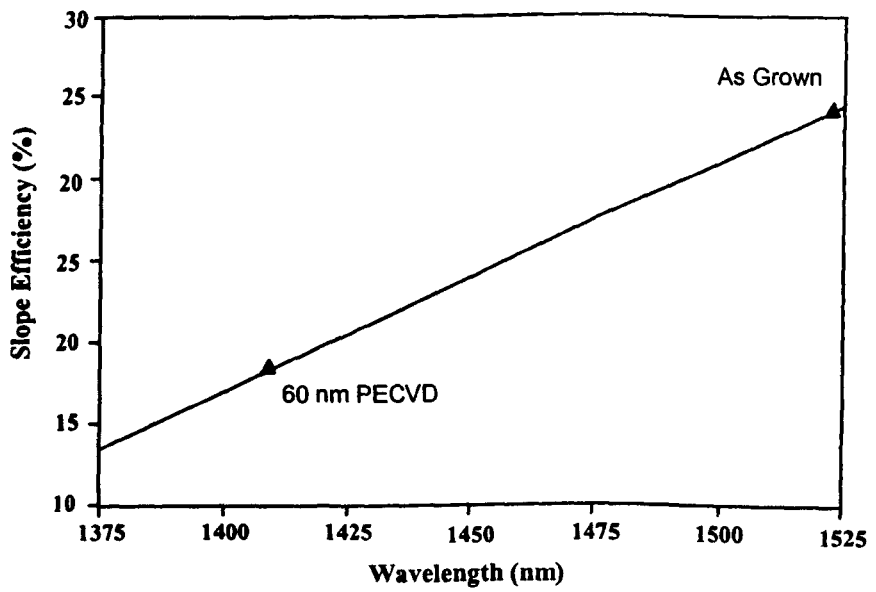


(b)

Fig. 6.4.1 (a) Threshold currents and (b) slope efficiencies of the InGaAs/AlInGaAs bandgap-tuned oxide stripe laser array

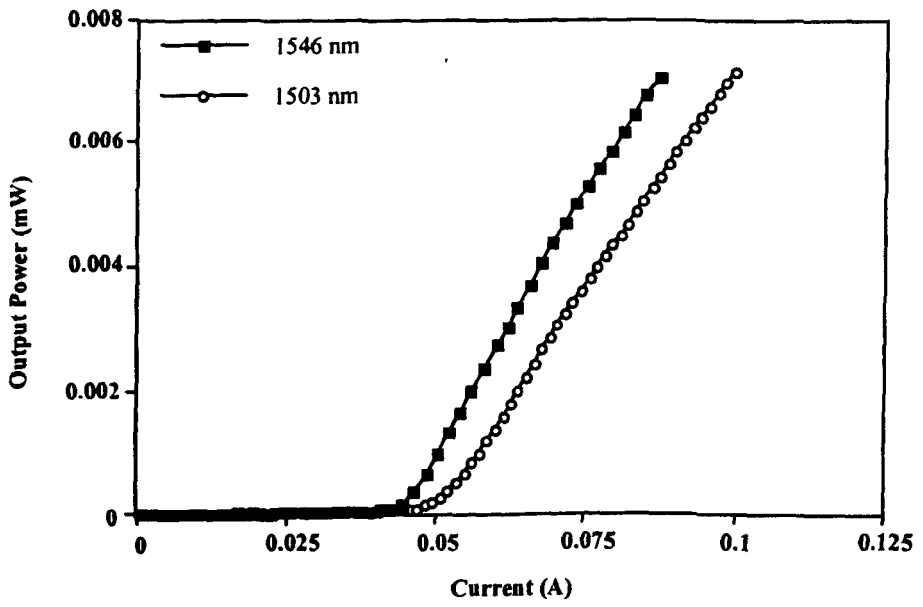


(a)

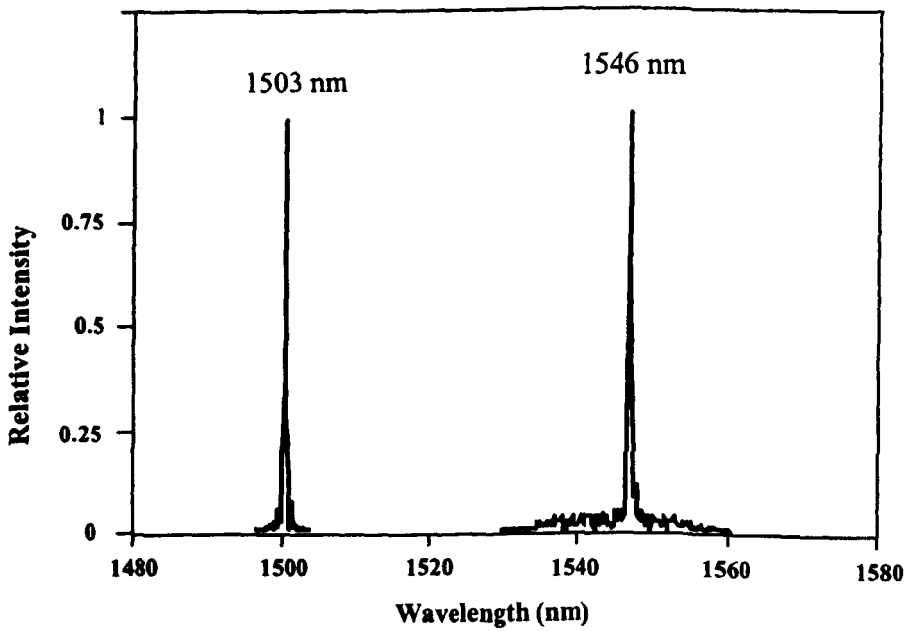


(b)

Fig. 6.4.2 (a) Threshold currents and (b) slope efficiencies of the InGaAs/InGaAsP bandgap-tuned oxide stripe laser array



(a)



(b)

Fig. 6.4.3 (a) Power-current characteristics and (b) optical spectra of integrated InGaAs/AlInGaAs ridge waveguide lasers

### 6.4.2 Integrated 2x2 crosspoint optical switch

The 2x2 crosspoint switch incorporates semiconductor optical amplifiers (SOA), passive waveguide splitters and electro-absorption (EA) modulators and typically requires three bandgaps (See 6.4.4). For many systems purposes, the operation wavelength for the switches, and therefore of the amplifiers, is 1.55  $\mu\text{m}$ , but a much wider bandgap is required for the passive waveguides in order to minimize the absorption of light propagating along the waveguides. Moreover, the optimum absorption bandgap for the EA modulators is 30-50 nm shorter than that for the amplifiers, to realize a low insertion loss while attaining a large extinction ratio.

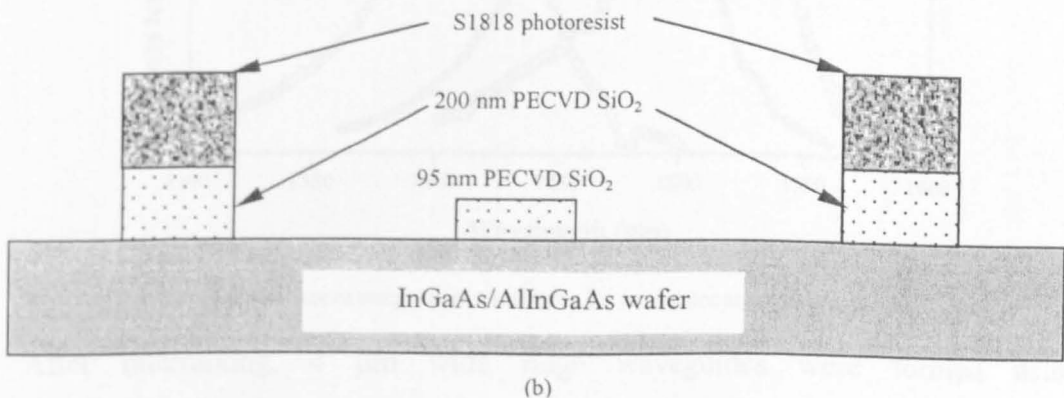
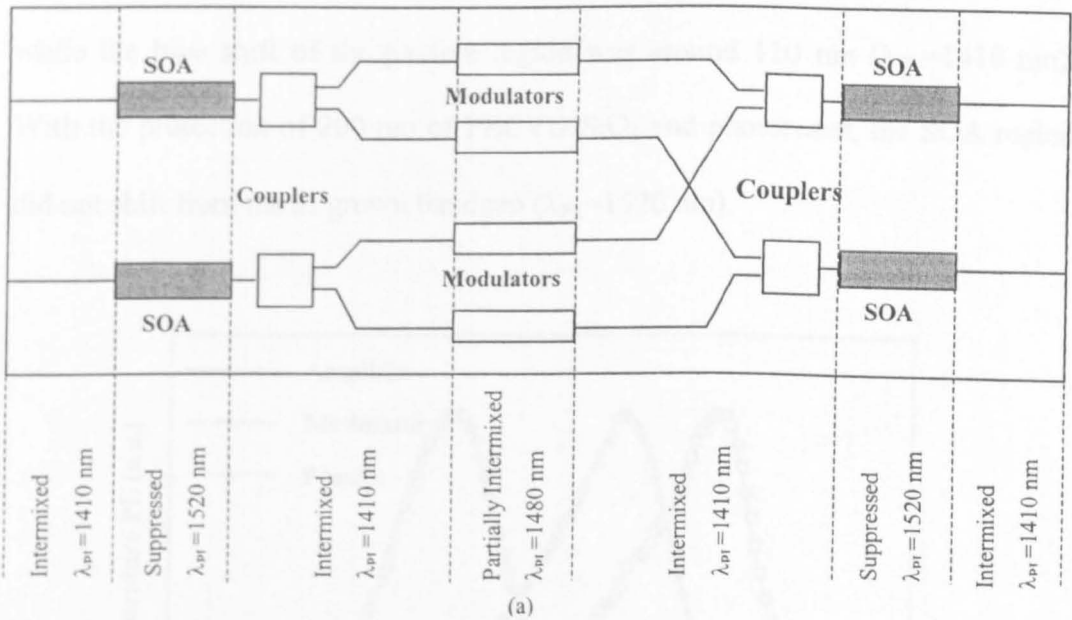


Fig. 6.4.4 (a) diagram of 2x2 crosspoint optical switch and (b) its masking way of QWI process

The wafer used for fabrication was a standard un-strained InGaAs/AlInGaAs MQW grown on a (100)-oriented n-type InP substrate by metal organic vapor phase epitaxy (MOVPE). The structure is shown in Table 2.2.1.

The intermixing process was similar to that described above. The PECVD SiO<sub>2</sub> cap layer was patterned such that the thicknesses were 200 (plus a layer of photoresist S1818), 95, and 0 nm on the SOA, EA modulator and passive region respectively. After the sputtering/annealing process, the room temperature photoluminescence (PL) was measured (See Figure 6.4.5). It was found that there was a wavelength blue shift of 40 nm in the modulator region ( $\lambda_{PL}=1480$  nm), while the blue shift of the passive region was around 110 nm ( $\lambda_{PL}=1410$  nm). With the protection of 200 nm of PECVD SiO<sub>2</sub> and photoresist, the SOA region did not shift from the as grown bandgap ( $\lambda_{PL}=1520$  nm).

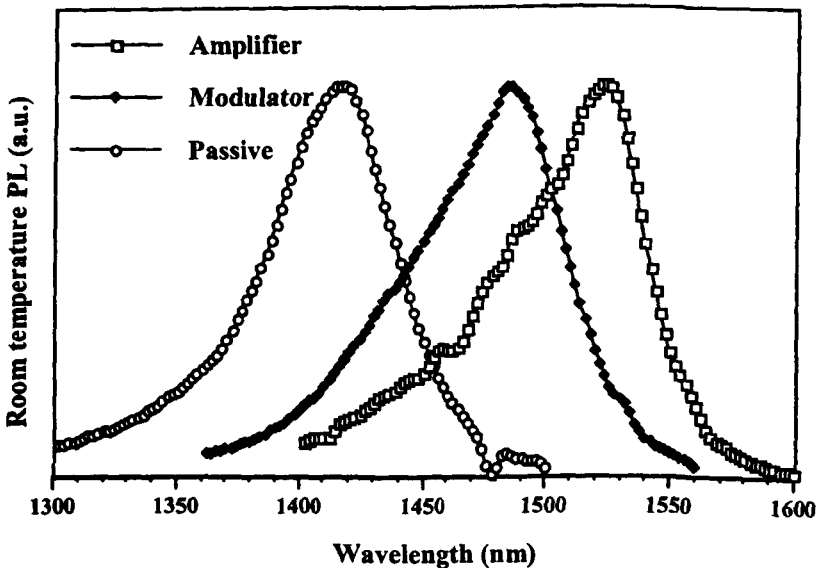


Fig.6.4.5 Room temperature PL spectra for modulator and passive regions

After intermixing, 4  $\mu\text{m}$  wide ridge waveguides were formed using photolithography and CH<sub>4</sub>/H<sub>2</sub> reactive ion etching to a depth of 1.2  $\mu\text{m}$ . Following

etching, samples were annealed at 500°C for 60 seconds to remove the residual damage generated during dry etching process. Then the same steps as for the ridge waveguide laser integration were carried out to complete the fabrication. It should be mentioned that the p-side contact was restricted to only the modulator and amplifier sections and, to ensure electrical isolation between these two components, the InGaAs cap layer of the surrounding area was removed by wet etching. Finally, individual devices were cleaved out and mounted onto a copper block with silver epoxy and wire bonding was applied.

During the test stage, a tunable semiconductor laser, with a range from 1480 to 1580 nm, was used to assess the device performance. Light from the laser was coupled into the device through a standard single mode fibre with a tapered lens end. A polarization controller was used to ensure that only the TE mode was launched in the waveguide. The output from the device was coupled into a fibre and then to an optical spectrum analyzer to monitor the power.

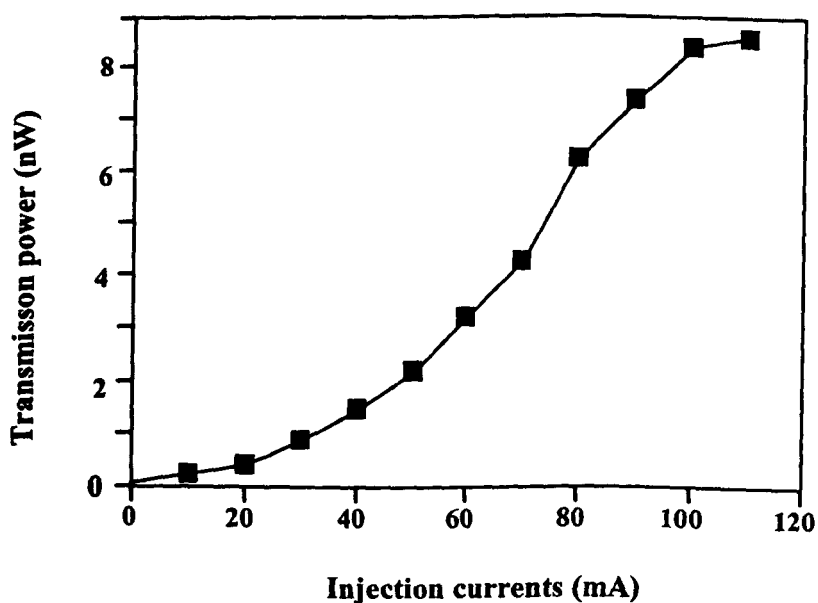


Figure 6.4.6 Transmission power as function of injection currents of amplifiers

Figure 6.4.6 shows the transmitted power as function of amplifier injection current measured at a wavelength of 1540 nm. The amplifier injection currents were set to be equal for amplifiers in a particular waveguide route. The measured net gain was around 5-6 dB per amplifier at an injection current of 110 mA.

A reverse DC voltage bias was applied to the EA modulators, which could be adjusted from 0 to 5.0V. It can be seen from Figure 6.4.7 that a modulation depth of 25 dB was obtained at an operation wavelength of 1500 nm and 17 dB at 1520 nm, which indicates the sputtering process did not produce any dramatic degradation in the performance of the MQW structure as an EA modulator [19-20].

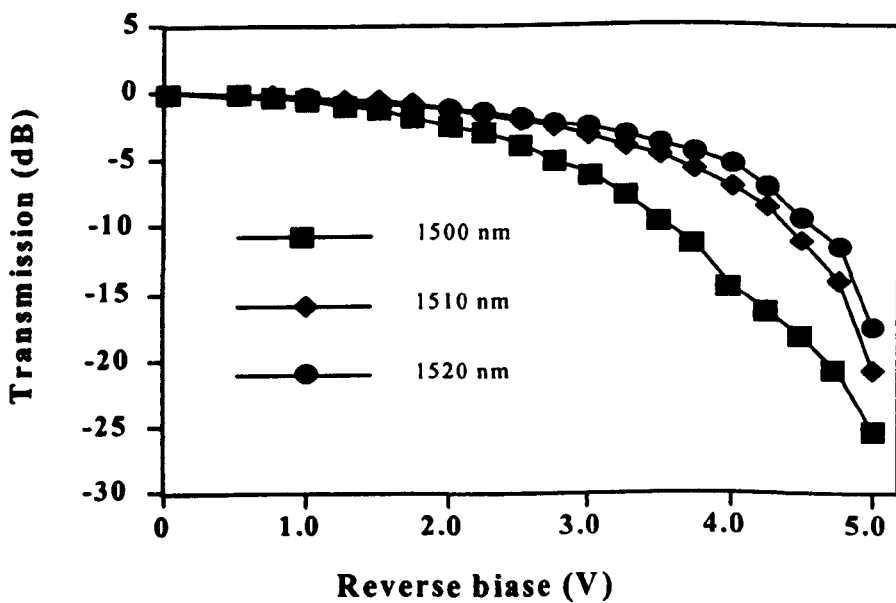


Figure 6.4.7 Transmitted optical power as function of reverse bias voltage for the EA modulator

## 6.5 Summary

In this Chapter, an important and potentially powerful development of the sputtering technique to create multiple bandgaps in a single sputtering-annealing step has been discussed for the first time. The technique is simple, reliable and the tuning of the bandgap is precise. With this technique, the blue shift in the bandgaps can be precisely tuned over a range of 0-160 nm for the InGaAs/AlInGaAs and 0-100 nm for InGaAs/InGaAsP MQW material systems. Assessment of post-process material characteristics has shown that good electrical and optical qualities have been maintained in the bandgap widened regions.

Several kinds of active devices, such as bandgap tuned stripe lasers, bandgap tuned ridge waveguide lasers and a 2x2 crosspoint optical integrated switch were successfully integrated on the same wafer using this novel multi-bandgap quantum well intermixing technique.

## Reference

- [1] B.C. Qiu, Y.H. Qian, O.P. Kowalski, A.C. Bryce, J.S. Aitchison, R.M. De La Rue, J.H. Marsh, M. Owen, I.H. White, R.V. Penty, A. Franzen, D.K. Hunter, I. Andonovic, 'Fabrication of 2x2 crosspoint switches using a sputtered SiO<sub>2</sub> intermixing technique', *Photonics Technology Letters*, Vol.12, pp.287-289, 2000
- [2] J.E. Epler D.W. Treat, S.E. Nelson, and T.L. Paoli, 'Multiple wavelength diode laser super array', *IEEE J. of Quantum Electronics*, Vol.26, pp.663-668, 1990
- [3] K.J. Beermink, R.L. Thorton, and H.F. Chung, 'Low threshold current dual wavelength planar buried heterostructure lasers with close spatial and large spectral separation', *Applied Physics Letter*, Vol.64, pp.1082-1084, 1994
- [4] D. Jacob, N.H. Tran, F. Bretenaker, and A. LeFloch, 'Differential absorption measurement of methane with two spectrally resolved laser lines', *Applied Optics*, Vol.33, pp.3261-3264, 1994
- [5] S.D. McDougall, M.J. Jubber, O.P. Kowalski, J.H. Marsh, and J.S. Aitchison, 'GaAs/AlGaAs waveguide p-i-n photodiodes with non-absorbing input facets fabricated by quantum well intermixing', *Electronics Letter*, Vol.36, pp.749-750, 2000
- [6] T.M. Cockerill, R.M. Lammert, D.V. Forbes, M.L. Osowski, and J.J. Coleman, 'Twelve-channel strained-layer InGaAs-GaAs-AlGaAs buried heterostructure quantum well laser array for WDM applications by selective-area MOCVD', *IEEE Photonics Technology Letter*, Vol.6, pp.786-788, 1994
- [7] B.S. Ooi, M.W. Street, S.G. Ayling, A.C. Bryce, J.H. Marsh, J.S. Roberts, 'The application of the selective intermixing in selected area (SISA) technique to

the fabrication of photonic devices in GaAs/AlGaAs structure', *International Journal of Optoelectronics*, Vol.10, pp.257-263, 1996

[8] J.P. Noel, D. Melville, T. Jones, F.R. Shepherd, C.J. Miner, N. Puetz, K. Fox, P.J. Poole, Y. Feng, E.S. Koteles, S. Charbonneau, R.D. Goldberg, I.V. Mitchell, 'High-reliability blue-shifted InGaAsP/InP lasers', *Applied Physics Letter*, Vol.69, pp.3516-3518, 1996

[9] A. McKee, C.J. Mclean, G. Lullo, A.C. Bryce, R.M. De La Rue, J.H. Marsh and C.C. Button, 'Monolithic integration in InGaAs-InGaAsP multiple quantum well structure using laser intermixing', *IEEE J of Quantum Electronics*, Vol.33, pp.45-55, 1997

[10] O.P. Kowalski, C.J. Hamilton, S.D. McDougall, J.H. Marsh, A.C. Bryce, R.M. De La Rue, B. Vögele, C.R. Stanley, C.C. Button, J.S. Aitchison, 'A universal damage induced technique for quantum well intermixing', *Applied Physics Letter*, Vol.72, pp.581-583, 1998

[11] S.D. McDougall, O.P. Kowalski, C.J. Hamilton, F. Camacho, B.C. Qiu, M.L. Ke, R.M. De La Rue, A.C. Bryce, J.H. Marsh, 'Monolithic integration via a universal damage enhanced quantum-well intermixing technique', *IEEE J. of Selected Topics In Quantum Electronics*, Vol.4, pp.636-646, 1998

[12] Y.H. Qian, M.Owen, M.L. Ke, B.C. Qiu, S.D. McDougall, O.P. Kowalski, C.J. Hamilton, A.C. Bryce, J.H. Marsh, C.D.W. Wilkinson, R.V. Penty, I.H. White, S. Perrin, and D. Rogers, 'Three band-gap QW intermixing in InP/InGaAs/InGaAsP system for monolithically integrated optical switch', *11<sup>th</sup> IEEE Annual Lasers and Electro Optics Society (LEOS) Meeting Proceedings*, pp.194-195, 1998

- [13] B.C. Qiu, Y.H. Qian, O.P. Kowalski, A.C. Bryce, J.S. Aitchison, R.M. De La Rue, J.H. Marsh, M. Owen, I.H. White, R. V. Penty, A. Franzen, D.K. Hunter, and I. Andonovic, 'Low cost fabrication of 2x2 crosspoint', *Proceeding of ECOC'99*, Vol.I, pp.122-123, 1999
- [14] B.C. Qiu, X.F. Liu, O.P. Kowalski, A.C. Bryce, J.H. Marsh, 'Precise Control of the Blue-shift of the Wavelength in InGaAs-InGaAsP Multiple Quantum Wells Using a Sputtered SiO<sub>2</sub> Technique', *12<sup>th</sup> IEEE Annual Lasers and Electro Optics Society (LEOS) Meeting Proceedings*, Vol.1, TuV3, pp. 309-310, 1999
- [15] 'SIMS analysis of III-V materials', *Test report of No.SI.IPL.1243*, Loughborough Surface Analysis Limited, July, 2001
- [16] X.F. Liu, B.C. Qiu, M.L. Ke, A.C. Bryce, J.H. Marsh, 'Control of Multiple Bandgap Shifts in InGaAs/AlInGaAs Multiple Quantum Well Material Using Different Thickness of PECVD SiO<sub>2</sub> Protection Layers', *IEEE Photonics Technology Letters*, Vol.12, No.9, pp.1141-1143, 2000
- [17] B.C. Qiu, Y.H. Qian, O.P. Kowalski, A.C. Bryce, J.S. Aitchison, R.M. De La Rue, J.H. Marsh, M. Owen, I.H. White, R. V. Penty, A. Franzen, D.K. Hunter, and I. Andonovic, 'Fabrication of 2x2 crosspoint switches using a sputtered SiO<sub>2</sub> intermixing technique', *IEEE Photonics Technology Letters*, Vol.12, pp.287-289, 2000
- [18] X.F. Liu, B.C. Qiu, M.L. Ke, A.C. Bryce, J.H. Marsh, 'The Application of a novel intermixing technique for multi-bandgap integration of InGaAs/AlInGaAs', *13<sup>th</sup> IEEE Annual Lasers and Electro Optics Society (LEOS) Meeting Proceedings*, THR4, 2000
- [19] B.C. Qiu, X.F. Liu, M.L. Ke, H.K. Lee, A.C. Bryce, J.S. Aitchison, and J.H. Marsh, 'Monolithic fabrication of 2x2 crosspoint switches on InGaAs/AlInGaAs

multiple quantum well structure using quantum well intermixing', *Conference on Lasers and Electro-Optics (CLEO) Proceedings, CMI4, 2001*

[20] B.C. Qiu, X.F. Liu, M.L. Ke, H.K. Lee, A.C. Bryce, J.S. Aitchison, and J.H. Marsh, 'Monolithic fabrication of 2×2 crosspoint switches on InGaAs/AlInGaAs multiple quantum well structure using quantum well intermixing', to be published in *IEEE Photonics Technology Letters*, December, 2001

## CHAPTER 7

# MONOLITHICALLY INTEGRATED MACH-ZEHNDER ASYMMETRIC INTERFEROMETER DEMULTIPLEXER: INTRODUCTION AND THEORY

High-bandwidth demultiplexing is important for optical time-division multiplexed communication systems, as demultiplexing is the major factor limiting the throughput of complete system. In this chapter, a brief introduction to high-speed demultiplexers is presented. The principle of terahertz optical asymmetric demultiplexer is investigated. The design of a Mach-Zehnder interferometer (MZI) type demultiplexer is discussed.

## 7.1 Introduction

For optical time-division multiplexed communication systems, high-bandwidth demultiplexing is important. That is because the demultiplexer is the only component, which must operate at the aggregate bandwidth of the multiplexing system. It limits the throughput of the complete system.

There have been several candidates for ultrafast demultiplexing, such as soliton gates [1] and Nonlinear Optical Loop Mirrors (NOLM's) [2]-[5]. Soliton gates require tens of meters of special fibre, expensive soliton sources and high energy control pulses (~100 pJ). A NOLM uses a small Kerr-type nonlinearity in the optical fibre to achieve a phase shift, so it requires either a long length of fibre to obtain enough phase shift or a high-intensity control pulse to achieve a large optical nonlinearity.

Latterly, an improved NOLM, the Semiconductor Laser Amplifier in a Loop Mirror (SLALOM), was developed [6]-[7]. The SLALOM employs a semiconductor optical amplifier (SOA), which has a much stronger nonlinearity than that of silica fibres, as the nonlinear optical element and to achieve a phase shift. But as the gain-saturation-induced phase shift is governed by signal itself, the interval between two successive pulses has to be larger than the recovery time of the amplifier. This means the time resolution of a SLALOM is determined by the relatively slow recovery time of the amplifier (~10<sup>2</sup> ps), which limits its application in ultrahigh speed switching.

In 1993, a novel ultrafast all-optical demultiplexer, the Terahertz Optical Asymmetric Demultiplexer (TOAD), was demonstrated [8]-[9] for the first time by J.P. Sokoloff et al. Similar to the SLALOM, the TOAD also uses gain-saturation of a SOA to achieve a phase shift. But unlike the SLALOM, the phase shift of a TOAD is governed by the control pulse and offset position of the amplifier in the loop mirror. The time resolution of a TOAD is therefore determined by the rise-time of the nonlinearity of the SOA, which is more than two orders of magnitude faster than that of a SLALOM implying, THz demultiplexing can be achieved with a TOAD.

Apart from its ultra-high speed switching, the TOAD has some other advantages such as low switching energies ( $< \text{pJ}$ ), wavelength compatibility, compact and stable structure, easy integration.

With these significant features, the TOAD can be employed as a demultiplexer in an OTDM system [10-13], an add/drop multiplexer (ADM) for a multi-node architecture [14] and for all-optical address recognition and self-routing in a packet-switching network [15], etc.

In 1994, K. Suzuki et al. demonstrated a significant achievement using a TOAD. An optically multiplexed signal of 160 Gbit/s was successfully demultiplexed to 10 Gbit/s with 500 fJ control pulses [11]. In this letter, a low Bit Error Rate (BER) was demonstrated for the first time. Experiment confirms that 'the BER is degraded by the excess signal power in the optical loop mirror, which introduces the temporal change of the carrier density in the SOA, that degrades the eye

opening'. By restricting the average signal power into the demultiplexer to 0 dBm, error-free operation ( $BER < 10^{-10}$ ) was achieved.

In the same year, the demonstration of a 250 Gbit/s TOAD, constructed using discrete elements was reported by I. Glerk [16]. Pulses of only 800 fJ were used to gate the demultiplexer.

In 1995, K.I. Kang et al. demonstrated a TOAD based on a Mach-Zehnder interferometer structure. 100 Gbit/s demultiplexing was realized requiring control pulses of only 650 fJ [12,13].

In 1996, E. Jahn et al. reported, for the first time, the operation of a 20 Gbit/s all optical add/drop multiplexer that could be configured in a highly flexible multi-node architecture [14].

Recently, major effort has been focused on the integration of TOADs [14][17][18]. In 1995, E. Jahn demonstrated a 40 Gbit/s monolithically integrated device fabricated with selective epitaxy technology [17]. In this device, a MZI structure was used with two 500  $\mu\text{m}$  SOAs. MMI couplers were employed as 3dB couplers owing to their compact size and low polarisation sensitivity. Moreover, the input/output waveguides were inclined at  $7^\circ$  to the cleaved facet to reduce the reflectivity. Using this integrated device, a 5 Gbit/s signal was demultiplexed from a 40 Gbit/s stream and a power penalty of 2.5 dB at a BER of  $10^{-9}$  was obtained.

From the viewpoint of demand of realistic systems, only monolithically integrated devices can be employed because of their stability and high performance. Therefore in this work, an all-optical monolithically integrated TOAD was developed, in which the semiconductor optical amplifier, multimode interference (MMI) couplers and waveguides were monolithically integrated.

## 7.2 Nonlinearity in Semiconductor Optical Amplifier (SOA)

### 7.2.1 Carrier density change induced nonlinearity

Consider an optical beam incident to a semiconductor laser amplifier. The incident beam is amplified and if the beam is sufficiently intense, gain saturation will occur since there is a limited number of conduction band states and carriers that can participate in transitions to give optical gain. From the steady-state rate equations for electrons and photons, a simple analytical description of the saturation of the gain can be obtained. Assuming the recombination process is characterised by a lifetime  $\tau$ , then we have [19]

$$\frac{g_0}{g} = 1 + \frac{p}{p_s} \quad (7.2.1)$$

$g_0$  and  $g$  denote the unsaturated and saturated gain coefficients per unit length.  $p$  is the incident optical power and  $p_s$  is the saturation power given by

$$P_s = \frac{E \cdot S}{\Gamma \tau \cdot \left( \frac{dg}{dN} \right)} \quad (7.2.2)$$

$E$  is the photon energy;  $S$  is the waveguide section area;  $\Gamma$  is the mode confinement factor;  $dg/dN$  is the differential gain and  $N$  is the electron concentration in the semiconductor.

Manipulation of the steady-state rate equations gives the following result for the effective index  $n$  [20]:

$$n = n_0 - g_0 \left( \frac{dn/dN}{dg/dN} \right) \frac{P/P_s}{1 + P/P_s} \quad (7.2.3)$$

$n_0$  is the refractive index in the absence of light and  $dn/dN$  is the derivative of the index with respect to carrier density.

Then we can get the nonlinear phase shift caused by carrier density change:

$$\Delta\Phi_{Carrier} = \frac{2\pi}{\lambda_0} \left( -g_0 \left( \frac{dn/dN}{dg/dN} \right) \frac{P/P_s}{1 + P/P_s} \right) \cdot l \quad (7.2.4)$$

$l$  is the length of SOA;  $\lambda_0$  is the free-space wavelength.

Typical values for an optical amplifier of InGaAs/InGaAsP working at 1.55 $\mu$ m are,

$$E = 1.28 \times 10^{-19} \text{ J}, S = 0.3 \text{ } \mu\text{m}^2, \Gamma = 0.3, dg/dN = 2.8 \times 10^{-16} \text{ cm}^2, \tau = 0.35 \text{ ns},$$

$$dn/dN = -2 \times 10^{-20} \text{ cm}^3, g_0 = 300 \text{ cm}^{-1}.$$

From (7.2.2), we find  $p_s = 13 \text{ mW}$ , and from (7.2.4), a phase shift of  $\pi$  should be achieved for  $p/p_s = 0.099$  in a device of  $400 \mu\text{m}$  length. This means an incident optical power of only  $1.29 \text{ mW}$  is needed for the InGaAs/InGaAsP amplifier.

Similarly, for an InGaAs/AlInGaAs amplifier of same bandgap wavelength and waveguide structure, we can show an incident optical power of  $3 \text{ mW}$  is large enough to achieve a  $\pi$  phase shift, with typical values of [21]

$$dg/dN = 3.2 \times 10^{-16} \text{ cm}^2, dn/dN = -2 \times 10^{-20} \text{ cm}^3, g_0 = 300 \text{ cm}^{-1}, \tau = 0.15 \text{ ns}, p_s = 26 \text{ mW}$$

### 7.2.2 Kerr Effect

With a high intensity field, some nonlinearities will be present in a medium. One of them is the Kerr Effect:

$$n = n_0 + n_2 I \tag{7.2.5}$$

Here,  $n_0$  is the refractive index in absence of light (so-called linear refractive index) and  $n_2$  is the nonlinear refractive index that is termed the Kerr Coefficient.  $I$  is the optical intensity. The nonlinear phase shift related to the Kerr Effect is given by

$$\Delta\Phi_{Kerr} = \frac{2n_2\pi}{\lambda_0} I \cdot l \quad (7.2.6)$$

$l$  is the length of the SOA,  $\lambda_0$  is the free-space wavelength.

Typically, for the InGaAs/InGaAsP system,  $n_2$  is around  $-0.8\sim-2.0\times 10^{-16} \text{ m}^2/\text{W}$  according to different testing conditions [22]. With same waveguide structure ( $S = 0.3 \text{ }\mu\text{m}^2$ ,  $\Gamma = 0.3$ ), we can show the incident power needs to be larger than 10 W to achieve a phase shift of  $\pi$ .

Comparing this switching power with that of carrier density induced nonlinearity (1.29 mW), we conclude that the carrier density change induced nonlinearity is the dominating nonlinear process in SOA-based demultiplexers. It is unnecessary to take account of the Kerr Effect.

Although, no exact  $n_2$  can be given to the InGaAs/AlInGaAs material system, it is reasonable to estimate that it is of the same order as that of the InGaAs/InGaAsP material system. So in this work, only the nonlinearity induced by carrier density changes is under consideration.

### 7.3 Operation of TOAD

In OTDM systems, a group of users multiplex their signals onto a single optical fibre. Each transmitter is assigned one time-slot  $T_{bit}$  within a data frame period  $T_{frame}$ . Thus each user's data rate is equal to  $1/T_{frame}$ , and the aggregate data rate is equal to  $1/T_{bit}$ . To receive data from a particular transmitter, a receiver requires a demultiplexing switch to sample the appropriate time slot in each data frame. The demultiplexing switch must have sufficient bandwidth to permit sampling of data in a time slot of duration  $T_{bit}$ , and must perform a sampling operation every  $T_{frame}$ .

Normally, a TOAD consists of a interferometer, an additional coupler and one or two nonlinear elements offset from the loop's midpoint by a distance  $\Delta x$ . Up to now, two main structures have been demonstrated: Mach-Zehnder Interferometers (MZI) and Nonlinear Sagnac Interferometers (NSI), as shown in Fig.7.3.1. Although the structures are very different, the principles are the same.

Before we start to analyse the performance of TOAD, let us consider the working principles of the x coupler and the interferometers.

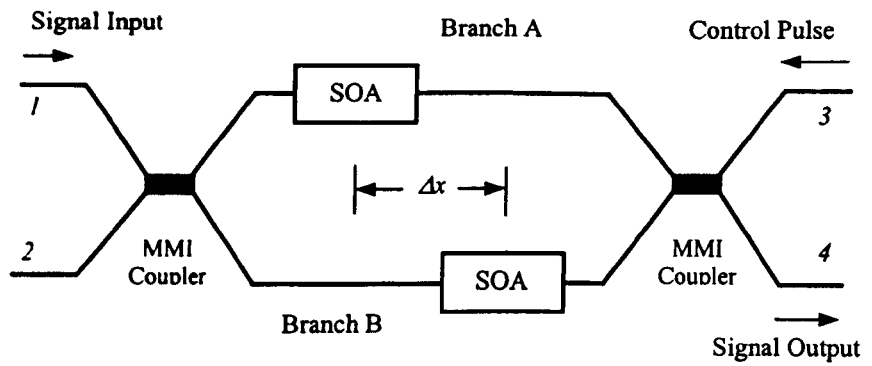


Fig. 7.3.1 (a) Scheme of MZI De-multiplexer

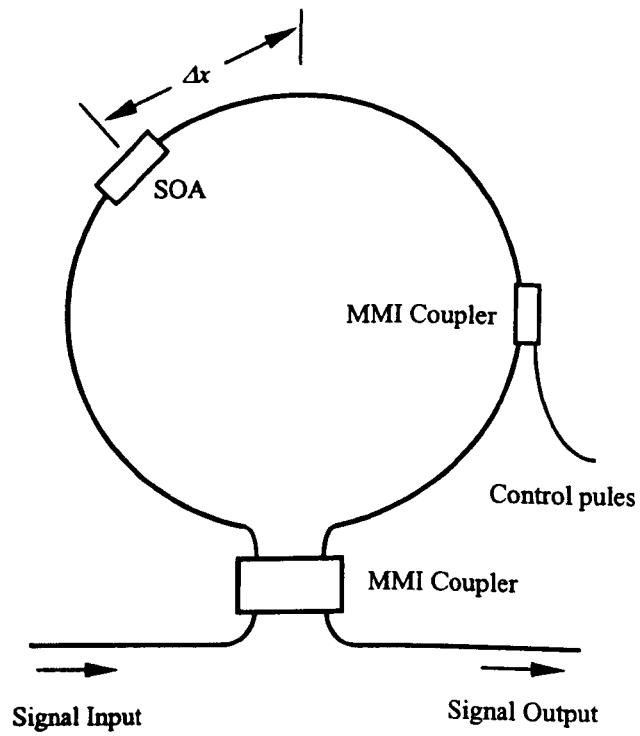


Fig. 7.3.1 (b) Scheme of NSI De-multiplexer

### 7.3.1 X-couplers

The X-coupler is a two-waveguide four-port coupler as shown in Figure 7.3.2, which is the guided wave equivalent of the free-space optics beam splitter. It plays a very important role in two-dimensional monolithic integration. The operation of X-couplers is based on the fact that, when two waveguides are brought sufficiently close to each other, the guiding modes in the two waveguides become coupled through their evanescent fields. This results in a reciprocal power transfer from one waveguide to the other, with a power transfer ratio depending on the waveguide spacing and interaction length.

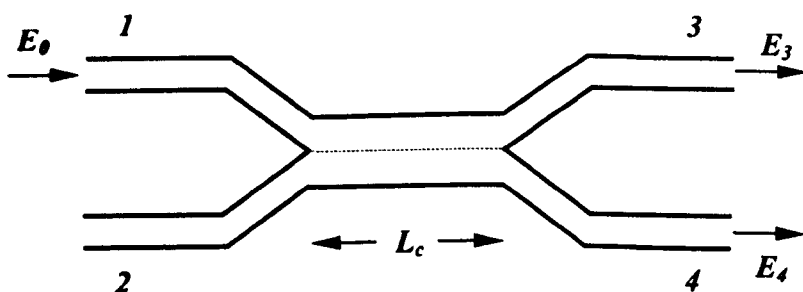


Figure 7.3.2 Diagram of the X-coupler

According to the coupled-mode theory [23], if an input beam with electrical field  $E_0$  is launched into port 1, the output fields from port 3 and port 4,  $E_3$  (in term of the transmitted mode) and  $E_4$  (in term of the coupled mode), are, omitting the time variation  $\exp(j\omega t)$ ,

$$E_3 = E_0 \cos(CL_c) \quad (7.3.1)$$

$$E_4 = E_0 \sin(CL_c) \cdot \exp[-j\frac{\pi}{2}] \quad (7.3.2)$$

$C$  is the coupling strength coefficient;  $L_c$  the effective coupling length. (7.3.1) and (7.3.2) show that the electrical field of the coupled mode has a  $\pi/2$  phase delay, compared to that of transmitted mode. Assuming there is no propagation loss, the intensities of transmitted mode and coupled mode are given by

$$I_3 = E_3 E_3^* = E_0^2 \cos^2(C \cdot L_c) \quad (7.3.3)$$

$$I_4 = E_4 E_4^* = E_0^2 \sin^2(C \cdot L_c) \quad (7.3.4)$$

The intensity split ratio of a X-coupler is defined as

$$r = \frac{I_3}{I_4} = \frac{\cos^2(C \cdot L_c)}{\sin^2(C \cdot L_c)} \quad (7.3.5)$$

Then, we can obtain

$$\cos(CL_c) = \sqrt{\frac{r}{1+r}} \quad (7.3.6a)$$

$$\sin(CL_c) = \sqrt{\frac{1}{1+r}} \quad (7.3.6b)$$

### 7.3.2 Performances of Mach-Zehnder interferometer (MZI) and Sagnac interferometer (SI)

The Mach-Zehnder interferometer consists of two X-couplers and two arms (shown in Figure 7.3.3). We assume the polarisation of signals is the same and maintained in the whole device.

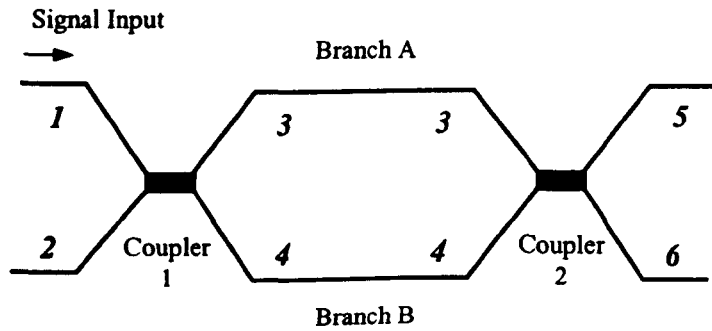


Figure 7.3.3 diagram of the Mach-Zehnder interferometer

When the input electrical field  $E_0$  is launched into port 1, the output electrical fields from port 3 ( $E_3$ ) and port 4 ( $E_4$ ) are given by (7.3.1) and (7.3.2). If the phase shifts and the field propagation losses in branches A and B are  $\Phi_i$  and  $K_i$  ( $i= A, B$ ), the electrical field output from port 5 is given by

$$E_5 = E_3 K_A \exp[-j\Phi_A] \cos(C_2 L_{c2}) + E_4 K_B \exp[-j\Phi_B] \sin(C_2 L_{c2}) \exp[-j\frac{\pi}{2}] \quad (7.3.7)$$

$$E_5 = E_0 K_A \cos(C_1 \cdot L_{c1}) \cos(C_2 \cdot L_{c2}) \exp[-j\Phi_A] - E_0 K_B \sin(C_1 L_{c1}) \sin(C_2 L_{c2}) \exp[-j\Phi_B] \quad (7.3.8)$$

Similarly, the electrical field from port 6 is

$$E_6 = E_3 K_A \exp[-j\Phi_A] \sin(C_2 L_{c2}) \exp[-j\frac{\pi}{2}] + E_4 K_B \exp[-j\Phi_B] \cos(C_2 L_{c2}) \quad (7.3.9)$$

$$E_6 = E_0 K_A \cos(C_1 \cdot L_{c1}) \sin(C_2 \cdot L_{c2}) \exp[-j\frac{\pi}{2}] \exp[-j\Phi_A] \\ + E_0 K_B \sin(C_1 L_{c1}) \cos(C_2 L_{c2}) \exp[-j\frac{\pi}{2}] \exp[-j\Phi_B] \quad (7.3.10)$$

To obtain a clear understanding of the performance of Mach-Zehnder interferometer, let us consider the simplest situation in which both the phase shifts and the propagation loss of the two branches are the same, as well as the split ratio  $r$  of 50:50 for the two X-couplers. From (7.3.6), we get

$$\cos(CL_c) = \sin(CL_c) = \frac{1}{2}\sqrt{2} \quad (7.3.11)$$

and

$$I_5 = 0 \quad (7.3.12a)$$

$$I_6 = E_0^2 K^2 \quad (7.3.12b)$$

which means, for such a Mach-Zehnder interferometer, all the signals launched into port 1 are output from port 6, while there is no output from port 5. However, for any of the three cases listed below, there may be an output from port 5, according to (7.3.8),

1. Split ratio of the X-couplers is not 50:50;
2. Propagation losses of the two branches are not the same;

3. Phase shifts of the two branches are not the same.

Compared with the Mach-Zehnder interferometer, the Sagnac interferometer is simpler, as it consists of only one X-coupler and a loop mirror (shown in Figure 7.3.4). We assume the polarisation of signals is the same and maintained in the whole device while the phase shifts and the field propagation losses in the clockwise (CW) direction and counter-clockwise directions (CCW) are  $\Phi_i$  and  $K_i$  ( $i= CW, CCW$ ).

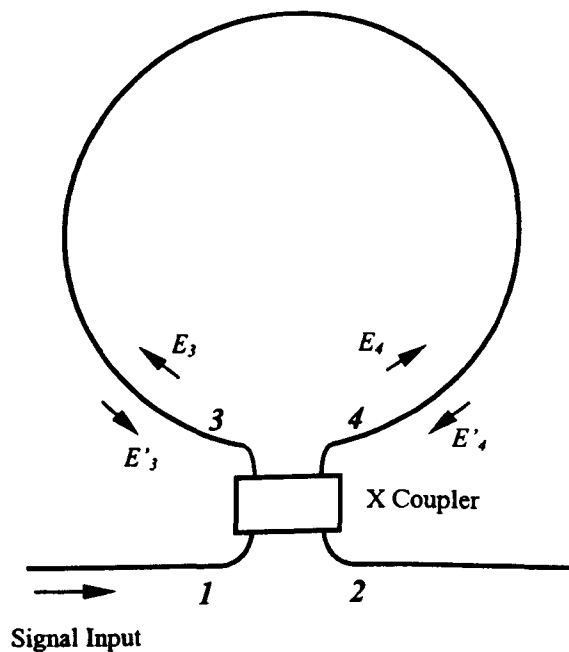


Figure 7.3.4 diagram of the Sagnac interferometer

When the input field  $E_0$  is launched into port 1, the output fields from port 3 and 4 are also given by (7.3.1) and (7.3.2). After the propagation round the whole loop, the electrical field launched into port 3 is

$$E'_3 = E_0 K_{CCW} \sin(CL_c) \cdot \exp[-j\frac{\pi}{2}] \exp[-j\Phi_{CCW}] \quad (7.3.13)$$

and that into port 4 is

$$E_4' = E_0 K_{CW} \cos(C \cdot L_c) \exp[-j\Phi_{CW}] \quad (7.3.14)$$

Then the output field from port 1 is

$$\begin{aligned} E_1' = & E_0 K_{CCW} \sin(CL_c) \cos(CL_c) \exp[-j\frac{\pi}{2}] \exp[-j\Phi_{CCW}] \\ & + E_0 K_{CW} \sin(CL_c) \cos(CL_c) \exp[-j\frac{\pi}{2}] \exp[-j\Phi_{CW}] \end{aligned} \quad (7.3.15)$$

Similarly, the output field from port 2 is,

$$E_2' = -E_0 K_{CCW} \sin^2(CL_c) \exp[-j\Phi_{CCW}] + E_0 K_{CW} \cos^2(CL_c) \exp[-j\Phi_{CW}] \quad (7.3.16)$$

Again, let us consider the simplest situation in which the field propagation losses and phase shifts are the same for CW and CCW directions, as well as the split ratio of X-coupler is 50:50. Then (7.3.15), (7.3.16) are simplified as

$$I_1' = E_0^2 K^2 \quad (7.3.17)$$

$$I_2' = 0 \quad (7.3.18)$$

Which means all the input signals are reflected back to the input port, and there is no signal out of port 2. However, there may be an output from port 2, according to (7.3.16), when any of the three cases listed below happens,

1. Split ratio of the X-couplers is not 50:50;
2. Propagation losses in the CW and CCW directions are not the same;
3. Phase shifts of the CW and CCW directions are not the same.

### **7.3.3 Operation of TOAD**

In the following analysis, we only consider a MZI structure of the type shown in Figure 7.3.1(a) and make several assumptions:

1. The optical coupler is ideal with a split ratio of 50:50.
2. The input signal's intensity is sufficiently small that no nonlinearity is generated by the signal.
3. The polarisation of pulses in both branches is the same and maintained throughout the whole device.
4. No reflections occur in the device.
5. The input signal can be distinguished from the control signal.
6. The linear gains of the two SOAs are the same.

Unlike the normal Mach-Zehnder interferometer, a MZI DMUX consists of two SOAs that are asymmetrically located within the two branches. If the two SOAs offer the same gain as well as additional phase shifts, the DMUX behaves just like the normal Mach-Zehnder interferometer. All the signals launched into the device are transmitted out from a particular port all the time. But, as we discussed in Section 7.2.1, when an ultrafast optical pulse (i.e., control pulse) with sufficient

intensity reaches the SOAs, it produces a rapid nonlinear change in the SOA's optical properties. This can impose a time-varying phase shift on any signal passing through the SOA at the time, due to the change in carrier density resulting from the nonlinearity. According to our analysis in Section 7.3.2, this leads to the response of the performance of the interferometer.

To obtain a clear understanding, let us consider three situations. First, when the control pulse enters the SOAs, the signals in both Branch A and B have passed through the SOAs. Signals in Branch A and B will have the same phase shift as the nonlinear transition has no effect on them. When meeting at the 3dB coupler, they will interfere as in the ordinary Mach-Zehnder interferometer and be transmitted out of port 6.

Second, when the control pulse enters the SOAs, the signals in neither Branch A nor B have passed through the SOAs. In this case, the nonlinear transition occurs in the SOAs when the signals lie more than  $\Delta x/2$  from, and are propagating toward, the midpoint. Both signals experience the post-transition properties of the SOAs. If the fall time of the nonlinearity of SOA satisfies,

$$\tau_{fall} \gg \Delta x / v \quad (7.3.19)$$

the signals in Branch A and B will experience virtually identical phase shifts. When meeting at the 3dB coupler, they will interfere and be transmitted out of port 6.

Third, when the control pulse enters the SOA in Branch B at about the same time as the signal in Branch A has just left the SOA. In this case, the optical transition occurs when both signals lie less than  $\Delta x/2$  from the midpoint, with the signal in Branch A moving away from its SOA and the signal in Branch B moving towards its SOA. Only the signal in Branch B undergoes an additional phase shift. If this additional shift is  $\pi$ , when meeting at the 3dB coupler the two signals will interfere and be transmitted out of port 5.

Thus the rapid transition (although its relaxation time is much longer) in the optical properties of the SOA opens a time-window with a duration of  $\Delta x/v$  between the MZI-DMUX's port 5 and 6.

Signals launched from port 5 are those located within  $\Delta x/2$  of the midpoint when the optical transition induced by control pulse occurs in the SOAs. If  $\Delta x/v \leq T_{\text{bit}}$  with proper timing of the control pulse any bit can be demultiplexed from the input data stream. Another bit cannot be demultiplexed until the optical properties of SOA have recovered. Therefore the data frame period  $T_{\text{frame}}$  must be larger than the fall time  $\tau_{\text{fall}}$  of the nonlinearity and the relationship is established:

$$\tau_{\text{rise}} < \tau_{\text{bit}} \ll \tau_{\text{fall}} < T_{\text{frame}} \quad (7.3.20)$$

It should be pointed out that, although the sampling window is only related to the nonlinearity rise time  $\tau_{\text{rise}}$  and asymmetry  $\Delta x$ , the relaxation time of the nonlinearity does limit the repetition rate at which switching can be performed. Therefore the applications of the switch are those that demand a narrow sampling

window but with a much larger repetition period. One such application is the OTDM demultiplexer.

## **7.4 Design of MZI-DMUX**

The design components of the MZI-DMUX included the device structure, passive waveguides, MMI couplers, semiconductor amplifiers and taper connectors.

The basic requirements of the waveguide are good mode confinement/distribution and low propagation loss as we discussed in Chapter 3. It has been concluded that deep etched waveguides are preferred in our design. The two proposed waveguide structures were:

Width of waveguide:  $2\ \mu\text{m}$  or  $3\ \mu\text{m}$

Height of waveguide:  $>1.5\ \mu\text{m}$

Employed as nonlinear element, the SOA is one of the main components in the MZI-DMUX. According to the calculation in Section 7.2.1, a typical SOA length of  $400\ \mu\text{m}$  can offer enough nonlinearity. In the design, a longer length of  $500\ \mu\text{m}$  was used so that enough gain and phase shift could be obtained. The designed offset between the centres of the two SOAs was  $300\ \mu\text{m}$  which corresponded to a  $\sim 3\ \text{ps}$  time delay.

The SOAs used the ridge waveguide structure. Considering the difficulty of manufacture (especially the window opening), the proposed geometric parameters

of the SOA waveguide were 4  $\mu\text{m}$  wide (window width of 1  $\mu\text{m}$ ) and a height of around 800 nm.

As the width of the SOA waveguide was larger than that of the passive waveguide and the etch depth of the SOA ( $\sim 800$  nm) was less than that of passive waveguides ( $>1.5$   $\mu\text{m}$ ), the optical modes propagating in these two waveguides were different. Hence a mode coupling loss occurred at the conjunction of the two waveguides. To reduce such a coupling loss, a taper structure was employed between two waveguides. The taper was 50  $\mu\text{m}$  long with one end 2  $\mu\text{m}/3$   $\mu\text{m}$  wide, 1.5  $\mu\text{m}$  deep and the other 4  $\mu\text{m}$  wide, 800 nm deep. The estimated mode-distortion loss of this taper structure was less than 0.3 dB [24].

The MMI coupler was designed using *BPM\_CAD* as discussed in Chapter 4. The designed MMI coupler structures were:

#### 1. MMI-2

Width of MMI section: 6  $\mu\text{m}$

Length of MMI section: 160  $\mu\text{m}$

Width of input/output waveguide: 2  $\mu\text{m}$

Separation distance between two input/output waveguides: 4  $\mu\text{m}$

Height of MMI section/access waveguide:  $>1.5$   $\mu\text{m}$

## 2. MMI-3

Width of MMI section:  $9\ \mu\text{m}$

Length of MMI section:  $360\ \mu\text{m}$

Width of input/output waveguide:  $3\ \mu\text{m}$

Separation distance between two input/output waveguides:  $6\ \mu\text{m}$

Height of MMI section/access waveguide:  $>1.5\ \mu\text{m}$

Because all the components discussed above were passive devices except the SOAs, a low propagation loss was required. This was achieved by intermixing all the areas except that for the SOAs so that the bandgap energy was larger than that of the SOA. Normally the required bandgap shift was larger than 100 nm.

Three kinds of MZI-DMUX structure were designed in this work.

Type-I was based on  $2\ \mu\text{m}$  wide passive waveguide structures. For the convenience of launching the control pulse into and coupling the signal out of the same side of the device, a sufficient large separation distance (chosen to be 1 mm) between the two output waveguides is required. This was achieved by curving the output waveguides out using a bend complex with  $287\ \mu\text{m}$  curvature. This curved bend did increase the total device length (6.8 mm), and hence the total insertion loss. Moreover, the input/output waveguides were inclined at  $6^\circ$  to the cleaved facets to reduce the reflectivity.

To reduce the total length of the device, a compact structure was designed. Type-II was also based on 2  $\mu\text{m}$  wide passive waveguides but with a much smaller separation distance (250  $\mu\text{m}$ ) between the two output waveguides. This reduced the length by almost 50% (3.5 mm) compared to Type-I.

As discussed in Chapter 3, narrow waveguides tend to have higher propagation losses due to the stronger influence of roughness of the sidewall. For comparison, Type-III was designed, based on 3  $\mu\text{m}$  wide passive waveguides. Because of the increase of waveguide width, the MMI section was longer than that of Type-I and Type-II, which led to a small increase to the total device length (4.3 mm). Table 7.4.1 summarises the structures of the three types of MZI-DMUXs.

Table 7.4.1 Characteristics of three types of MZI-DMUX

Device type	Type-I	Type-II	Type-III
Total device length (mm)	6.8	3.5	4.3
Separation of device access ( $\mu\text{m}$ )	1000	250	250
Tilted angle of output waveguide ( $^\circ$ )	6	0	0
Passive waveguide width ( $\mu\text{m}$ )	2	2	3
Passive waveguide depth ( $\mu\text{m}$ )	1.5	1.5	1.5
MMI section length ( $\mu\text{m}$ )	160	160	360
Separation of MMI access ( $\mu\text{m}$ )	4	4	6
Bend length of MMI coupler ( $\mu\text{m}$ )	870	400	390
Bend radius ( $\mu\text{m}$ )	287	319	287
SOA waveguide width ( $\mu\text{m}$ )	4	4	4
SOA waveguide height (nm)	800	800	800

## **7.5 Summary**

In this chapter, a brief introduction to high-speed demultiplexers has been presented. Based on an analysis of nonlinearity caused by carrier density changes in semiconductor optical amplifiers, the principle of terahertz optical asymmetric demultiplexer (TOAD) has been described qualitatively. Three designs of MZI type demultiplexers have been demonstrated.

## Reference

- [1] M. Chbat, B. Hong, M.N. Islam, C.E. Socolich, and P.R. Prucnal, 'Ultrafast soliton trapping AND gate', *J. Lightwave Technology*, Vol.10, pp.2011-2013, 1992
- [2] K.J. Blow, N.J. Doran, and B.P. Nelson, 'Demonstration of the nonlinear fibre loop mirror as an ultrafast all optical demultiplexer', *Electronics Letter*, Vol.26, pp.962-963, 1990
- [3] N.A. Whitaker, Jr., H. Avramopolous, M.C. Gabriel, P.M.W. French, R.E. LeMarche, and D.J. Digiovanni, and H.M. Presby, 'All-optical arbitrary demultiplexing at 2.5Gbits/s', *Optics Letter*, Vol.16, pp.1838-1841, 1991
- [4] M.N. Islam, E.R. Sunderman, R.H. Stolen, W. Pleibel, and J.R. Simpson, 'Soliton switching a fibre nonlinear mirror', *Optics Letter*, Vol.14, pp.811-813, 1989
- [5] N.J. Doran and D.Wood, 'Nonlinear loop mirror'. *Optics Letter*, Vol.13, pp.56-58, 1988
- [6] M. Eiselt, 'Optical loop mirror with semiconductor laser amplifier', *Electronics Letter*, Vol.28, pp.1505-1506, 1990
- [7] M. Eiselt, W. Pieper, and H.G. Weber, 'All-optical high speed demultiplexing with a semiconductor laser amplifier in a loop mirror configuration', *Electronics Letter*, Vol.29, pp.1167-1168, 1993
- [8] J.P. Sokoloff, P.R. Prucnal, and I. Glesk, 'Terahertz optical asymmetric demultiplexer (TOAD)', *OSA proceeding on Photonics in Switching*, Vol.16, pp.211-214, 1993

- [9] J.P. Sokoloff, P.R. Prucnal, I. Glesk, and M. Kane, 'A terahertz optical asymmetric demultiplexer (TOAD)', *IEEE Photonics Technology Letter*, Vol.5, pp.787-790, 1993
- [10] J.P. Sokoloff, I. Glesk, P.R. Prucnal, and R.K. Boncek, 'Performance of a 50 Gbit/s optical time domain multiplexed system using a terahertz optical asymmetric demultiplexer', *IEEE Photonics Technology Letter*, Vol.6, pp.98-100, 1994
- [11] K. Suzuki, K. Iwatsuki, S. Nishi, and M. Saruwatari, 'Error-free demultiplexing of 160Gbit/s pulse signal using optical loop mirror including semiconductor laser amplifier', *Electronics Letter*, Vol.30, pp.1501-1502, 1994
- [12] K.I. Kang, N. Agrawal, H.J. Ehrke, R. Ludwig, W. Pieper, and H.G. Weber, 'Demonstration of ultrafast, all-optical, low control energy, single wavelength, polarization independent, cascadable, and integratable switch', *Applied Physics Letter*, Vol.67, pp.605-606, 1994
- [13] K.I. Kang, I. Glesk, T.G. Chang, P.R. Prucnal, and R.K. Boncek, 'Demonstration of all-optical mach-zehnder demultiplexer', *Electronics Letter*, Vol.31, pp.749-750, 1995
- [14] E. Jahn, N. Agrawal, H.J. Ehrke, R. Ludwig, W. Pieper, and H.G. Weber, 'Monolithically integrated asymmetric mach-zehnder interferometer as a 20Gbit/s all-optical add/drop multiplexer for OTDM systems', *Electronics Letter*, Vol.32, pp.216-217, 1996
- [15] I. Glesk, J.P. Sokoloff, and P.R. Prucnal, 'All-optical address recognition and self-routing in a 250Gbit/s packet-switched network', *Electronics Letter*, Vol.30, pp.1322-1323, 1994

- [16] I. Glesk, J.P. Sokoloff, and P.R. Prucnal, 'Demonstration of all-optical demultiplexing of TDM data at 250Gbit/s', *Electronics Letter*, Vol.30, pp.339-341, 1994
- [17] E. Jahn, N. Agrawal, M. Arbert, H.J. Ehrke, R. Ludwig, W. Pieper, H.G. Weber, and C.M. Weinert, '40Gbit/s all-optical demultiplexing using a monolithically integrated mach-zehnder interferometer with semiconductor laser amplifier', *Electronics Letter*, Vol.31, pp.1857-1858, 1995
- [18] E. Jahn, N. Agrawal, R. Ludwig, H.J. Ehrke, D. Franke, W. Furst, and C.M. Weinert,, "Monolithically integrated nonlinear sagnac interferometer and its application as a 20Gbit/s all-optical demultiplexer", *Electronics Letter*, Vol.32, pp.782-784, 1996
- [19] M.J. Adams, 'A comparison of active and passive optical biastability in semiconductors', *IEEE J. Quantum Electronics*, Vol.QE-21, p1498, 1985
- [20] M.J. Adams, D.A.O. Davies, M.C. Tatham, and M.A. Fisher, 'Nonlinearities in semiconductor laser amplifier', *Optical and Quantum Electronics*, Vol.27, pp.1-13, 1995
- [21] A. Grabmaier, A. Hangleiter, G. Fuchs, J.E.A. Whiteaway, and R.W. Glew, 'Low nonlinear gain in InGaAs/InGaAlAs separate confinement multiquantum well lasers', *Applied Physics Letter*, Vol.59, pp.3024-3026, 1993
- [22] K.L. Hall, A.M. Darwish, E.P. Ippen, U. Koren, G. Raybon, 'Subpicosecond gain and index nonlinearity in InGaAsP diode lasers', *Optics Communications*, Vol.111, pp.589, 1994
- [23] R.G. Hunsperger, 'Integrated Optics: Theory and Technology', Springer-Verlag, pp.111-112, 1984
- [24] S. Yu, personal communication

## CHAPTER 8

# MONOLITHICALLY INTEGRATED MACH-ZEHNDER ASYMMETRIC INTERFEROMETER DEMULTIPLEXER: FABRICATION AND ASSESSMENT

In this chapter, the fabrication process of the monolithically integrated Mach-Zehnder asymmetric interferometer demultiplexer is presented. Device assessment is described, which includes the operation of the SOA, propagation loss of the device, etc.

## 8.1 Quantum well intermixing using sputtering process disordering

First, an InGaAs/AlInGaAs sample, its structure shown in Table 2.2.1, was scribed into pieces measuring  $6 \times 9 \text{ mm}^2$  and cleaned. The cleaning process used acetone and methanol each for 5 minutes in an ultrasonic bath. The sample was then rinsed in RO water for two minutes and dried. After deposition with a layer of PECVD  $\text{SiO}_2$  of 200 nm thickness, the sample was patterned by photolithography and HF wet etching so that only the areas (each of size  $500 \times 300 \mu\text{m}^2$ ) to be defined with amplifier structure were capped with PECVD  $\text{SiO}_2$  and photoresist S1818. After that a 20 nm  $\text{SiO}_2$  sputtering process was carried out, followed by a cleaning stage to remove the photoresist S1818. The sample was annealed in the RTA at  $640^\circ\text{C}$  for 90 seconds. During the annealing, the sample was placed between two Si wafers to limit evaporation of the Group V elements. Finally, PL measurements were carried out to determine the bandgap shift. Fig.8.1.1 shows the PL spectra from the SOA areas, intermixed areas and as-grown wafer at 77 K. It can be seen that the bandgap of the intermixed area (for passive waveguides and MMI couplers) has more than a 160 nm blue shift. Simultaneously, effective suppression is observed in the SOA areas, with only a 2 nm blue shift.

After the intermixing process, the sample was wet etched with HF to remove both the PECVD  $\text{SiO}_2$  and sputtered cap layers.

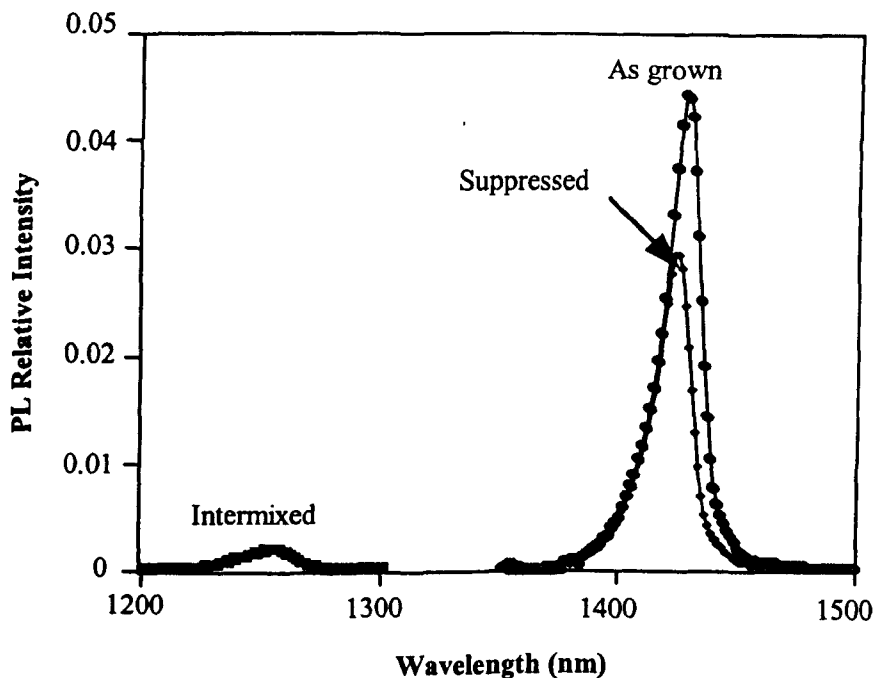


Figure 8.1.1 the PL spectra of suppressed areas for SOAs, intermixed areas and as-grown wafer at 77 K

## 8.2 Pattern Transfer Process on InGaAs/AlInGaAs Structure

The next stage of fabrication was pattern transfer, which includes:

1. Deposition of suitable masking material ( $\text{SiO}_2$ ,  $\text{SiN}$ ,  $\text{Ti}$ ,  $\text{NiCr}$ , etc.) on the top of semiconductor wafer.
2. Photolithography of whole pattern on mask material using a particular photoresist, such as S1805 and S1818.
3. Etching the masking material to obtain the desired pattern mask by using a wet or dry etching process.

The key of this stage is to keep the accuracy of transfer as high as possible, which is vital for the whole fabrication. In Chapter 4, we have discussed the MMI couplers that are one of the major components of the integrated Mach-Zehnder asymmetric interferometer demultiplexer. The MMI couplers should be dry etched to a certain depth (in our case, deeper than 1.5  $\mu\text{m}$ ) with high pattern transfer accuracy so that the cross talk between access waveguides can be eliminated and desired split ratio can be obtained. That means a total etch time longer than 45 minutes is required. It is very important to ensure the selected mask material is durable enough to stand such a long period of bombardment without any significant pattern erosion.

### **8.2.1 The photoresists**

There are two kinds of photoresist normally used in photolithography in the Department: S1818 and S1805. Under standard spinning conditions (4000rpm, 30 s), the thickness of S1818 is 1.8  $\mu\text{m}$  and S1805 is 0.5  $\mu\text{m}$ .

The mask aligner used was manufactured by STG and worked on the principle of contact printing. Ideally the mask plate and the wafer are vacuum clamped together without any gap between them for exposure. In practice, contact between the mask and the wafer is not perfect and some small amount of Fresnel diffraction occurs. During the photolithography, if the contact between mask plate and the photoresist on the sample is not good enough, the Fresnel diffraction tends to degrade the defined pattern and makes small features, such as waveguides, narrower than intended. It was found that the thicker the photoresist, the worse the contact. Fig.8.1.2 shows SEM micrographs of photolithographic patterns of an

MMI coupler defined with (a) S1818 and (b) S1805. It is obvious that S1805 is much better than S1818 when used to define small features such as an MMI coupler. Particularly when defining repeated small features across a large wafer, it is almost impossible to obtain satisfactory results using photoresist S1818. This is mainly because of poor contact when photolithography is carried out on a large sample.

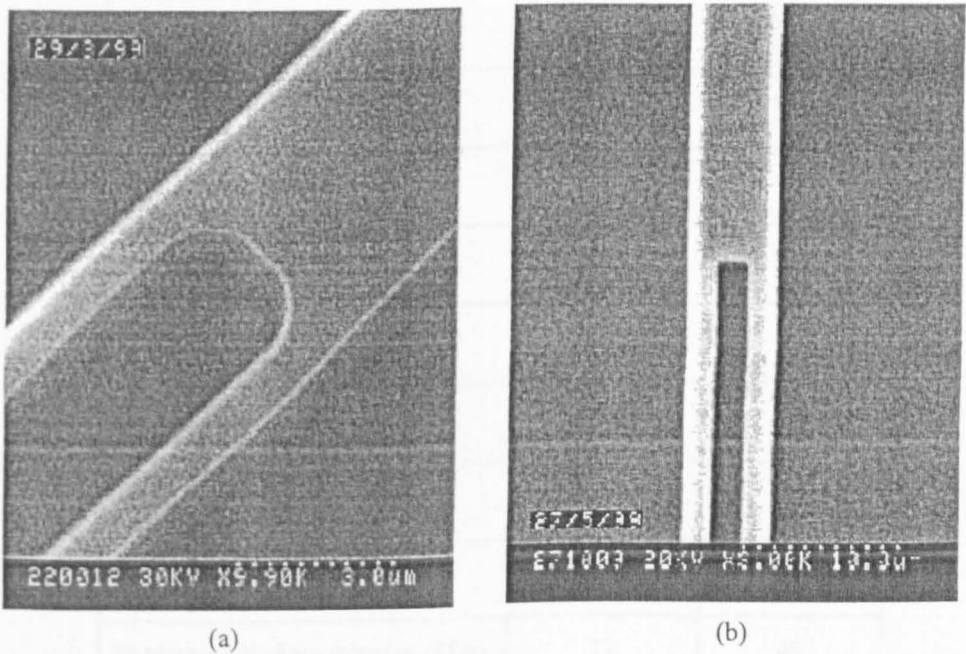


Figure 8.2.1 SEM photos of a MMI coupler pattern defined with (a) S1818 and (b) S1805

### 8.2.2 Pattern transfer process with $\text{SiN}_x$ as mask material

$\text{SiN}_x$  is a popular mask material used in III-V semiconductor device fabrication. In the Department, the dry etching of  $\text{SiN}_x$  is performed in the BP80 RIE machine, using  $\text{CHF}_3$  or  $\text{C}_2\text{F}_6$ . The etching conditions are shown in Table 8.2.1. As previously described, during the dry etching process, the photoresists are also etched by the RIE plasma, which could cause pattern transfer error. In particular,

if the photoresist pattern is not well transferred because of poor contact, the high photoresist etching rate could cause the mask pattern to become mis-shaped. For this reason,  $\text{CHF}_3$  is preferred in our fabrication as the etching rate of the photoresist is only 1/3 of that of the substrate, as opposed to  $\text{C}_2\text{F}_6$  which is nearly equal etch rates for the two materials.

Table. 8.2.1 the etching process recipes for SiN

	Recipe-1	Recipe-2
Etching Gas	$\text{CHF}_3$	$\text{C}_2\text{F}_6$
Flow Meter Reading (%)	20	80
Correct Flow (Sccm)	20	20
Etching Pressure (mtorr)	11	12
RF Forward Power (W)	100	100
RF Reflected Power (W)	0	0
Etching Rate (nm/Min.)	29	45
Photoresist Etching Rate (nm/Min)	12	40

To find out if the  $\text{SiN}_x$  is hard enough to withstand the  $\text{CH}_4/\text{H}_2$  RIE, experiments were carried out with  $\text{SiN}_x$  masks of thickness of 200 nm. Figure 8.2.2(a) and (b) show SEM micrographs of the profiles of a 2  $\mu\text{m}$  waveguide and a MMI coupler after 45 minutes  $\text{CH}_4/\text{H}_2$  etching in the ET340 RIE machine. The  $\text{SiN}_x$  mask was narrowed significantly because of the  $\text{CH}_4/\text{H}_2$  bombardment, which resulted in the badly mis-shaped profile.

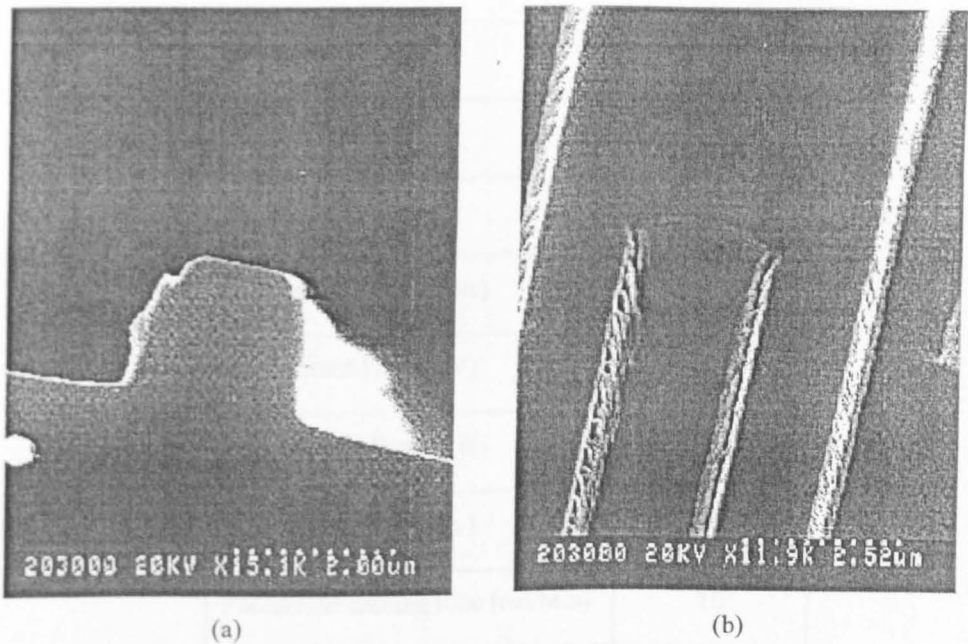


Figure 8.2.2 SEM photos of the profiles after 45 minutes etch

### 8.2.3 Pattern transfer process with Ti/SiO<sub>2</sub> as mask material

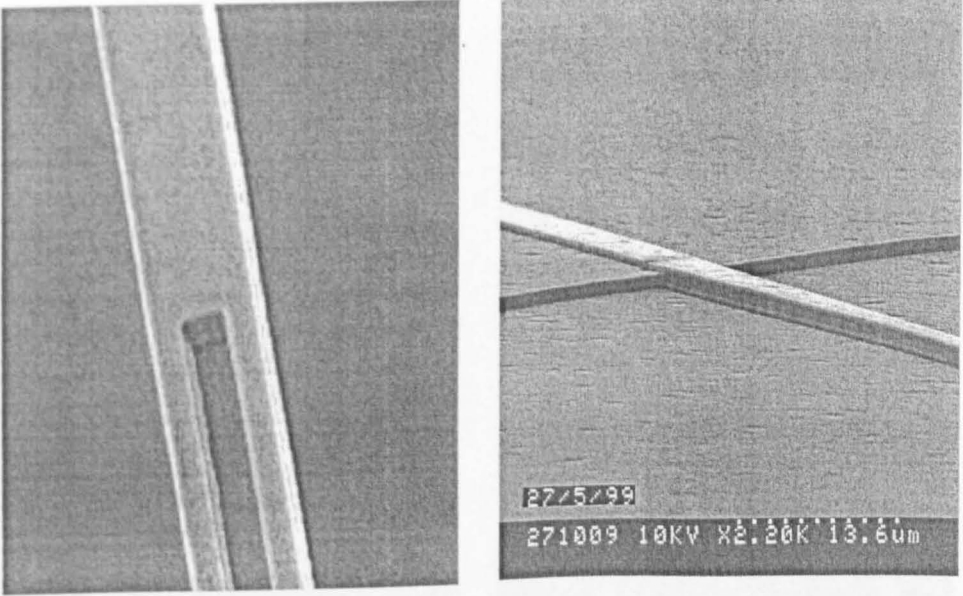
An improved pattern transfer process was developed recently to avoid the significant transfer error associated with the SiN<sub>x</sub> process. In this process, a combination of Ti and PECVD SiO<sub>2</sub> was employed as the mask material. First a layer of 200 nm of PECVD SiO<sub>2</sub> was deposited on the substrate surface, followed by 100 nm of Ti. After defining the whole pattern using photoresist S1805 on the Ti layer, SF<sub>6</sub> was employed to etch the layer of Ti and CHF<sub>3</sub> the layer of SiO<sub>2</sub> in BP80 RIE machine. Table 8.2.2 gives the recipe of SF<sub>6</sub> process. As a metal mask material, Ti is sufficiently durable to withstand a long CH<sub>4</sub>/H<sub>2</sub> etch and maintains the pattern accurately. An etching test of 70 minutes showed that there was no significant distortion of the mask shape, which happened during the SiN<sub>x</sub> process.

Table. 8.2.2 the etching process recipes for Ti

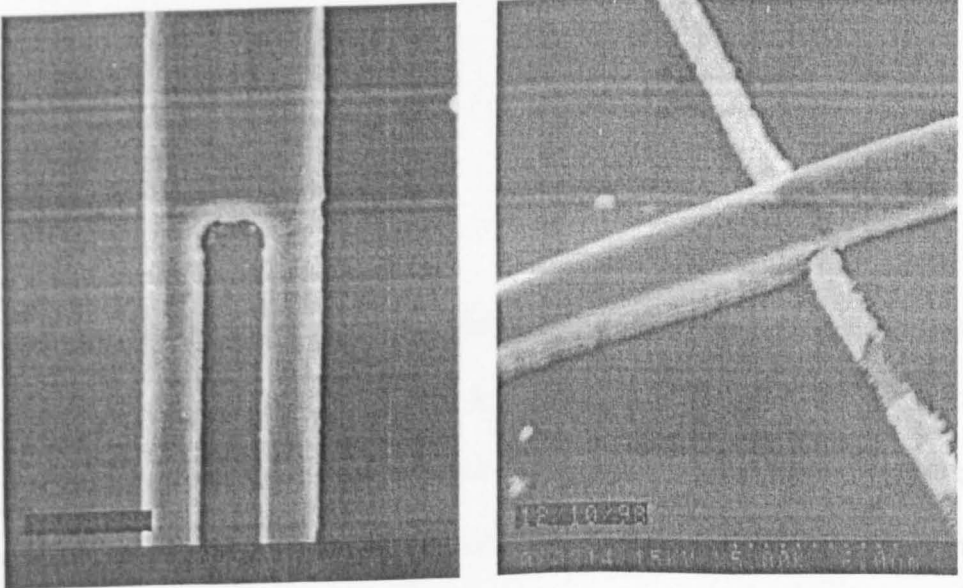
	Recipe
Etching Gas	SF <sub>6</sub>
Correct Flow (Sccm)	10
Etching Pressure (mtorr)	13
RF Forward Power (W)	100
RF Reflected Power (W)	0
Etching Rate (nm/Min.)	30
Photoresist Etching Rate (nm/Min)	10

Fig.8.2.3 (a) shows SEM micrographs of the profiles of MMI couplers and taper connectors fabricated using Ti/SiO<sub>2</sub> mask process. It can be seen that the sidewall is vertical and the rectangular corner is of good shape. For comparison, SEM micrographs of same structures fabricated using the SiN<sub>x</sub> mask process are shown in Figure 8.2.3 (b). It is obvious that sidewall is very rough, sloping and the rectangular corner is round. There is no doubt that Ti/SiO<sub>2</sub> mask is much better than SiN<sub>x</sub> masks in transferring small features, so Ti-SiO<sub>2</sub> masks were used in the pattern transfer process.

When using Ti/SiO<sub>2</sub> as a mask, two aspects required more attention. First, before depositing Ti, the SiO<sub>2</sub> surface should be well cleaned. Second, it is better that the thickness of Ti is not more than 100 nm. If the surface is not clean or the Ti is too thick, the Ti mask may lift off during the etching process (See Figure 8.2.4), due to the different thermal expansion and poor adhesion between Ti and SiO<sub>2</sub>.



(a) Profiles of MMI coupler and taper connector by using Ti-SiO<sub>2</sub> mask



(b) Profiles of MMI coupler and taper connector by using SiN mask

Figure 8.2.3 comparison between SiN mask and Ti-SiO<sub>2</sub> mask process

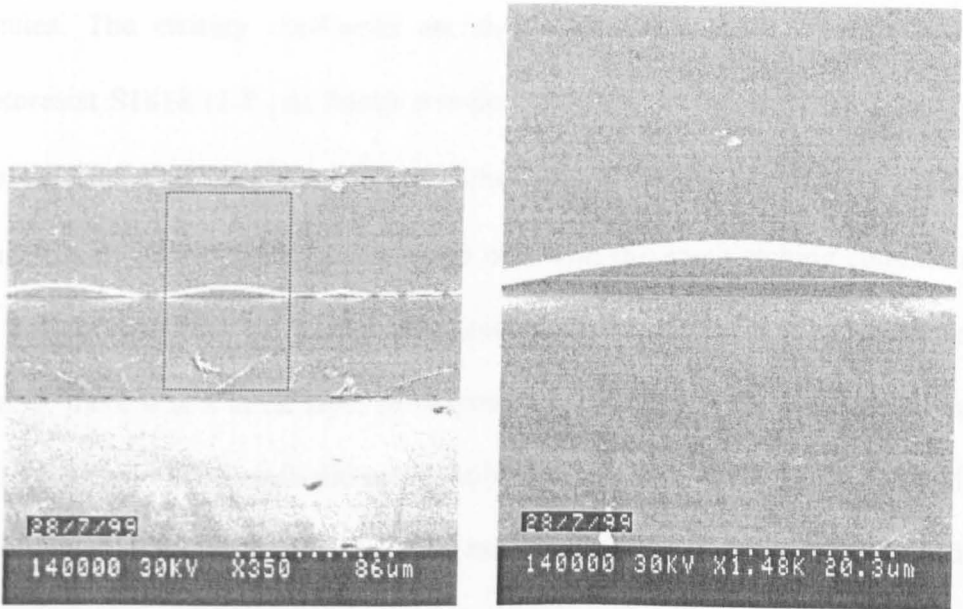


Figure 8.2.4 lifted Ti mask during SiO<sub>2</sub> etching process

### 8.3 Dry etching process

As discussed in Chapter 7, the amplifiers should be shallow etched to prevent excess nonradiative recombination, while all the passive waveguides need to be deep etched to maintain good confinement and distribution. According to theoretical analysis and experiment investigation, the best performance can be achieved when the etching stops about 200 nm above the upper cladding layer, in our case meaning that 800 nm InGaAs/AlInGaAs should be removed. On the other hand, at least 1.5  $\mu\text{m}$  of semiconductor should be removed in the passive areas to give the effective wave guiding.

The dry etching process included several steps. First was the shallow etching. The whole sample was etched using  $\text{CH}_4/\text{H}_2$  in the ET340 RIE machine for 22 minutes. The etching conditions are shown in Table 2.2.4. Then a layer of photoresist S1818 (1.8  $\mu\text{m}$  thick) was defined only on the amplifier areas (each size of  $500 \times 300 \mu\text{m}^2$ ) to protect the whole areas from future etching. Subsequently, deep etching was carried out, with the same etching conditions in the ET340 machine for another 25 minutes. It was found that, after the deep etching, there was a thick layer of polymer deposited on the top of the Ti mask, while the photoresist mask did not dissolved in acetone any more because of the crosslinking. A standard  $\text{O}_2$  clean of 10 minutes duration was therefore carried out in the ET340 RIE machine to remove the polymer and photoresist mask. The Ti- $\text{SiO}_2$  mask was then removed by HF wet etching.

Finally, the sample was capped with another layer of PECVD  $\text{SiO}_2$  and annealed in the RTA at  $500^\circ\text{C}$  for 90 seconds to anneal out any damage generated during the dry etching processes.

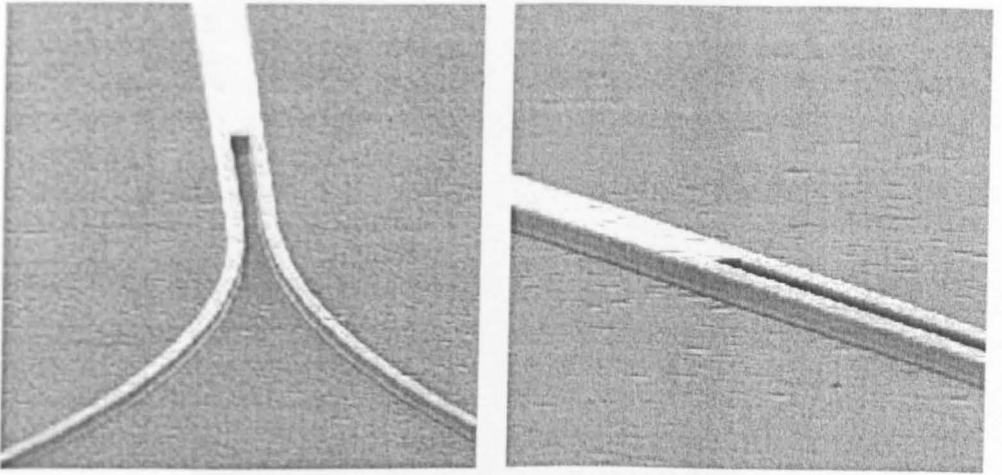
#### **8.4 Metal contact layer deposition and device bonding**

A P-contact window was opened along the amplifier waveguides using photolithography and HF wet etching. The sample was thinned to 150  $\mu\text{m}$  and metal contact layers (p side, Ti : Pd : Au :: 20 : 20 : 150 nm; n side, Au : Ge : Au : Ni : Au :: 14 : 14 : 14 : 10 : 200 nm) were evaporated onto both surfaces and

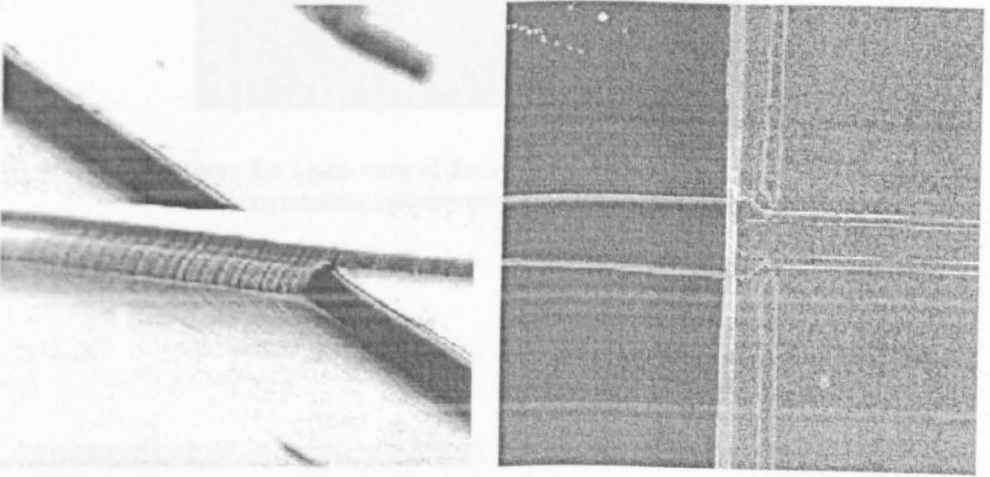
alloyed in the RTA at 360°C for 60 seconds. Finally, the sample was cleaved into individual devices.

Figure 8.4.1 shows some features of the device and Figure 8.4.2 shows a plan view of the whole device.

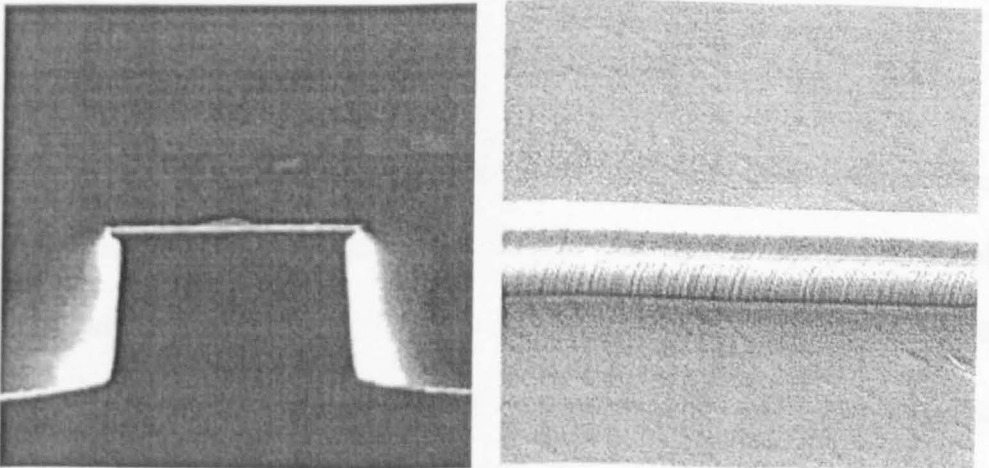
The device was bonded with indium onto the surface of a small copper heatsink that had been coated with 250  $\mu\text{m}$  of Au in advance. First, a small piece of indium was placed on the surface of heatsink and a thin layer of flux was sprayed over it and the surrounding area. After the device was located near the indium, the heatsink was heated on a hot plate to a precise temperature. As the device was pushed towards the molten the In was sucked into the gap between the device and the heatsink. After adjusting the device into its final position, the heatsink was cooled to room temperature. Control of the amount of indium and flux is very important as well as the operation technique during this stage. Much attention should be paid to avoid contamination of the device facets. Finally, two p-contact pads were connected to the electric pin-out with Au wire using a KS-4123 ultrasonic wiring machine.



(a) Views of MMI couplers



(b) Views of taper connectors



(a) Views of passive waveguides

Figure 8.4.1 SEM micrographs of some features of the device

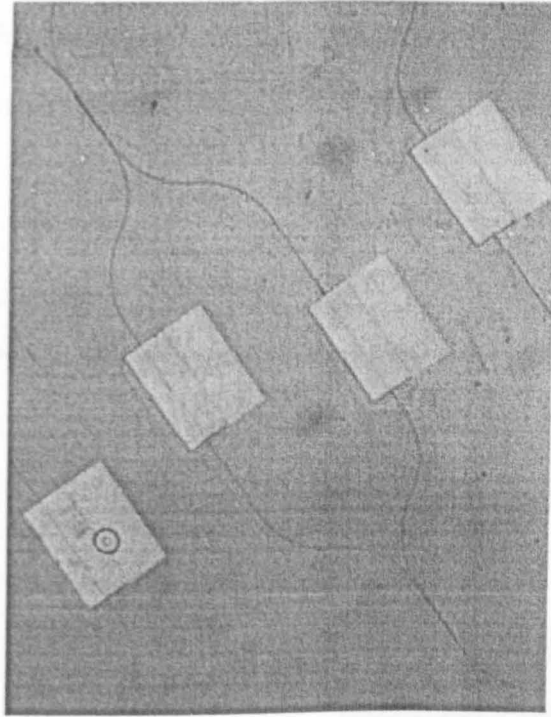


Figure 8.4.2 plan view of the integrated Mach-Zehnder asymmetric interferometer demultiplexer

## 8.5 Assessment of integrated Mach-Zehnder asymmetric interferometer demultiplexer

### 8.5.1 Experimental set-up

The assessment of MZI-DMUX was carried out in the test bed shown in Figure 8.5.1, which is similar to that used in the waveguide and MMI coupler measurements. The light from the  $1.55\ \mu\text{m}$  tunable laser was coupled into the waveguide of the semiconductor optical amplifier via a standard  $1.55\ \mu\text{m}$  single mode fibre. On the output tapered end of the fibre, a micro-lens was formed using the fibre splicer, so that relatively high coupling ( $\sim 4\text{-}5\ \text{dB}$ ) could be achieved. The

output from the device under test was coupled into another single mode fibre with a lensed tip. Using a 3dB fibre coupler, the signal was split and transferred into a detector and optical spectrum analyser.

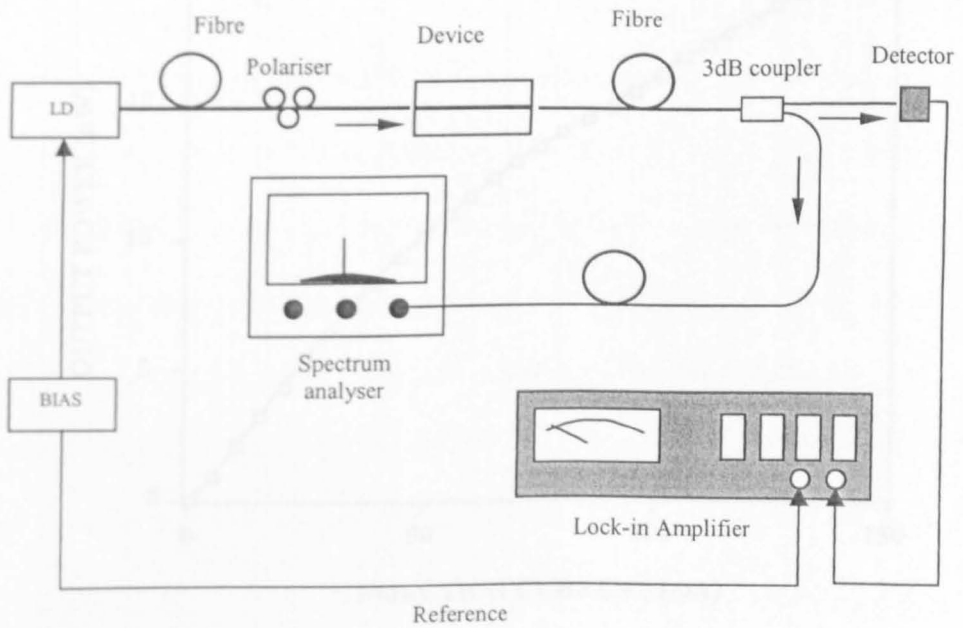


Figure 8.5.1 experimental set-up of MZI-demultiplexer assessment

### 8.5.2 Assessment of semiconductor optical amplifier

To assess the performance of the semiconductor optical amplifier (SOA), some discrete SOA devices were fabricated on the 5QW wafer shown in Table 2.2.1, following the fabrication process described above. To minimise reflections from the facets, the  $5\ \mu\text{m}$  wide amplifier waveguides were tilted at  $6^\circ$  from normal to the facet. Fig.8.5.2 shows the spontaneous emission power from one facet as a function of SOA injection current, the absence of lasing confirming that the facet reflection was well eliminated. Fig.8.5.3 shows the spontaneous emission spectra

of the SOA when biased at 50 mA. The central wavelength of the emission is around 1557 nm, with a FWHM of ~100 nm.

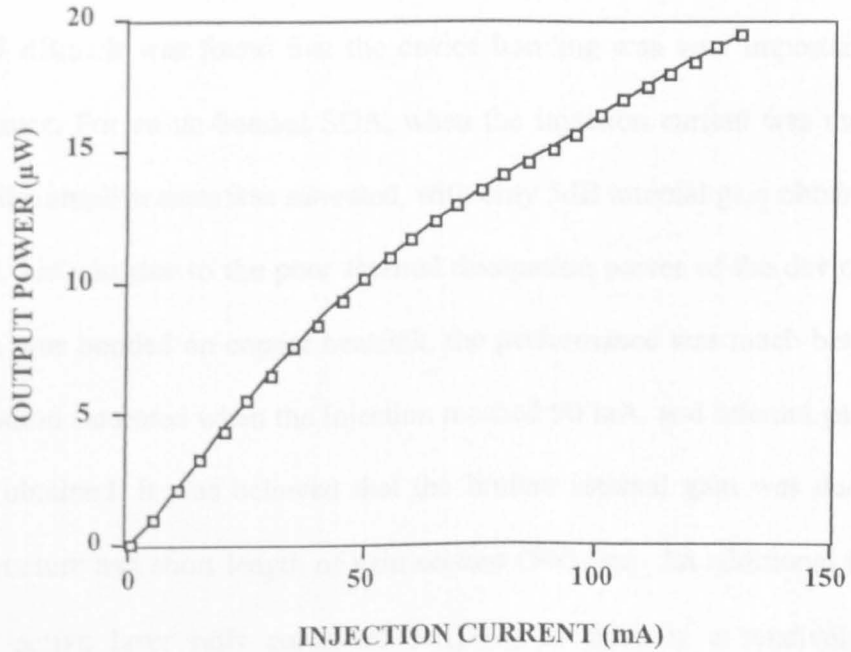


Fig.8.5.2 Spontaneous emission as a function of SOA injection current

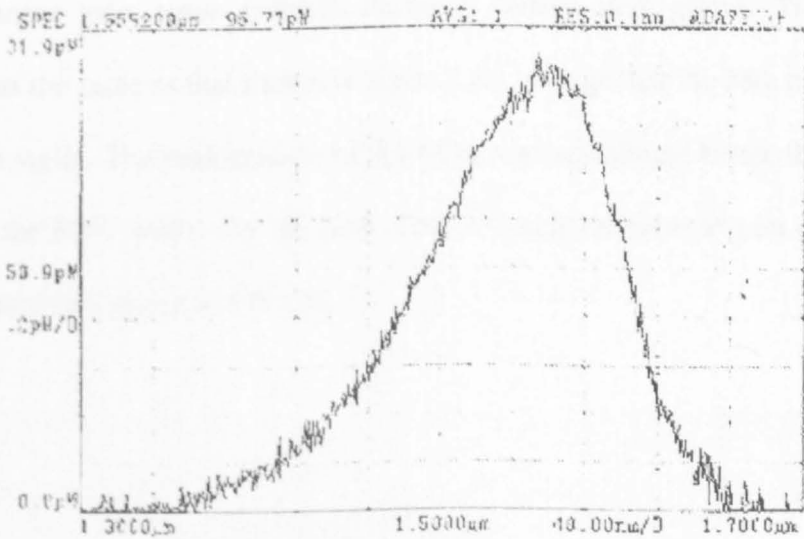


Fig.8.5.3 the spontaneous emission spectra of a 500 µm / 6° tilted AlInGaAs SOA

The amplification experiment was carried out using the test bed shown in Figure 8.5.1. The tunable laser was stabilised at  $-7$  dBm DC output power with 25% sinusoidal modulation. Because of the high coupling loss caused by the tilted facet, the estimated input optical power into the amplifier waveguide was lower than  $-17$  dBm. It was found that the device bonding was very important to the performance. For an un-bonded SOA, when the injection current was more than 30 mA, the amplification was saturated, with only 5dB internal gain obtained. It is believed this was due to the poor thermal dissipation power of the device. After the SOA was bonded on copper heatsink, the performance was much better. The amplification saturated when the injection reached 90 mA, and internal gain of 15 dB was obtained. It was believed that the limited internal gain was due to the wafer structure and short length of gain section (500  $\mu\text{m}$ ). An additional factor is that the active layer only contained 5 QWs, so there is a relatively small amplification overlap with the guided mode.

To obtain more gain, some specially designed wafers were grown. The wafer structure was the same as that shown in Table 2.2.1, except that the core contained 10 quantum wells. The performance of the SOA was significant better than those made from the 5QW wafer. For the same device length, an internal gain of 25 dB was obtained when biased at 125 mA.

### 8.5.3 Assessment of integrated Mach-Zehnder asymmetric interferometer demultiplexer

Assessment of the integrated Mach-Zehnder asymmetric interferometer demultiplexer focused on two aspects: the total propagation loss and the amplification of the integrated amplifiers.

Three types of demultiplexer were fabricated, with the designed structure parameters shown in Table.7.4.1. Table 8.5.1 gives a comparison of the three types of demultiplexer fabricated in 5QW material.

Table 8.5.1 Designed parameters of three types of MZI demultiplexer

Device type	Type-I	Type-II	Type-III
Device Length (mm)	6.8	3.5	4.3
Output waveguide separation ( $\mu\text{m}$ )	1000	250	250
Length of the bend ( $\mu\text{m}$ )	870	400	390
Shallow etch depth (nm)	807	980	807
Deep etch depth (nm)	1547	1560	1450
Waveguide width ( $\mu\text{m}$ )	2.1	2	2
Separation in MMI ( $\mu\text{m}$ )	1.8	2	2
Total loss (Fibre-Fibre) (dB)	86.5	43	40

\*Wafer: MR1403 MOCVD InGaAs/AlInGaAs 5QW laser material

Table 8.5.1 clearly indicates that, apart from the loss associated with the intermixing process, the waveguide profile can cause high propagation loss. Generally speaking, long, narrow waveguides, as well as small bend radii, induce large propagation losses.

Table 8.5.2 gives the characteristics of two Type-II MZI demultiplexers. The patterns of DMUX-14/DMUX-15 were defined using photolithography. Although DMUX-14 and DMUX-15 were fabricated in the same way, the pattern of DMUX-14 was narrowed about 0.2  $\mu\text{m}$  due to over etching during the BP80 process. This resulted in a total extra propagation loss of 16.5 dB, which indicates that the propagation loss of narrow waveguides is very sensitive to the width because of sidewall surface scattering.

Table 8.5.2 Characteristics of two Type-II MZI demultiplexers

Type-II device	DMUX-14	DMUX-15
Device Length ( $\mu\text{m}$ )	3.5	3.5
Access waveguide separation (nm)	250	250
Shallow etching depth (nm)	860	980
Deep etching depth (nm)	1470	1560
Waveguide width ( $\mu\text{m}$ )	1.8	2
Separation in MMI ( $\mu\text{m}$ )	2.2	2
Max. Amplifier Bias (mA)	90	90
Max. Internal gain (dB)	10	8
Total loss (Fibre-Fibre)	59.5	43

Performance tests of the MZI-demultiplexers were carried out at The Photonics Research Group, Aston University, using their 40 Gbit/s transmission system test bed. The light source was a 1553 nm DFB laser with a maximum output power level of +4 dBm. The receiver sensitivity of the test bed was -20 dBm. The test was unsuccessful because the high insertion loss of the devices (>40 dB) made the signal undetectable even with the help of the semiconductor optical amplifiers.

From the results obtained, several issues have been raised that require further investigation. The most important one is to reduce the transmission loss associated with the QWI process. During the intermixing process, 200 nm SiO<sub>2</sub> was directly sputtered onto the surface of semiconductor where bandgap was to be tuned. SIMS analysis showed that this process introduced Cu of more than  $1 \times 10^{18} \text{ cm}^{-3}$  across the cladding/core region (Figure 5.4.4) during the successive annealing stage. Due to the fact that diffused Cu is both electrically and optically active [1], this excess amount of Cu existing in cladding and core region would lead to strong impurity-related non-radiation absorption. This issue is serious but solvable, according to the result shown in Chapter 6. Accurately controlling the amount of Cu introduced during QWI by using PECVD SiO<sub>2</sub> protection layers, it is possible to achieve both a large blue-shift and negligible additional loss. Some more effective and accurate methods of Cu concentration control is currently under investigation in Intense Photonics Ltd. Secondly, an optimised waveguide design could make the insertion loss of the whole device relatively low. The insertion loss can be further minimised by using the technique of Hydrogen passivation [2-3]. Hydrogen can passivate both shallow acceptor and donor impurities in many technologically important semiconductors [4] and leads to important modifications of the electrical and optical properties of semiconductors. In the Zn-doped semiconductor, through formation of Zn-H complexes, atomic hydrogen deactivates Zn acceptors nearly completely [5], which leads to significant reduction of holes concentration in the upper p-doped cladding layer. This directly causes a drastic drop in the intervalence band absorption by free holes, hence the total propagation loss. This technology has been applied in fabrication of III-V integrated optoelectronic circuits [6]. Finally, accurate pattern

transfer would ensure that no extra loss is caused by misshapen waveguide profiles.

## **8.6 Summary**

The fabrication process of the monolithically integrated Mach-Zehnder asymmetric interferometer demultiplexers has been presented, which includes quantum well intermixing, pattern transfer, dry etching and contact deposition. A series of assessment has been carried out, which includes operation of semiconductor optical amplifier, propagation loss of the device, etc. Due to the high insertion loss of the devices, no performance tests were carried out successfully. Based on an assessment of the devices, several issues have been raised requiring the further investigation.

## Reference

- [1] M.S. Skolnick, E.J. Foulkes, and B. Tuck, 'Transition metal diffusion in InP: Photoluminescence investigation', *J. Applied Physics*, Vol.55, pp.2951-2961, 1984
- [2] J.I. Pankove, D.E. Carlson, J.E. Berkeyheiser, and R.O. Wance, *Physical Review Letter*, Vol.51, pp2224-2226, 1983
- [3] A. Jalil, J. Chevallier, R. Azoulay, and R. Micrea, 'Electron mobility studies of the donor neutralization by atomic hydrogen in GaAs doped with silicon', *J. Applied Physics*, Vol.59, pp3774-3785, 1986
- [4] S.J. Pearton, J.W. Corbett, and T.S. Shi, *Applied Physics A: Solid Surface*, Vol.A43, pp153-167, 1987
- [5] S.J. Pearton, J.W. Corbett, and M. Stavola, 'Hydrogen in Crystalline Semiconductor', Springer-Verlag, Heidelberg, 1992
- [6] E.V.K. Rao, Y. Gottesman, M. Allovon, B. Theys, H. Sik, and S. Slempek, 'Hydrogenation of buried passive sections in photonic integrated circuits: A tool to improve propagation losses at  $\sim 1.56 \mu\text{m}$ ', *Proceeding of ExMatec '98*, Cardiff, Jun 1998

## CHAPTER 9

### CONCLUSIONS AND FUTURE WORK

## **9.1 Conclusions**

The work described in this thesis is aimed at exploring the possibility of monolithically integrated multi-bandgap energy opto-electronic devices on appropriate semiconductor substrates, using the technology of quantum well intermixing. Several types of devices have been investigated: the multi-wavelength laser array that is of considerable importance for WDM systems, the 2×2 cross-point switch and the Mach-Zehnder interferometer demultiplexer, which will play important roles in WDM and OTDM systems. It has been shown that such devices could be integrated on III-V semiconductor multiple quantum well material, especially InGaAs/AlInGaAs system, if the design of the devices and the choice of fabrication techniques are carefully considered. A lot of work addressing this issue has been carried out and many conclusions from this study have been reached which are summarised below.

### **9.1.1 Reactive ion etching (RIE) process for InGaAs/AlInGaAs MQW system**

The reactive ion etching process with CH<sub>4</sub>/H<sub>2</sub> etching gas has been investigated, especially for the effective etching on InGaAs/AlInGaAs MQW system in an ET340 RIE machine. Al is chemically active and very easily oxidised. The resulting Al<sub>2</sub>O<sub>3</sub> is very difficult to etch from the wafer surface, so further etching is prevented. For this reason, unlike the dry etching process for InGaAs/InGaAsP system, only CH<sub>4</sub>/H<sub>2</sub> without O<sub>2</sub> can be used as the etching gas during the etching process for InGaAs/AlInGaAs system.

It has been found that:

1. The creation rate of the polymer is proportional to the gas flow rate. If the gas flow rate is too large, the polymer deposited on the surface will not be sputtered away by ions and more and more polymer will be deposited on the surface. Eventually etching will stop.
2. A suitable RF power level is important to the process. High RF power can produce better side wall verticality and a higher etching rate but poorer optical and electronic characteristics because the dry etch damage increases with the increasing of intensity of ion bombardment and ion energy that is determined by RF power. On the other hand, a low RF power could lead to the etching stopping if the RF power is too low to remove the polymer by sputtering.

Considering the balance between the etching rate, sidewall sharpness and the dry etching damage, a group of process parameters was chosen as our 'standard' process for InGaAs/AlInGaAs material system. The etching rate for this recipe is around 38 nm/min.

It has been found that, occasionally, the dry etching stopped in some areas or even the whole surface. This is thought to be mainly due to a small amount of residual O<sub>2</sub> in the etching chamber reacting with the Al and forming Al<sub>2</sub>O<sub>3</sub>. An improved pre-cleaning stage has been developed with significant success to address this problem. First, the chamber is cleaned with O<sub>2</sub> for 10 minutes, followed by H<sub>2</sub> cleaning for 20 minutes. Then the chamber is pumped to the desired vacuum level

and  $\text{CH}_4/\text{H}_2$  etching gas is flown into the chamber. After 1 minute, the RF source is switched on to start the etching.

### **9.1.2 Theory, design and Characterisation of waveguides**

A brief theoretical description of the waveguide has been discussed. Several types of deep etched waveguides have been fabricated and characterised. It has been found the sidewall roughness of narrow, deep etched waveguide has a strong influence on the propagation loss as in such case the surface energy scattering on waveguide side wall is significant.

### **9.1.3 Modelling, design and fabrication of MMI couplers**

The modelling and design of 3-dB MMI couplers have been carried out by using BPM\_CAD. An improved Ti/SiO<sub>2</sub> masking method has been successfully employed to ensure the actual profiles of the MMI couplers meet the design, especially the feature definition of the MMI section. The characterisation has shown good agreement with the design. A split ratio of 46:54 has been achieved for a coupler with 160  $\mu\text{m}$  long MMI section and 51:49 for one with 360  $\mu\text{m}$  long MMI section.

### **9.1.4 Novel multi-bandgap quantum well intermixing technique on 1.55 $\mu\text{m}$ InGaAs/AlInGaAs and InGaAs/InGaAsP MQW material**

A novel quantum well intermixing technique, based on a sputtering process induced disordering (SID), has been developed for the first time, addressing multi-bandgap active device integration. SIMS analysis showed that during SID process, Cu was involved and played an important role in QWI enhancement. As one of

the 3d transition metals, Cu, having a very high diffusion coefficient, is known to diffuse interstitially and to move onto group III lattice sites through the 'kick-out' mechanism. Because of its fast diffusion, Cu is much more efficient than many other impurities in generating point defects. For the same reason, it can enhance QWI at relatively low temperatures.

By locally controlling the thickness of the PECVD SiO<sub>2</sub> cap, the concentration of Cu introduced into III-V semiconductor during the sputtering/annealing process can be controlled. Hence, local control of the bandgap shift in the QW can be obtained. Due to the barrier effect of PECVD SiO<sub>2</sub>, the concentration of Cu within waveguide/core region is reduced dramatically. This achievement makes SID one of the practical techniques in the fabrication of low loss waveguides in the future.

Using this novel technique, the blue shifts have been precisely tuned from 0 nm to over 160 nm for InGaAs/AlInGaAs and from 0 nm to 110 nm for InGaAs/InGaAsP MQW systems. Assessment of post-process material characteristics has shown that good electrical and optical qualities have been maintained in the bandgap widened regions. For a laser wavelength shift as large as 100 nm, the threshold current density of the InGaAs/AlInGaAs oxide stripe laser increased by only 16% compared to that of the as-grown laser, it is believed that the increase is mainly due to the well shape changing and the carriers becoming less confined within the wells. For the same bandgap shift, the internal quantum efficiency decreased by only ~4%, implying that the process did not introduce a significant number of nonradiative recombination centres.

The same assessment has also been carried out on bandgap-tuned InGaAs/InGaAsP material. For a laser wavelength shift as large as 110 nm, the threshold current density of the laser increased by only 6% compared to that of as-grown lasers, while the internal quantum efficiency decreased by only ~3%.

### **9.1.5 Applications of the novel multi-bandgap quantum well intermixing technique**

Four oxide stripe lasers with different bandgap energies have been integrated on one InGaAs/AlInGaAs chip. With a maximum blue shift of lasing wavelength of 100 nm, there is about a 25% increase of threshold current.

Two ridge waveguide lasers with different bandgap energy have also been integrated on same InGaAs/AlInGaAs wafer. The lasing wavelengths are 1546 and 1503 nm. The threshold current of the 43 nm wavelength shifted laser increased by only 6 mA, compared to that of the as-grown laser (46 mA), while slope efficiency were very similar (12.1 and 12.8%), especially for 300  $\mu\text{m}$  long devices.

A 2x2 crosspoint optical integrated switch, incorporating semiconductor optical amplifiers (SOA), passive waveguide splitters and electro-absorption (EA) modulators, was fabricated employing this novel technique to define the three-bandgap energy structures. A modulation depth of 25 dB has been obtained for the operation wavelength of 1.55  $\mu\text{m}$ , on the application of an applied reverse DC voltage bias of 5 V, which indicates the sputtering process did not produce any

dramatic degradation in the performance of the MQW structure as an EA modulator.

### **9.1.6 Investigation of monolithically integrated Mach-Zehnder asymmetric interferometer demultiplexer**

The principle of a terahertz optical asymmetric demultiplexer has been investigated and the design of a MZI type demultiplexer has been carried out. Three kinds of MZI demultiplexers with different geometric structures have been fabricated using the SID technique. A series of assessments were carried out, which included the operation of the semiconductor amplifier, the propagation loss of the device, etc.

## **9.2 Future work**

Although the improved SID technique has been successfully demonstrated, there are several issues to be focused on. The introduction of Cu is still not accurately controlled, in terms of concentration, especially from the viewpoint of industrial application. Although PECVD SiO<sub>2</sub> can realize a concentration of Cu less than 10<sup>17</sup> cm<sup>-3</sup> within the waveguide/core region, it cannot prevent a high concentration of Cu in the cladding area, due to a high concentration of Cu in the sputtered SiO<sub>2</sub> layer (~10<sup>21</sup> cm<sup>-3</sup>). This could cause a serious problem in long-term laser/active device performance, considering the high diffusion rate of Cu.

Several improved processes are currently under investigation in Intense Photonics Ltd. The key point is to find a suitable way to reduce the concentration of Cu in sputtered SiO<sub>2</sub>, lower than 10<sup>18</sup> cm<sup>-3</sup> so that it can be significantly reduced across the whole epitaxy layers to meet the requirement of a large bandgap shift, low propagation loss and long term stability.

On the application side, future work should be focused on the investigation of various multi-bandgap integrated devices. One of the promising devices is a multi-wavelength integrated light source, which is desired by WDM transmission systems. This device is expected to include several active regions with different bandgap energy structures, which are connected by a 1×N MMI couplers so that all the emissions with different wavelengths are emitted from the same waveguide. Moreover, EA modulators could be integrated with the light emission sections to form a practical WDM transmitter system.

Investigation of MZI demultiplexers should be further addressed. The improved SID technique could be applied to form the passive region, instead of the standard SID process, to achieve low propagation losses. Then research should be focused on the performance of the device, such as a high-speed demultiplexing in OTDM system.

